Modelling the Subglacial Hydrology of Trinity-Wykeham Glaciers of the Northern Canadian Arctic

by

Michael Willette

A thesis
presented to the University of Waterloo
in fulfillment of the
thesis requirement for the degree of
Master of Mathematics
in
Applied Mathematics

Waterloo, Ontario, Canada, 2023

Author's Declaration

I hereby declare that I am the sole author of this thesis. This is a true copy of the thesis, including any required final revisions, as accepted by my examiners.

I understand that my thesis may be made electronically available to the public.

Abstract

In Canada's High Arctic region, the melting of glacial ice contributes substantially to the world's increasing sea levels (Harig and Simons, 2016). Of the icebergs in the region, approximately 62% are discharged by Trinity-Wykeham Glaciers. In the last twenty years, these glaciers have retreated approximately 5 km, also doubling in speed and tripling in iceberg production during that period (Van Wychen et al., 2016). It is argued that warming air temperatures are the primary cause of glacial retreat and consequently sea level rise in the Canadian High Arctic region (Cook et al., 2019). This is because the warmer air causes ice on the surface of glaciers to melt at a higher rate. This meltwater is routed to the base of the ice, where it can directly impact the glacier's velocity. If the water spreads into high-pressure cavities over a large enough area, the ice can often accelerate. However, if the water input is great enough to form large, low-pressure channels at the base of the glacier, water will be drawn from the higher-pressure regions and the ice will often decelerate (Iken and Bindschadler, 1986).

The Glacier Drainage System (GlaDS) subglacial hydrology model (Werder et al., 2013) is used to examine the development of hydrological networks at the base of Trinity-Wykeham Glaciers in response to variable surface melt rates between 2016 and 2019. GlaDS couples distributed and channelized subglacial drainage, allowing the mathematical model to capture the spatiotemporal evolution of the subglacial drainage system. The interplay between these two modes of drainage is highly influential on glacier dynamics. Satellite-derived datasets are used as inputs to the model, including basal and surface topography, surface velocities, and daily ice surface runoff products. Model outputs including subglacial water sheet thickness, water pressure, and channel discharge are compared to satellite-derived glacier surface velocities to determine how subglacial hydrology affects Trinity-Wykeham Glaciers. Nine model runs are completed to gauge the sensitivity of the GlaDS model to variations in two poorly constrained parameters that control the ease of subglacial water flow and determine a practical range of values for these parameters in future studies.

The results of this project suggest that Trinity-Wykeham Glaciers' velocities are directly influenced by surface melting rates and the configuration of the subglacial hydrology networks. Model outputs indicate that high subglacial water pressures cause acceleration at Trinity-Wykeham Glaciers and that with a sufficiently high influx of water to the bed, an efficient channelized drainage network develops that reduces local water pressures and causes a drop in flow velocity. The year 2018 is identified as a year in which channelized drainage is minimal, resulting in comparatively high water pressures and velocities after the melt season.

Acknowledgements

First and foremost, I consider it very important to recognize that this thesis was completed on the traditional land of the Haudenosaunee, Anishinaabe, and Neutral Peoples of Ontario as well as the Mi'kmaq Peoples of Newfoundland. I must also acknowledge the Indigenous Peoples of northern Canada, including the Inuit of Nunavut, my area of study, and the Southern Tutchone Peoples of the Yukon, whose culture I learned much about while in the province for fieldwork. I acknowledge and value their traditional knowledge and beliefs.

I would like to thank the University of Waterloo, the Natural Sciences and Engineering Research Council, the Ontario Graduate Scholarship program, the Northern Scientific Training Program, the ArcticNet Training Fund, the Qalipu First Nation of Newfoundland, and Indspire for financially supporting my education.

Thank you to all of my peers in the UWaterloo Glaciology group for the good times, for all the help along the way, and for making me feel welcome. In particular, I'd like to thank Kevin Siu and Koi McArthur for always lending a hand. To that end, I must also thank Adam Hepburn for reliably digging me out of many a hole when it came to modelling troubles, and for being a proper mate during his time in Waterloo.

Thank you Marek Stastna for acting as my supervisor at a crucial time in my program, and always giving sound advice. Thank you as well to Wesley Van Wychen, Luke Copland, and Dorota Medrzycka for teaching me much of what I know about glaciology.

Thank you so much to Christine Dow for the knowledge and support you've given me during my time as your student. You put your faith in me and always pushed me to strive for better. It has been rewarding and inspiring to learn under the guidance of one of the most brilliant minds in glaciology, and I count myself very lucky to have done so.

To Dylan and Mallory, thank you for truly being the best roommates and friends anyone could ask for. I can't wait to celebrate with you the second I step foot in Newfoundland again. Thank you Aaron, Nate, Brady, Ben, and all my other pals. You guys are the best.

Thank you to my mother, father, and sister for your neverending support. In every sense, I could have never made it through this master's program without you in my corner. Thank you for believing in me and encouraging me when I needed it most, I'm so deeply grateful to have a family like you.

Finally, I extend my heartfelt thanks to my beloved partner, Jenna. You have been my guiding light through all of this. Thank you for being a constant source of inspiration, comfort, happiness, and understanding.

Table of Contents

List of Figures

List of Tables

Chapter 1

Introduction

Glaciology, the study of glaciers and ice sheets, plays a vital role in our understanding of the Earth's climate. Approximately 68.7% of Earth's freshwater supply is frozen in the form of these large ice masses (Shiklomanov, 1993), and as the cryosphere continues to experience unprecedented changes, the response of glaciers to climatic variability poses major implications for global sea-level rise and the management of water resources. Predicting the nature of these responses is crucial if humanity hopes to adapt to the changing climate. Subglacial hydrology, the study of water flow beneath glaciers and ice sheets, is an important aspect of glaciology that has garnered increasing attention since the turn of the 21st century. Subglacial hydrology is known to control much of the ice dynamics and water discharge at many glaciers, making it an important area of study when trying to determine how glaciers will behave in the face of a rapidly changing global climate (Benn and Evans, 2010; Fountain and Walder, 1998; Iken and Bindschadler, 1986). The response of a glacier to water input to the bed—e.g., basal water pressure, the efficiency of subglacial drainage, and the morphology of the subglacial hydrological system—has a strong influence on the velocity of a glacier. Considering the global rise of air temperatures, which is manifested as melting on the surface of glaciers, the urgency of understanding the relationship between subglacial hydrology and glacier dynamics is clear.

Glaciers are generally difficult to study directly due to the remote locations and harsh environmental conditions in which they often reside. With the added barrier of hundreds to thousands of metres of ice, the subglacial environment is a particularly inaccessible area to investigate. In recent decades, many advancements in glaciological research have been driven by mathematical models. Models offer a controlled environment to simulate various scenarios and assess the sensitivity of glacial responses to changing environmental conditions. Through the integration of field observations, remote sensing data, and physical

principles, mathematical models enable scientists to analyze subglacial processes that are otherwise difficult to observe, such as basal sliding and meltwater routing. There are many mathematical models that seek to shed light on the hydrology of glaciers through the use of parameters that quantify glacial phenomena that are otherwise too complicated to capture (Flowers, 2015). Verifying the accuracy of these parameters, and of the models themselves, is key for assuring that the models can be improved and used as a tool to capture glaciological processes as accurately as possible.

Section 1.1 gives a review of glacier hydrology and its impact on glacier dynamics. Section 1.2 discusses the general properties of subglacial hydrology models and gives a number of examples of the capabilities of such models. Section 1.3 provides a broad overview of the Canadian Arctic Archipelago and Trinity-Wykeham Glaciers, the subjects of this project. Finally, Section 1.4 provides an overview of the structure of this thesis.

1.1 Glacier Hydrology

Conventionally, discussions of glacier hydrology separate the hydrological system spatially into three distinct sections—the supraglacial, englacial, and subglacial hydrological systems. These systems are closely linked, and events in one area of a glacier's hydrological system can have profound effects on the others, both directly and indirectly. Shreve (1972) provided the theoretical groundwork for hydrology in temperate glaciers and lists three main principles of the flow of water through these glaciers:

1. the capacity of the glacial hydrology system varies in response to the addition of meltwater;
2. water flow is directed primarily by overburden pressure exerted by the ice, as influenced primarily by surface slope and secondarily by bed topography;
3. the geometry of the system gradually evolves into an arborescent configuration over time in each subdomain (Shreve, 1972).

Subsection 1.1.1 provides a brief description of the supraglacial and englacial systems that conduct water on the surface of and within the ice respectively. Subsection 1.1.2 takes a more in-depth look at the movement of water at the base of the glacier within the subglacial hydrological network, the focus of this project.

1.1.1 Supraglacial and Englacial Hydrology

The supraglacial hydrological system dictates the flow and storage of water on the surface of a glacier. Most water found in this system is the product of surface melt due to above-zero air temperatures, and as such the supraglacial hydrological system is mostly restricted to the glacier's ablation zone during the melt season, i.e., the time of year in which most surface melting occurs (Pitcher and Smith, 2019). Rainwater also contributes to surface hydrology (Benn and Evans, 2010). The volume of water in the supraglacial system varies depending on factors including surface energy balance, season, and climate; some areas of the world, such as Antarctica, are too cold for melting to occur on the surface and receive very little rainfall, and therefore have minimal supraglacial hydrology (Banwell et al., 2023).

One way by which water is stored and transported in the supraglacial system is through snow and firn, or coarse, compacted snow with a density of 400-830 kg/m^3 that has yet to be compressed into ice (Paterson, 1994). Water flows through these porous media relatively slowly, and often freezes within the pack, forming superimposed ice (Benn and Evans, 2010). Firn aquifers are 4–25 metre-thick layers of firn that insulate water from sub-zero air temperatures and allow the water to remain liquid at great depths throughout the year (Chu et al., 2018). These aquifers can delay glacier runoff for periods lasting up to years (Forster et al., 2013; Munneke et al., 2014).

Water also flows on the glacial surface over bare ice in distributed systems that, with time, can incise into the surface to create deep river networks (Benn and Evans, 2010; Gulley et al., 2009a). At the beginning of the melt season, these rivers begin to form at lower altitudes and gradually extend upglacier as air temperatures increase. Rivers transport water much faster than flow through snow and firn, akin to a terrestrial river. However, rates of flow in glacial rivers vary more quickly than in their land-based counterparts—on as short as an hourly time scale—due to fluctuations in the surface melting rate (Pitcher and Smith, 2019; Smith et al., 2017). Supraglacial lakes can form in depressions on the glacial surface, often with a corresponding depression in the underlying bedrock, reforming in the same location over multiple years (Banwell et al., 2014; Echelmeyer et al., 1991). These lakes can be many square kilometres in area and up to several metres deep. Some lakes have crevasses at their bed which drain their contents into the englacial or subglacial hydrological systems (van der Veen, 2007). These drainage events can transpire in as little as a few hours, and occur due to a process called hydrofracture; when water seeps into crevasses created by the stretching of ice due to glacier flow, the outward pressure exerted by the water on the crevasse walls causes the opening to expand (Weertman, 1973). Crevasses like this allow surface water direct access to deeper parts of the glacier

and even the bed. Moulins are surface features that link the three hydrological systems, also formed by hydrofracture (Benn and Evans, 2010). Preferential and continual flow through a crevasse from a supraglacial lake or river can create a near-cylindrical conduit for water to reach the glacial base. These moulins are particularly important for water transport to the bed.

The englacial hydrological system serves the purpose of transporting water between the surface and base of a glacier, but comparatively little is known about the processes involved. In general, it is assumed that the glacial ice is impermeable to water flow. The presence of englacial channels and moulins is all that allows water to pass through the internal system of the glacier. Shreve's theoretical model of the englacial drainage system predicted that it takes the form of branching channels that travel deeper as the system extends downglacier (Shreve, 1972). These channels are fed from above by smaller, dendritic tributaries. In-situ observations suggest that englacial channels may form by means of hydrofracture, carving by surface streams and rivers, and the exploitation of weaknesses in the formation of the ice (Benn and Evans, 2010; Gulley et al., 2009b).

1.1.2 Subglacial Hydrology

Subglacial hydrology refers to the flow of water at the base of a glacier. While some glaciers are cold-based—that is, frozen to their beds—temperate glaciers have beds that are at the melting point, which is a condition conducive to water flow and production beneath the ice (Benn and Evans, 2010). The melting point of ice is dependent not only on temperature but also pressure; under high pressure from the overlying glacial ice, the freezing point of water is reduced, and thus water may persist at the bed at sub-zero temperatures (Robin, 1976). Geothermal heat from the earth and frictional heat generated by ice-bedrock contact both act to produce meltwater, and the thick ice above acts as an effective insulator from surface air temperatures (Benn and Evans, 2010). For many mountain glaciers and the Greenland Ice Sheet, the primary source of water at the bed is water routed from the supraglacial and englacial hydrological systems.

There are two classifications of subglacial drainage networks: distributed/inefficient networks and channelised/efficient networks. These systems are closely related and the interplay between the two drainage types can strongly influence glacier dynamics (Fountain and Walder, 1998). Distributed systems typically cover a large area of the glacier bed and can incorporate multiple modes of drainage (Benn and Evans, 2010). One such mode is a thin film of water that forms at the ice-bed interface at particularly inefficient parts of the bed (Weertman and Birchfield, 1983). These films consist only of meltwater produced

at the base and are very inefficient in water transportation. Many glaciers lie upon soft beds composed of sediment which allows both Darcian flow through the porous bed and the formation of braided canals in the sediment (Benn and Evans, 2010).

A common form of inefficient drainage in the subglacial hydrological system is a linked network of cavities. Cavities open when basal sliding over rocks creates separation between the glacier and the bedrock, creating a gap for water to pool into. Cavities are often found on the lee side of bumps in the bedrock. It follows that fast-flowing glaciers and glaciers with particularly rough beds are more likely to have numerous cavities that hold a great volume of water (Benn and Evans, 2010). However, these cavities are typically connected by narrow, highly pressurised orifices with very low flux and as such, water transportation is slow through a system of linked cavities (Fountain and Walder, 1998). As more water is added to the linked cavity system, water pressure p_w is increased. Were the glacier to cease motion, a process known as ice creep, in which glacier ice slowly deforms in response to stress applied by the overlying ice, would cause ice to fill the cavities and leave no room for water (Weertman, 1983). Ice creep still occurs in moving ice, but as the ice begins to fill the gap, it has already travelled downhill away from the opening. Therefore, cavities can persist beneath a glacier due to the glacier's motion. Water pressure in subglacial cavities also serves to counteract ice creep.

Efficient drainage at the glacial bed occurs through channels. There are multiple types of channels suggested to exist at the glacial bed, but the most common type of channel used for modelling subglacial hydrology is the Röthlisberger channel or R-channel (Röthlisberger, 1972). As water is added to a distributed system of linked cavities, the increase in pressure, in accordance with Bernoulli's principle, forces the water to flow at a faster rate. This causes friction which produces heat that melts the surrounding ice, increasing the size of the small orifices in the inefficient system as the sole of the ice is melted away. The growth of these orifices results in a decrease in the water pressure within, in turn creating a hydraulic potential gradient that allows water to be drawn from the distributed system into the now semicircular R-channels. R-channels persist when the rate of melt on the channel walls exceeds the rate of closure due to the overburden pressure exerted by the glacier ice above, $p_i = \rho_i g H$ (Röthlisberger, 1972). Other types of channels have been proposed, such as Nye-channels which are incised into subglacial bedrock (Nye, 1973). Evidence for the existence of Nye channels has been found in numerous deglaciated areas, with depths up to ~ 0.1 m (Fountain and Walder, 1998). Hooke et al. (1990) and Walder and Hallet (1979) suggested that channels melted into the glacier sole are more likely to take on a broader and lower cross-section than those proposed by Röthlisberger due to decreased melt at the ceiling of the channel when discharge is low. R-channels and Hooke channels have been observed at the termini of valley glaciers.

For a majority of glaciers, the transition between distributed and channelised drainage is brought about by changes in meltwater input (Benn and Evans, 2010; Copland et al., 2003). Although meltwater input can undergo large diurnal variations due to fluctuating air temperatures (Smith et al., 2021), changes in the morphology of the subglacial hydrology system happen over daily or weekly timescales; dye-tracing experiments through the moulins of John Evans Glacier on Ellesmere Island in the Canadian Arctic Archipelago by Bingham et al. (2005) suggested that the subglacial system underwent a transition from entirely distributed to channelised over the course of 13 days, based on a relationship between the supraglacial discharge into a given moulin and the mean water-flow velocity. Bingham et al. (2006) later inferred that a week-long period of cool air temperatures during the melt season at John Evans Glacier may be sufficient to revert a channelised network to a distributed cavity system. In the colder months of the year when there is minimal surface melt, ice creep typically closes any channels present from the prior melt season and pressurises water remaining at the bed (Rada Giacaman and Schoof, 2023; Hart et al., 2022). In this state, virtually all water at the bed is produced by basal melting processes, and the distributed system transports this small volume of water inefficiently. As air temperatures rise in the spring, surface melt commences. Melting rates trend upward at the beginning of the melt season and decrease with elevation (Noël et al., 2018; Wójcik and Sobota, 2020). The influx of meltwater to the bed causes abrupt and significant pressurisation in the distributed system due to its inefficiency. This phenomenon is referred to as the spring event (Bartholomew et al., 2010; van de Wal et al., 2015). Faster water flow leads to enhanced frictional melting which enlarges subglacial cavities, thereby increasing their capacity. With a sufficient melt rate greater than the rate of creep, channels will develop between cavities due to the instability of the linked cavity system (Benn and Evans, 2010). With time, a branching network of channels forms, typically beginning near the terminus and extending upglacier. Once the melt season ends, the meltwater input gradually decreases until ice creep overtakes the melt rate, and the distributed network is once again the primary mode of drainage.

An important distinction between linked cavities and channel networks is the relationship between water volume and water pressure. As mentioned previously, the orifices linking subglacial cavities are quite narrow and thus an increased influx of water increases the water pressure. In contrast, channels persist at much lower water pressure because frictional heat due to additional water causes the channels to grow larger, and ice creep does not act fast enough to counteract this (Fountain and Walder, 1998). Water is naturally poached from the high-pressure distributed system into low-pressure channels following a hydraulic potential gradient, $\nabla\phi$, where $\phi = \phi_m + p_w$ is hydraulic potential, $\phi_m = \rho_w g b$ is the elevation potential, ρ_w is the density of water, g is acceleration due to gravity, b is bed

elevation, and p_w is water pressure. This implies that areas of the glacial bed with greater water volume are dominated by dendritic networks of channelised drainage with very little distributed flow.

1.1.3 Glacier Dynamics

Findings from direct observations, theoretical analyses, and mathematical modelling strongly suggest a correlation between short-term variations in glacier sliding velocity and subglacial water pressure in tidewater (or marine-terminating) glaciers across the Arctic (e.g., Copland et al. (2003); Dalton et al. (2022); Davison et al. (2020); Müller and Iken (1973)). Seasonal and interannual velocity patterns in Greenland, Svalbard, and the Canadian Arctic Archipelago (CAA) indicate that short-term subglacial hydrology changes, typically due to variations in meltwater production, can cause significant changes in seasonal flow patterns (Anderson, 2004).

A seminal study by Almut Iken sought to interpret hourly-to-daily velocity variations that had been observed at many glaciers and their relation to subglacial hydrology using an idealised numerical model (Iken, 1981). Using two-dimensional finite-element analysis on an infinitely wide ice mass sitting on an idealised sinusoidal bed, Iken argued that fluctuations in water pressure p_w act to induce basal sliding in two distinct phases. There are transient phases, which include the instantaneous re-distribution of overburden pressure by subglacial water resulting in the separation of the glacier from its bed, and the growth and shrinking of subglacial cavities. Steady-state sliding is the second phase, in which the glacier slides over stable cavities at a given water pressure (Iken, 1981). Iken went on to conclude that sliding velocity is a function of both p_w and subglacial cavity size. These findings were put to the test in an experiment by Iken and Bindschadler (1986) at Findelengletscher, Switzerland in which borehole measurements of water levels in the subglacial drainage system (taken as an indicator of subglacial water pressure) were compared to surface velocity variations. They concluded that flow velocities were sensitive to variations in pressure in a subglacial cavity system that increased separation from the bed in response to elevated water input, exhibiting a functional relationship between the two variables. Sliding velocity begins to increase in response to p_w only when p_w exceeds a threshold referred to as the "separation pressure", but this acceleration becomes unstable and rapid as p_w increases further and approaches p_i. Similar measurements of diurnal water pressure and velocity variations by Kamb et al. (1994) at Columbia Glacier, USA, further support the existence of this functional relationship.

Observations at Helheim Glacier, East Greenland show that both diurnal and multi-day variations in velocity occur in response to variations in surface melt and the resultant

reduction in basal friction, with peak diurnal velocities coinciding with peak meltwater flux to the bed from the englacial system (Andersen et al., 2010, 2011; Stevens et al., 2022). Similar velocity patterns have been observed at Petermann Glacier in northern Greenland, where summer velocities accelerate by $\sim 15\%$ seasonally, and a subglacial hydrology model one-way coupled to an ice sheet model reproduced the observed magnitude, timing, and duration of velocity variations (Ehrenfeucht et al., 2023), pointing to subglacial hydrological factors as the primary control on the seasonal velocity variations. Joughin et al. (2008) also reported summertime accelerations of 15% or less in summer in western Greenland outlet glaciers. It should be noted that in Greenland, subglacial hydrology is often a larger influence on velocity further into the ice sheet, whereas ocean warming and retreat are often cited as the dominant control on the coastline (Carr et al., 2013a; Joughin et al., 2008; Seale et al., 2011; Straneo and Heimbach, 2013).

Moon et al. (2014) presented a record of seasonal velocities for 55 tidewater glaciers on the eastern and southwestern coasts of Greenland between 2009 and 2013. While some slow-moving glaciers exhibited small intra-annual velocity ranges, the majority exhibited mean ranges of 150–500 m/yr and were separated into three distinct types based on the patterns in their velocities changes. Type 1 glacier behaviour was attributed to ice-front position, but Type 2 and 3 glaciers both showed patterns heavily influenced by subglacial hydrology. Type 1 glaciers exhibited a speedup between late spring and early summer, with velocities remaining elevated late into the winter or early into the spring. Type 2 glaciers were characterised by significant speedup in the early summer as melt rates grew, and stable velocities through the remainder of the year, aside from brief periods of acceleration in response to meltwater anomalies. Type 3 glaciers were generally found further south than Type 2 glaciers in areas of greater surface melt, exhibiting deceleration in response to high rates of melt, a prominent late-summer slowdown, and especially high intra-annual velocity ranges. The seasonal velocities in Type 2 and 3 glaciers in the study reflect two scenarios in which surface melt and subglacial hydrology directly influence glacier dynamics; Type 2 glaciers indicate distributed drainage throughout the year, whereas Type 3 glaciers indicate a transition from distributed to channelised drainage in response to higher rates of surface melt. Svalbard is a Norwegian archipelago located northeast of Greenland in the Arctic Ocean. Summertime velocities at Kronebreen, Svalbard showed the behaviour of a Type 3 glacier in 2013 and a Type 2 glacier in 2014, showing that these seasonal patterns can also vary year-to-year based on surface meltwater production (Vallot et al., 2017).

Velocity variations in response to meltwater input are not limited to the Nordic regions. The CAA is an area of particular interest because it is home to Trinty-Wykeham Glaciers, the subjects of this project. A detailed overview of the CAA is given in Subsection 1.3.1. Van Wychen et al. (2020b) pointed to the velocity regime of Belcher Glacier on Devon Ice

Cap as typical for large outlet glaciers in the northern CAA. Ice creep deformation drives flow in the higher elevation regions of the glacier (40–60 km from the terminus) where ice flows at just 5–15 m/yr. Between 40 and 15 km from the terminus, ice is channelled through valley margins where it thickens and picks up speed. Thicker ice reduces the pressure melting point beneath the glacier, resulting in increased water at the bed, reduced basal friction, and sliding with typical velocities between 25 and 100 m/yr (Van Wychen et al., 2020b). Velocities continue to increase up to $\sim$ 500 m/yr as elevation decreases and sliding becomes a more dominant force (Van Wychen et al., 2020b).

Analyses of subglacial hydrology and ice dynamics have been extensive at John Evans Glacier, located on Ellesmere Island in the northern CAA (the same island as the study site in this project). The nature of the subglacial hydrology at John Evans Glacier is highly sensitive to rates of surface melt. Dye-tracing experiments in the summers of 2000 and 2001 illustrated the system's sensitivity to meltwater input to the bed (Bingham et al., 2005). Tracer breakthrough curves were indicative of distributed drainage at the beginning of the melt season during both years. The summer of 2000 was notably warmer in the region and Bingham et al. (2005) reported the rapid formation of a channelised subglacial network in response to high water influx to the bed, and that this network persisted until the end of the melt season. In a later article, Bingham et al. (2006) suggested that these channels alleviate widespread high basal water pressures that would otherwise arise. In direct contrast is the cooler summer of 2001, in which inefficient distributed drainage persisted through the melt season. Bingham et al. (2006) also determined from this study that a week-long period of decreased air temperatures can lead to the complete closure of a network of channels. These results led to the conclusion that the high rates of supraglacial water input to the bed are often instrumental in the formation, structure, and persistence of channelised subglacial drainage in High Arctic glaciers. Copland et al. (2003) noted a strong relationship in both time and space between glacier flow rates, surface elevation changes, surface water input, and the evolution of subglacial drainage at John Evans Glacier, which in turn control basal water pressure and storage.

Alaska, USA is another North American point of interest for the study of subglacial hydrology and glacier dynamics. Meier et al. (1994) observed three types of velocity variations at Columbia Glacier, Alaska: diurnal fluctuations (5–8%) in coincidence with borehole water levels, speed-up events lasting $\sim$ 3 days during times of high water input, and "extra-slowdown" events lasting $\sim$ 3 days that follow a speed-up event and result in velocities below those prior to the initial speed-up. The extra-slowdown events, in particular, were taken as an indication of the expansion of subglacial channels from increased water flux, and subsequent efficient drainage (Kamb et al., 1994; Meier et al., 1994; Müller and Iken, 1973). GPS measurements of vertical and horizontal displacement at Bench Glacier,

Alaska led Anderson (2004) to suggest that effective pressure (that is, overburden pressure minus subglacial water pressure) is inversely proportional to sliding velocity. They also suggested that a sudden drop in surface elevation observed at the glacier must coincide with a drop in water pressure brought about by a channelised drainage network, marked by increased discharge from the terminus.

The relationship between basal water pressure and the evolution of the subglacial hydrological network is complex in nature. Iken (1981) showed that elevated basal water pressures result in the separation of a glacier from its bed and, in turn, reduced friction and basal sliding at elevated velocities. High rates of sliding increase the opening rate of cavities, and the elevated water pressure counteracts the closure of these cavities by creep (Schoof, 2005; Walder, 1986). In contrast, channel formation and size are not products of basal sliding but of increased discharge, which results in greater melt on the channel walls. This elevated melt widens the channels, counteracting ice creep, which in turn means that the growth of subglacial channels coincides with lower water pressures, leading to a pressure gradient that draws water from smaller tributaries into larger channels (Röthlisberger, 1972; Schoof, 2010). The efficient drainage of meltwater through these channels reduces water pressure at the bed, causing a drop in sliding velocity and cavity formation. Only decreased discharge and the resultant decrease in frictional melting can close these channels and revert the system to a primarily distributed configuration. This is evident in the seasonality of basal water pressures and changes in velocity observed at the many glaciers discussed in this subsection, with high velocities in the early melt season, a sharp deceleration in the later melt season, and relatively stable winter flow rates. Meltwater input and the resulting basal water pressures directly influence the state of the subglacial drainage network and the efficiency of the drainage therein, which in turn influences glacier velocities. As such, incorporating not just both modes of drainage, but the transition between the two as an adaptation to meltwater input, is essential to any model that seeks to capture the realities of subglacial hydrology.

1.2 Subglacial Hydrology Modelling

1.2.1 Basics, Variations, and Limitations of Subglacial Hydrology Models

The foundations of mathematical glacier drainage models were first developed in the latter half of the twentieth century (Fountain and Walder, 1998; Iken, 1981; Iken and Bindschadler, 1986; Shreve, 1972). Over time, as the motivating factors behind subglacial hy-

drology modelling have shifted, so too have the approaches to modelling (Flowers, 2015). The earliest subglacial hydrology models were developed for two purposes: to characterise glaciers' contribution to the earth's greater hydrological cycle in the form of runoff (e.g., Fountain and Tangborn (1985); Gottlieb (1980)), and to better understand the effects of subglacial hydrology on glacier dynamics (e.g., Iken and Bindschadler (1986)). Later models were designed with a greater focus on the accuracy of the morphological and functional representations of the subglacial hydrological system (e.g., Arnold and Sharp (1992); Flowers and Clarke (2002); Johnson and Fastook (2002)). This shift introduced a number of limiting factors, such as the requirement for system geometry to be prescribed beforehand instead of developed within the simulation. Nonetheless, this was a necessary step forward in the pursuit of hydrology coupled with glacier dynamics. Most recently, these limitations have been remedied using a two-dimensional numerical framework incorporating both distributed and channelised drainage and, most critically, the interaction and transient evolution between the two (e.g., Hewitt (2011); Schoof (2010); Werder et al. (2013)). Distributed drainage takes the form of a continuum, whereas channelised drainage takes place within a discrete network. The two-dimensional implementation of these models streamlines coupling with glacier dynamics models. There also exist "soft bed" hydrology models, typically concentrated in Antarctic ice streams, that focus on the hydrological permeability of subglacial sediment (e.g., Alley (1989)).

Flowers (2015) provided a wide-sweeping review of subglacial hydrology models, with an emphasis on spatially distributed models used primarily for characterising ice dynamics. A "recipe" for a subglacial drainage model is presented. This recipe delineates the essential mathematical principles ubiquitous in the field of subglacial hydrology modelling. The first such equation is the conservation of (water) mass, governed by

$$\frac{\partial h}{\partial t} + \nabla \cdot \mathbf{q} = m_b. \tag{1.1}$$

Here, h is the depth or volume of (incompressible) water, $\mathbf{q}$ is the water flux per unit area in the distributed system, and m_b is the source or sink term that represents the total amount of water available from supraglacial runoff routed to the bed, water produced through englacial strain, storage in adjacent aquifers, and meltwater produced at the bed through geothermal and frictional heating. Water flux is often computed through the empirical expression

$$\mathbf{q} = -Kh^{\alpha} \left(\nabla \phi\right)^{\beta}, \tag{1.2}$$

where K is a rate factor, $\nabla\phi$ is the potential gradient of the water, and α and β are exponents used to dictate the nature of flow in the system. When $\alpha = \beta = 1$, flow is

laminar in accordance with Darcy's law, and when $\alpha = 5/4$ and $\beta = 1/2$, flow is turbulent. Hydraulic potential ϕ represents the total mechanical energy cost per unit volume to move water from one state to another, separated by pressure p_w and elevation b,

$$\phi = p_w + \rho_w g b, \tag{1.3}$$

where ρ_w is the density of water and g is the rate of acceleration due to gravity. Some models instead define hydraulic potential only in terms of glacier geometry, replacing the water pressure term with $\rho_i g H$, where ρ_i and H are the density and thickness of the overlying ice respectively. The transient evolution of the hydrological system requires an equation to govern the system's capacity at a given time:

$$\frac{\partial h'}{\partial t} = w - v, \tag{1.4}$$

where w is the rate of cavity opening and v is the rate of cavity closure. Here, h' is representative of the capacity of the subglacial system at a given time.

As with any area of modelling, subglacial hydrology models suffer from limitations that impact the reliability of their outputs. The subglacial environment is a complex system with countless variables at play affecting the movement of water—basal composition, the presence and size of till, temperature, pressure, and many more factors have a direct influence on subglacial discharge. Further complicating the modeller's task, the thick glacier ice serves as a barrier to direct observation of these key parameters. As such, assumptions and simplifications must be made. These assumptions and simplifications also help lower the computational cost and time required to run the model. A common way of simplifying models is to assume that certain parameters at the bed are homogenous, isotropic, or otherwise uniform. Such parameters include but are not limited to basal composition (most often assumed to be impermeable bedrock), basal friction, the conductivity of water through channels and cavities, and the height of bumps in the bed that facilitate cavity formation. Many models, especially those used on ice sheets as opposed to glaciers, assume that water pressure is equal to overburden pressure across the domain, typically to avoid the computational cost of applying more sophisticated hydrology models (e.g., Alley et al. (2003); Willis et al. (2016)). The treatment of channels is another area that is often simplified. In many cases, the description of R-channels from Röthlisberger (1972) are used as the basis for subglacail conduits within a model (e.g., Arnold et al.; Schoof (2010); Werder et al. (2013). One consequence of this is the assumption that R-channels are fully saturated with water at all times. Many models also restrict their system to either laminar or turbulent flow through channels, seldom both (e.g., Alley (1996); Hager et al. (2022); Werder

et al. (2013)). Our limited knowledge of subglacial conditions due to the inaccessibility of the glacial bed makes broad assumptions like these a necessary compromise.

1.2.2 Recent Developments in Arctic Subglacial Hydrology Modelling

Subglacial hydrology has had a resurgence in popularity with modellers in the twenty-first century as they try to expand our understanding of subglacial processes. Many of the modelling endeavours have been focused in the Nordic region, with little attention paid to Canadian Arctic glaciers. Pälli et al. (2003) constructed digital elevation models (DEMs) of Hansbreen and Werenskioldbreen, two polythermal glaciers in Svalbard, from ground penetrating rader-acquired bedrock data. Hansbreen is a marine-terminating glacier with many overdeepenings in its basal topography. These DEMs were used to create maps of subglacial hydraulic potential, as defined by Shreve (1972), and the flow paths of the subglacial hydrological networks. The gridded surface and bedrock elevation data were used to calculate subglacial hydraulic potential with three different values of flotation fraction K—that is, the ratio of water pressure to ice overburden pressure. Two methods, D_8 and D_∞, from the TauDEM program were used for determining flow direction, (O'Callaghan and Mark, 1984; Tarboton, 1997; Tarboton and Ames, 2001). The D_8 method assigns a discrete flow direction from one element to the next based on the steepest slope, whereas the D_∞ method expresses flow direction as an angle with a continuous value between 0 and 2π. Modelled flow paths were largely in agreement with observations, including ground-penetrating radar evidence of channels at Hansbreen and moulin locations determined from aerial photography. Moulin locations were typically found near predicted subglacial channel locations and distributed flow paths, as one could expect given that moulins serve to concentrate surface meltwater flow into a relatively small area of the bed. Comparisons to borehole pressure measurements led the authors to conclude that overdeepened areas are particularly susceptible to rapid fluctuations in water pressure resulting from changes in water input. In the overdeepened areas of Hansbreen, the ice is between $\sim$ 100–300 m thick. Overdeepenings were near overburden pressure in the winter because the subglacial drainage network is inefficient and cannot escape the large cavities in the area detected by ground penetrating radar, but approached atmospheric pressure in as short as four days during the summer months, indicating an established channel network. Modelled locations of outflow sites, however, did not match in-situ observations.

Subglacial drainage at Kongsfjord basin, Svalbard is the topic of a study by Scholzen et al. (2021). The two-dimensional Glacier Drainage System model (GlaDS, see Section 2.1)

was applied to three adjacent tidewater glacier systems fed by Kongsfjord basin—namely Isachsenfonna–Kongsbreen, Holtedahlfonna–Infantfonna–Kronebreen, and Kongsvegen. These tidewater glaciers bear similarities to Trinity-Wykeham Glaciers, the subjects of this study (see Subsection 1.3.2). For instance, the beds in the ablation zones of each glacier are characterised by large regions of overdeepened topography (Harcourt et al., 2019). Kronebreen and Wykeham Glacier both flow in two distinct branches near the grounding line, divided by a bedrock ridge. Kronebreen also exhibits some of the highest velocities observed in Svalbard glaciers, with mean annual velocities approaching 800 m/year and summertime maxima approaching 1200 m/yr, again mirroring Trinity-Wykeham Glaciers (Van Wychen et al., 2020b). Four different experiments were completed, each with a unique method of transporting surface meltwater to the bed. The control experiment used the basal melt rate as a proxy for the surface melt rate, with all surface melt simply generated at the bed instead. Experiments 2 and 3 incorporate gradual meltwater routing through moulins. The latter of these experiments excludes meltwater generated away from moulin catchments. Experiment 4 is considered the most realistic, as it adds immediate transport to the bed through crevasses in the lower reaches of the glaciers to the configuration of Experiment 3. The fourth method, despite delivering the greatest volume of meltwater to the bed, yielded the lowest water pressures year-round due to comparatively efficient drainage. Across all experiments, however, channels were found to be ineffective at reducing subglacial water pressures during the melt season, a fact attributed to low hydraulic gradients, low surface gradients causing insufficient basal melt, and the short melt seasons in the area. The inefficiency of these channels made the glaciers more susceptible to basal sliding in response to high meltwater input and, in turn, elevated summer velocities.

Southern Greenland is the focus of many glacier hydrology modelling studies due to its rapid melting in response to rising temperatures in the Atlantic Ocean. Subglacial hydrological processes are widely regarded as a driver of seasonal velocity changes in the region. Spatially distributed modelling was used by Clason et al. (2015) to simulate the delivery of water from the surface to the bed by moulins and supraglacial lake drainage events at Leverett Glacier, Southwest Greenland, building on previous work at Devon Ice Cap, Nunavut, Canada (Clason et al., 2012). Like the supraglacial and subglacial systems, the englacial hydrological system also evolves in time and space, an important process that is often overlooked in glacier modelling. The model predicted the amount of supraglacial water storage, where and when moulins emerged, the drainage of supraglacial lakes, and the volume of water transported to the bed on a given date through each surface feature. A degree-day model driven by meteorological data and ultrasonic depth gauge measurements was used to generate meltwater and snow accumulation and included considerations for the refreezing of water within snowpack and slower meltwater flow through snow-covered

areas. A single-flow direction algorithm based on surface elevation was used to route surface meltwater (Schwanghart and Kuhn, 2010; Schwanghart and Scherler, 2014). Existing supraglacial lakes observed in Landsat imagery were manually digitized in the model, with the possibility of both rapid drainage to the bed through hydrofracture and slow drainage downglacier as the lakes exceed their maximum volume. Crevasse locations were determined from tensile stresses calculated from RADARSAT annual mean ice surface velocities (Vaughan, 1993), and crevasses depths were driven by surface meltwater and stresses using a model of water-filled crevasse penetration (van der Veen, 2007). The modelled meltwater input to the bed aligns closely with observed temporal and spatial patterns of acceleration at Leverett Glacier. There was a strong association between predicted periods of rapid drainage to the bed and observed acceleration events across the domain. The model indicated that moulins were the primary method of meltwater delivery to the bed at low elevations. Elevated meltwater drainage was not associated with speedup near the terminus, indicative of the efficient channelisation that has been proposed to develop in the region. At the highest elevations where supraglacial lake drainage is of greater importance, the delay between high melting rates and surface-to-bed water flux within the model agreed with the timing of high air temperatures and subsequent velocity increases in the area, showing the successful simulation of the slow flow rates and refreezing of meltwater within snowpack as well as the accumulation of water in supraglacial lakes. Poinar et al. (2019) also investigated the effects of an englacial hydrological process on the subglacial system in their project simulating Helheim Glacier, Southeast Greenland. The GlaDS model was implemented with multiple meltwater input regimes to simulate the delay of meltwater transport to the bed caused by water storage in firn aquifers. Firn aquifers increased meltwater supply to the bed by 10%, with the most significant gain in regions further upglacier, increasing basal water pressures and slow-growing channelisation at high elevations but reducing water pressures at lower elevations due to increased channelisation. Steady meltwater from firn aquifers allowed subglacial channels to persist year-round, enabling the channel network to adapt more rapidly to high rates of meltwater influx. This served to reduce seasonal water pressure fluctuations, such as the initial melt season pressurisation, downstream of the aquifers. These effects matched observations at Helheim Glacier and other Southeast Greenland tidewater glaciers that have substantial firn aquifers (Miège et al., 2016).

In 2020, Cook et al. (2020) introduced a three-dimensional subglacial hydrology model that couples distributed and channelised drainage through the GlaDS model and a one-dimensional simulation of water plumes generated at the calving front, within the Elmer/Ice ice flow model (Gagliardini et al., 2013; Werder et al., 2013). This model was applied to Store Glacier on the west coast of Greenland. The primary conclusions drawn from the

study included the assertion that freshwater flux from the terminus does occur during the winter from perennial channels up to $\sim$ 5 km in length and consistent frictional and geothermal meltwater production that drives plume melting at the calving front. This opposes the frequent assumption that freshwater discharge is zero during the winter months (e.g., Carroll et al. (2015); Slater et al. (2018)). There was a weak connection between surface melt and plume melting rates, but a strong connection between surface melt and subglacial water pressures even in the presence of extensive channelisation. Plume melting was found to make up over half of all freshwater outflux in the winter but only 5% during the melt season. However, the average rate of plume melting did increase in the summer but only slightly; large channels drove high rates of plume activity locally, but wide areas of the terminus were relatively unaffected by the increased basal discharge. A later study by Cook et al. (2022) built on these findings, this time using a model incorporating ice flow, GlaDS subglacial hydrology, plume melting, and the new additions frontal calving and two-directional coupling between the dynamics and hydrology. This study reaffirmed many of the findings from the 2020 study and reproduced observed calving, velocity, and water pressure measurements. Terminus velocity was found to be the primary control on calving patterns because of its influence on terminus position, though calving rates were also found to be susceptible to variations in plume melting. A hydrodynamic feedback far upglacier was reported to cause the water volume in the distributed system to increase; overburden pressure is greater in these areas where the glacier is thicker, increasing rates of ice creep and thereby impeding channel formation. Hydrodynamic feedbacks were also cited as a major control on calving rates, which are susceptible to variations with changes in velocity. Cook et al. (2022) concluded that Store Glacier, and in turn other Arctic tidewater glaciers, can be heavily influenced by hydrology. Outputs simulating the high-melt year of 2012 indicated a thoroughly channelised bed at the terminus and a higher number of plumes, causing faster frontal melt, instability, and increased calving, whereas channelisation in 2017 was said to be limited as a result of lower surface melt rates. One important takeaway was that there was little difference in the state of the glacier at the end of both the 2012 and 2017 runs, indicating that the hydrology and dynamics of the prior melt season may not have a strong influence on the following months/years.

In a study aimed at explaining seasonal velocity variations observed at Petermann Glacier, northern Greenland, Ehrenfeucht et al. (2023) coupled the GlaDS subglacial hydrology model to the Ice-sheet and Sea-level System Model (ISSM) in one direction such that the hydrology influenced glacier dynamics but the dynamics had no bearing on subglacial drainage. GlaDS simulated the state of the subglacial hydrological system including the effective pressure at the bed. Effective pressure outputs were then fed to ISSM to infer the basal friction at a given place and time using inverse methods, from which the velocity

of the glacier is calculated. The coupled model was successful in reproducing seasonal velocities captured in satellite observations and indicated that efficient drainage does not develop at the bed of Petermann Glacier. Outputs showed low effective pressures and high amounts of water at the bed year-round in an area of substantial grounding line retreat and corroborated the theory that this area is constantly near flotation and therefore less stable. Channel locations at the grounding line also aligned with known ice shelf channels at Petermann Glacier.

1.3 Study Area

1.3.1 The Canadian Arctic Archipelago

The Canadian Arctic Archipelago (CAA) is a cluster of islands located directly north of mainland Canada, composed of 94 major and over 36,000 minor islands that span $\sim 1,400,000$ km^2 (Adams and Dunbar, 2006). These islands contain the largest area of glacierised terrain outside of the ice sheets of Antarctica and Greenland. Approximately 70% of this glacier mass is contained within the large ice fields and ice caps of the Queen Elizabeth Islands (QEI), the northernmost cluster of islands in the CAA (Van Wychen et al., 2020b). The QEI's many major ice masses include Devon Ice Cap on Devon Island, Steacie and Müller Ice Caps on Axel Heiberg Island, and the Prince of Wales, Manson, and northern Ellesmere Icefields and Sydkap and Agassiz Ice Caps located on Ellesmere Island. Baffin and Bylot Islands are further south of the QEI and contain the remainder of CAA's glacier mass in their respective fields and caps. Figure 1.1 from Van Wychen et al. (2020b) shows the locations of these and other ice masses across the eastern CAA. Other than these large ice caps, ice in the CAA also takes the form of much smaller ice caps along with valley and cirque glaciers found along coastlines. In all, the CAA holds enough ice mass to contribute 199 ± 30 mm to global mean sea level rise (Cook et al., 2019).

While the central and western islands of the CAA largely consist of flat, low-relief terrain, the Arctic Cordillera ecozone found in the eastern CAA—namely the QEI—is highly mountainous and harbours conditions conducive to glacier formation. As typical of polar regions, the CAA has relatively short, cool summers that lead into long, cold winters. Baffin Bay is located east of the CAA, acting as the primary moisture source for the region. Precipitation, primarily in the form of snowfall, follows a gradient from southeast to northwest, with most areas in the regions accumulating less than 200 mm/yr (Van Wychen et al., 2020b). The lapse rate dictates that atmospheric temperatures decrease with altitude, so as moist air from Baffin Bay ascends the mountains of the QEI, it changes phase

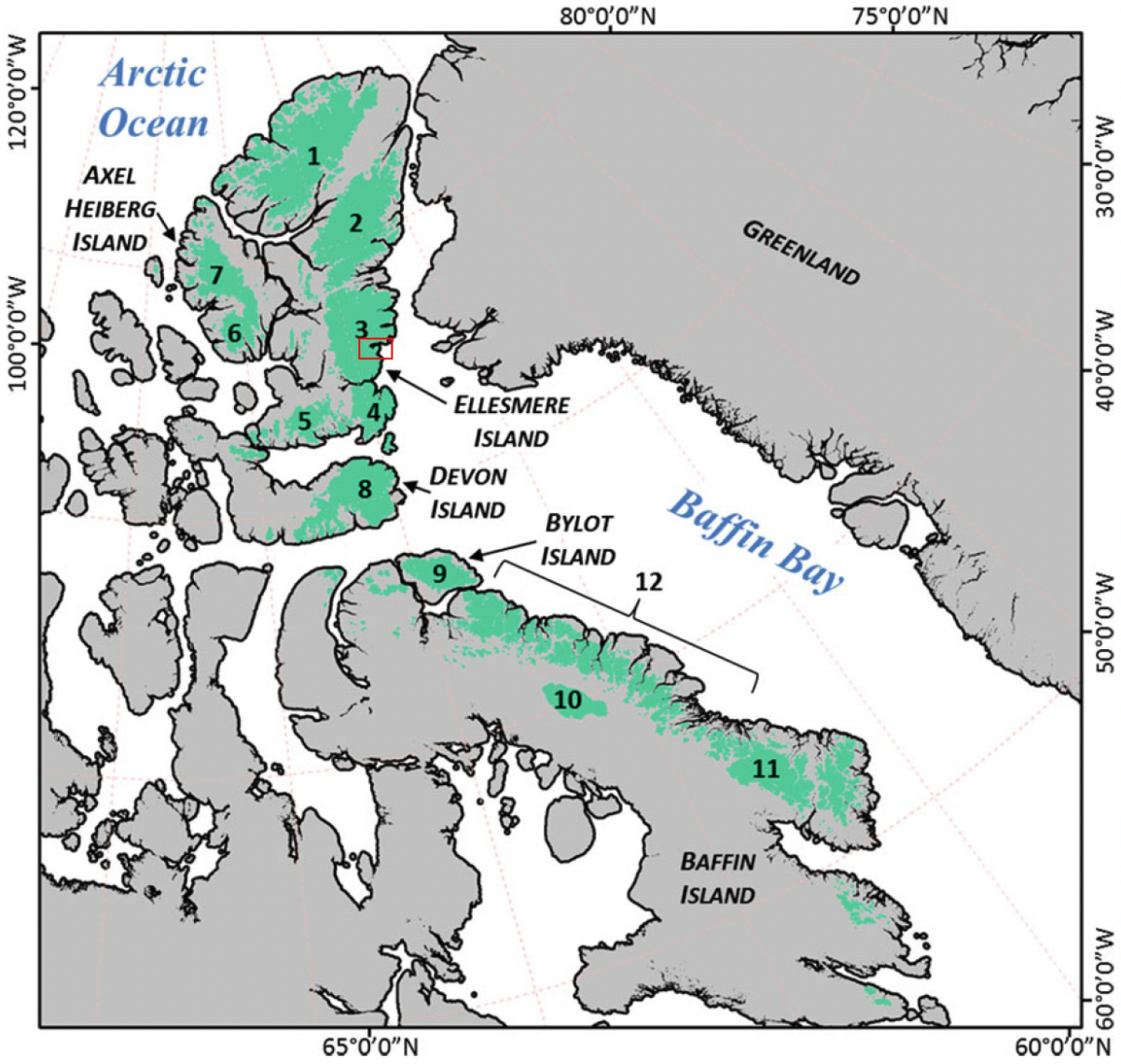

Figure 1.1: Overview of the major ice masses of the eastern Canadian High Arctic (denoted by green shading). 1 = Northern Ellesmere Icefield; 2 = Agassiz Ice Cap; 3 = Prince of Wales Icefield; 4 = Manson Icefield; 5 = Sydkap Ice Cap; 6 = Steacie Ice Cap, 7 = Muller Ice Cap; 8 = Devon Ice Cap; 9 = Bylot Island Ice Cap, 10 = Barnes Ice Cap; 11 = Penny Ice Cap; 12 = Coastal Glaciers and Ice Caps of Baffin Island. The red rectangle on Ellesmere Island denotes Talbot Inlet, the location of Trinity-Wykeham Glaciers. Adapted from Van Wychen et al. (2020b).

into snow and accumulates at the mountaintops. As such, the major ice caps of the region are found at the summits of these mountains 1800–2000 m above sea level and extend down to 400–500 m above sea level, with thicker sectors forming adjacent to the moisture-rich Baffin Bay (Van Wychen et al., 2020b). Marine-terminating outlet glaciers carry ice from these sectors down to the ocean.

The CAA is subject to a phenomenon that has been dubbed Arctic Amplification, in which high-latitude regions of Earth are warming two to three times as fast as the global mean due to strong ice-albedo positive feedback (Cohen et al., 2014; Mortimer and Sharp, 2018; Short and Gray, 2004). This rapid warming in the Arctic has manifested itself in the form of extensive glacier mass loss and retreat. From 2006 to 2016, the Canadian Arctic North experienced the second highest absolute mass loss of any region on Earth at 60 ± 84 Gt/yr (Zemp et al., 2019). Additionally, of the over 300 marine-terminating glaciers in the CAA, over 94% retreated between 1958 and 2015, with glacier retreat rates in the CAA increasing fivefold in the twenty-first century (Cook et al., 2019). Glacier retreat in polar regions—the neighbouring Greenland Ice Sheet, for instance, located just eastward adjacent to Baffin Bay—is generally accepted to be driven by warming ocean temperatures (Carr et al., 2013a; Seale et al., 2011; Straneo and Heimbach, 2013). Despite this, rising atmospheric temperatures are suggested to play a larger role in the retreat and mass loss observed in the CAA. In general, the length and intensity of the melt season in the QEI have risen substantially since 2005, as seen in Figure 1.2 (Sharp et al., 2011). Bedrock topography may also be an important factor in the extreme mass loss; many of the large northern CAA outlet glaciers are grounded below sea level for tens of kilometres up-glacier, making them more likely to accelerate, thin, and experience flotation due to increased ocean water exposure (Van Wychen et al., 2020b).

Coincident with this extreme retreat rate increase, marine-terminating glaciers of the QEI's Axel Heiberg and Ellesmere Islands have exhibited a general trend of decelerated flow and decreased dynamic discharge (Van Wychen et al., 2016). Dynamic discharge is defined as the mass passing through a terminus flux gate per unit time, i.e., mass loss in the form of iceberg calving. Despite this widespread reduction of dynamic discharge from many glaciers, overall ice loss from the QEI has held relatively constant from 2000–2015 (Millan et al., 2017). This seemingly illogical fact is possible due to the anomalous behaviour of just two glaciers, Trinity and Wykeham. These glaciers have become the subject of extensive research in the region, and as such will be the subjects discussed for the remainder of this paper.

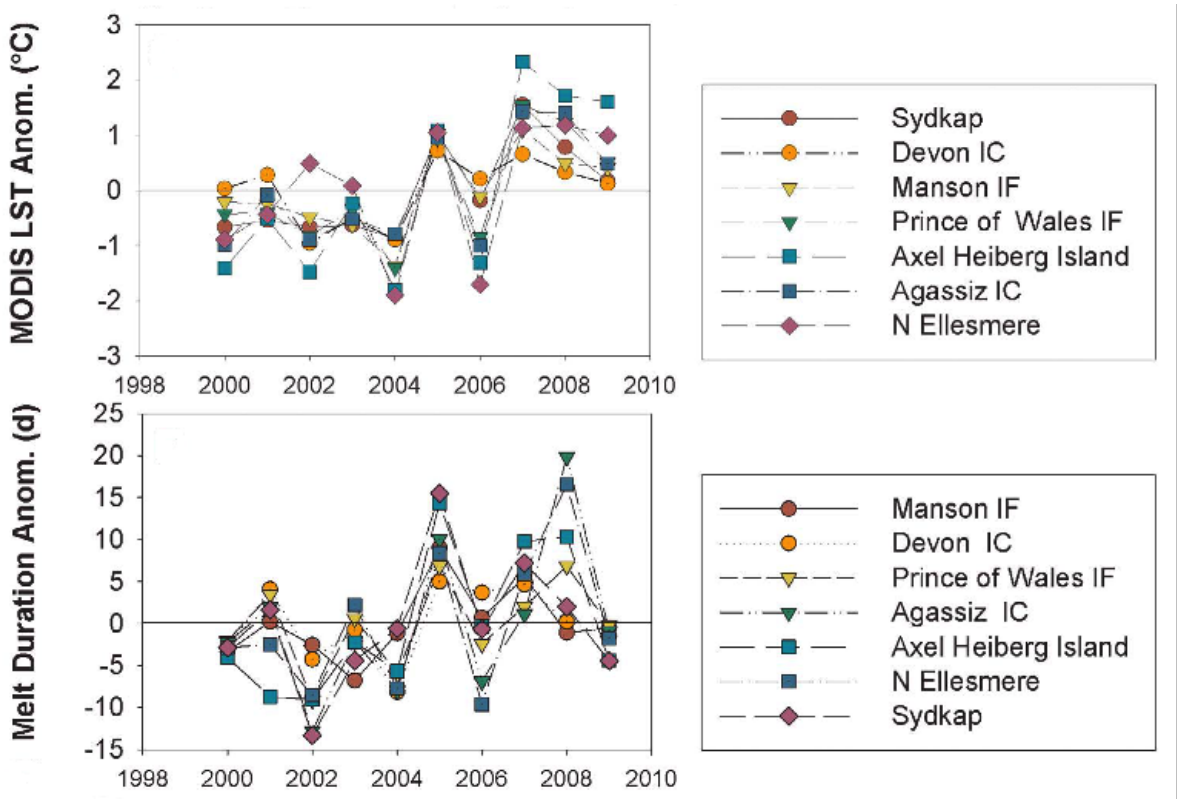

Figure 1.2: Annual anomalies (relative to the 2000–2009 mean) in (top) mean summer MODIS land surface temperature and (bottom) melt season duration between 1998 and 2010 for multiple glaciated areas of the CAA. Adapted from Sharp et al. (2011).

1.3.2 Trinity-Wykeham Glaciers, Nunavut, Canada

Trinity-Wykeham Glaciers, located in the Prince of Wales Icefield (POW) along the central-east of Ellesmere Island (see Figure 1.3, marked in red in Figure 1.1) are marine-terminating temperate glaciers that have undergone acceleration, retreat, and thinning in the 21st century unparalleled by any glaciers in the CAA (Cook et al., 2019; Van Wychen et al., 2016, 2020b). Many glaciers on Axel Heiberg and Ellesmere Island have been identified as surge-type glaciers, meaning they cycle through periods of rapid acceleration and advance, termed the active phase, and periods of flow slower than the balance velocity, termed the quiescent phase (Van Wychen et al., 2016). It was once thought that Trinity-Wykeham Glaciers, due to their sudden increase in velocity, were surge-type glaciers (Short and Gray, 2005). However, Trinity-Wykeham Glaciers are the only glaciers in the region to accelerate

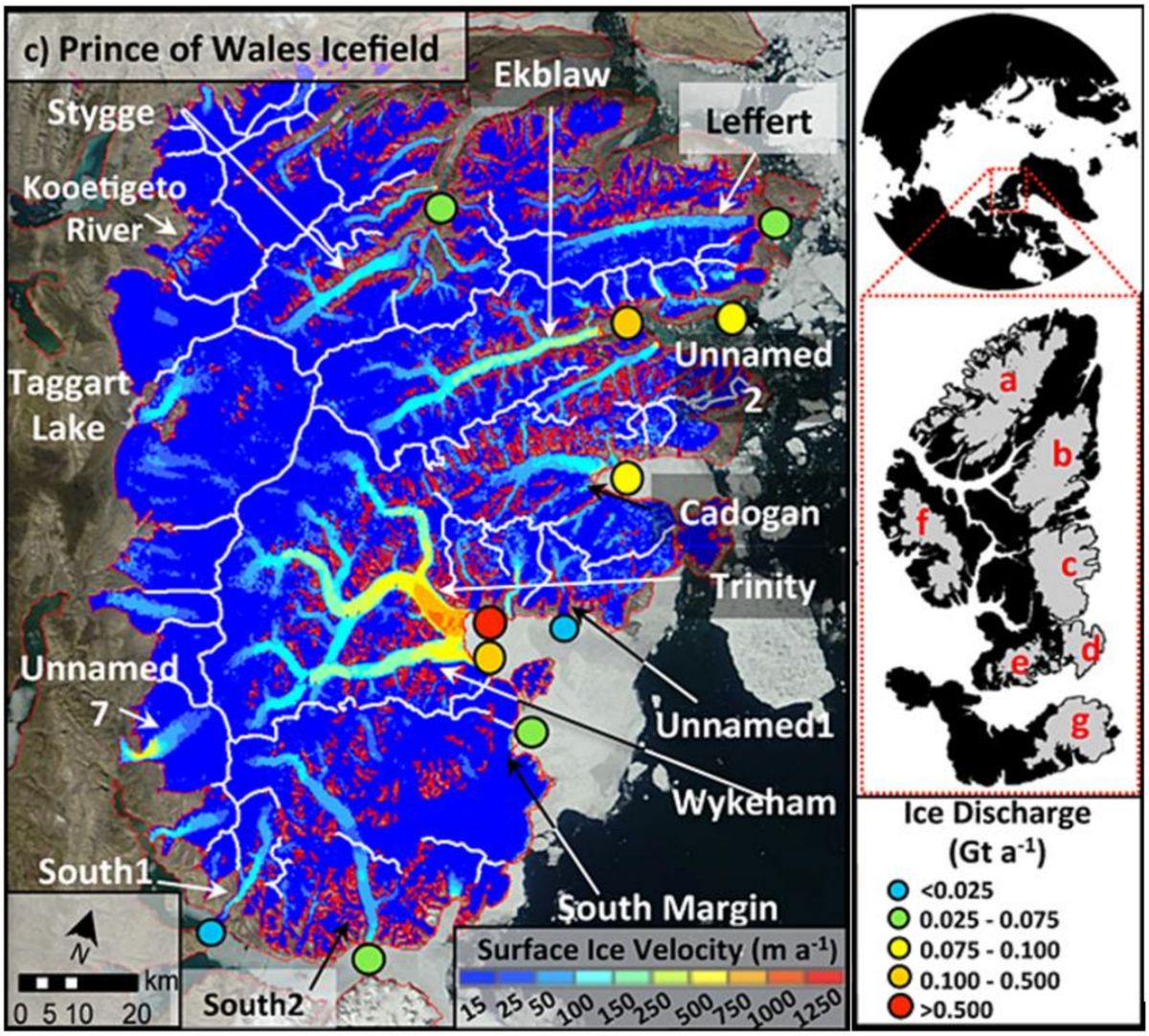

Figure 1.3: Surface velocity and ice discharge map of the Prince of Wales Icefield, along with its relative location in the Queen Elizabeth Islands. Adapted from Van Wychen et al. (2014).

consistently (without quiescent phases) since 1999, more than doubling their respective surface velocities between 1999 and 2015 (Van Wychen et al., 2016). Trinity-Wykeham Glaciers have achieved flow rates greater than 1200 and 600 m/yr, respectively, making them the two fastest-flowing glaciers in the entire CAA (Van Wychen et al., 2020b). This

significant acceleration has been accompanied by extensive terminus retreat of $\sim$ 3–4 km for Trinity and $\sim$ 1 km for Wykeham. This retreat is in direct contrast to the advancement typically seen in surge-type glaciers. Additionally, the surge of a glacier should result in an increase of mass at the terminus as the ice bursts downglacier. However, Dalton et al. (2022) report that the surface elevation at the termini of both glaciers decreased by over 20 m between 2010 and 2020. These high rates of thinning near the termini further differentiates the behaviour of Trinity-Wykeham Glaciers from that of surge type glaciers. The rapid retreat and acceleration of Trinity-Wykeham Glaciers have resulted in enough dynamic discharge to compensate for the region-wide decrease in dynamic discharge over the same period. In 2015, $\sim$ 64% of all dynamic discharge from Ellesmere and Axel Heiberg Islands, along with $\sim$ 58% of all iceberg plume events in the POW Icefield, came from Trinity-Wykeham Glaciers alone (Dalton et al., 2019; Van Wychen et al., 2016).

It is evident that regional temperature increases, likely augmented by anthropogenic activity, are driving the melt and retreat of QEI glaciers (Cook et al., 2019; Sharp et al., 2011; Zemp et al., 2019). However, for reasons not immediately apparent, Trinity-Wykeham Glaciers have diverged drastically over the last two decades from trends in glacier dynamics both in the immediate proximity of the POW Icefield and the CAA as a whole.

1.3.2.1 Observed Changes in Dynamics

One of the topics of greatest interest regarding Trinity-Wykeham Glaciers is their anomalous ice flow velocities. They are the only two glaciers in the QEI that currently flow at over 1 km/yr (Van Wychen et al., 2020b), and both exhibit strong seasonality in their respective flow regimes, as can be seen in Figure 1.4 which shows seasonal velocity patterns for both glaciers between 2013 and 2016. Both glaciers experience their peak velocities in the spring, increasing by 300 m/yr for Trinity Glacier and 100 m/yr for Wykeham Glacier between 2013 and 2016. Figure 1.5 provides RADARSAT-2 derived winter surface velocities for both glaciers between 2008 and 2020. Trinity, the larger and faster of the two glaciers, increased in winter velocity through this period, with a peak of $\sim$ 1200 m/yr in the winter of 2018/2019. Velocities at the lower 10 km of the glacier did not fall below 800 m/yr. This increase in speed has seemingly propagated upglacier in recent years, with the velocities in nearly the entire lower 30 km of the trunk exceeding 400 m/yr in 2018/2019 (Van Wychen et al., 2020b). In each year from 2013 to 2016, winter velocities at Trinity Glacier's lower 20 km exceeded summer velocities, which slowed by 200–300 m/yr in that period (Harcourt et al., 2019). Wykeham Glacier displayed similar velocity patterns. The lower 5 km of Wykeham Glacier accelerated from $\sim$ 500–600 m/yr in the winter of 2015/2016 to $\sim$ 700–800 m/yr in the winter of 2019/2020 (Van Wychen et al., 2020b).

The section of Wykeham Glacier's trunk 10–20 km from the grounding line also accelerated by about 200 m/yr in that time, but the terminus of Wykeham Glacier exhibits a year-round deceleration anomaly, consistently flowing less than 100 m/yr (Harcourt et al., 2019). Conversely to Trinity Glacier's behaviour, summer velocities at Wykeham Glacier exceeded those in the winter up until 2016, when the summer velocity decreased by $\sim$ 100 m/yr (Harcourt et al., 2019).

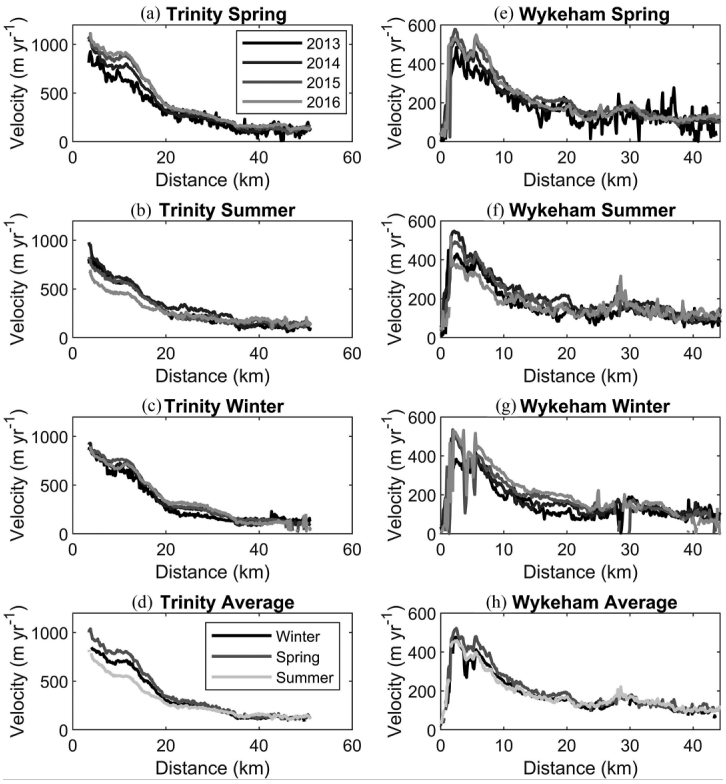

Figure 1.4: Seasonal velocity estimates between 2013 and 2016 for Trinity Glacier (a-d) and Wykeham Glacier (e-h). Spring (April to June) velocity estimates are shown in panels (a) and (e). Summer (July to September) velocity estimates are shown in panels (b) and (f). Winter velocity (October to March) estimates are shown in panels (c) and (g). Panels (d) and (h) show seasonal velocity along each glacier averaged between 2013 and 2016. Adapted from Harcourt et al. (2019).

In their investigation of iceberg plume events in the Prince of Wales Icefield between 1997 and 2015 using synthetic aperture radar (SAR) and optical satellite imagery, Dalton et al. (2019) determined that the ice flux of Trinity-Wykeham Glaciers doubled between

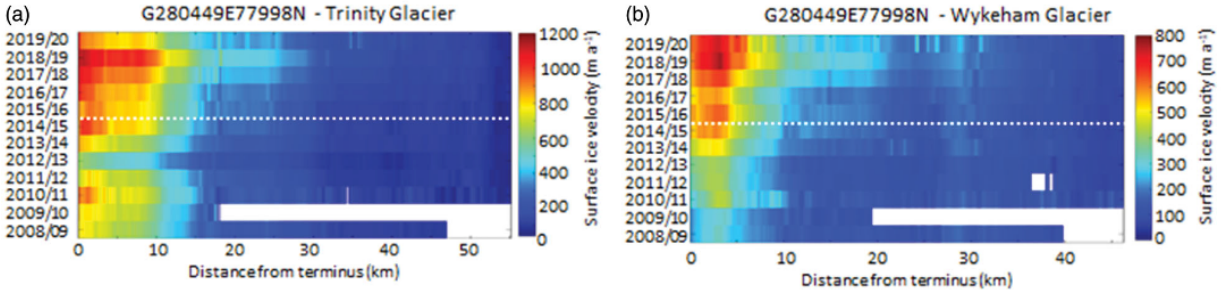

Figure 1.5: Variations in winter surface ice velocities over the RADARSAT-2 observation period (2008–2020) for (a) Trinity and (b) Wykeham Glaciers. Results provided below white dashed line were derived by Van Wychen et al. (2016). Adapted from Van Wychen et al. (2020b).

2005 and 2015. The majority of glaciers in POW Icefield produced fewer than 10 plume events in the period of the study, but Trinity-Wykeham (the most active) produced 139 and 134 respectively, with Trinity producing 11 "magnitude 3" (20–30 km^2) plume events, more than any other glacier in the study. It was found that the glaciers with more plume events often underwent greater retreat, which may suggest retreat patterns could be a direct control on such events, or perhaps that factors driving glacier retreat may also be driving plumes. Figure 1.6 depicts the ice discharge of 57 QEI glaciers in the winter of 2019/2020, with Trinity-Wykeham Glaciers accounting for 1.602 GT/yr out of 3.203 Gt/yr, over 50% of the total (Van Wychen et al., 2020a).

Before the year 2000, a general trend of gradual retreat was observed across the CAA. In the years since, retreat rates in the region have quickly increased to about five times the mean before 2000. The greatest absolute rates of retreat were those of Trinity-Wykeham Glaciers, which retreated ~ -255 m/yr between 2009 and 2015 (Cook et al., 2019). Trinity-Wykeham Glaciers have also undergone substantial thinning in recent years, most dramatically at their respective termini. Glaciers in the northern Canadian Arctic exhibited a mean elevation change rate of -0.40 ± 0.05 m/yr between 2010 and 2014 (Hugonnet et al., 2021). Van Wychen et al. (2016) found that the lower ~ 15 km of Trinity Glacier thinned ~ 2–5 m/yr between 2008 and 2014, with similar rates of thinning near the front of Wykeham Glacier (see Figure **??**). This is 500–1250% the regional average reported by Hugonnet et al. (2021), and two other unnamed glaciers ~ 8 km and ~ 15 km from the front of Trinity-Wykeham were found to have lowered by an average of ~ 0.61 m/yr in this same period (Van Wychen et al., 2016). This indicates that there may be factors specific to Trinity-Wykeham causing extreme thinning. According to Van Wychen et al. (2016), at least half of the observed thinning rate at the terminus of Trinity Glacier can be attributed

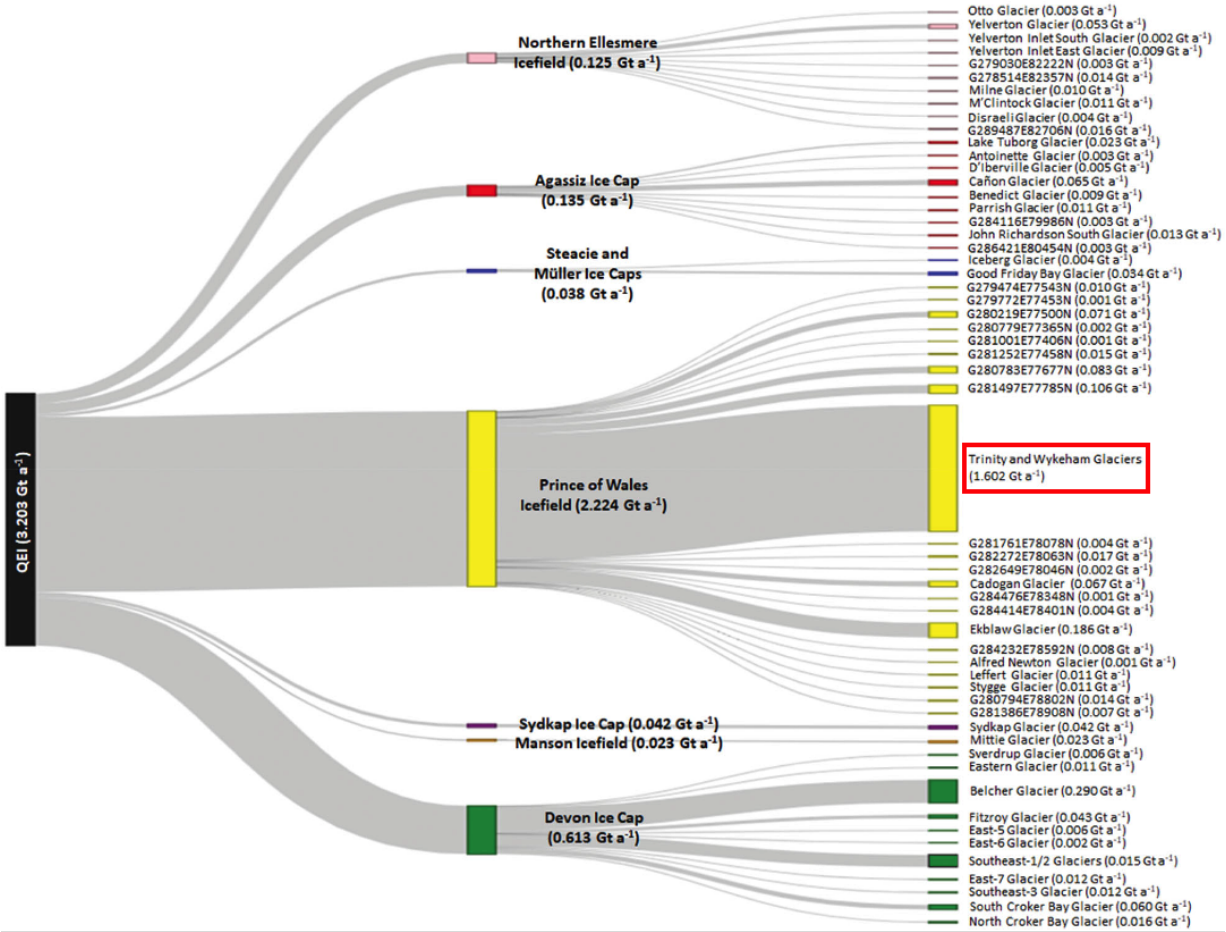

Figure 1.6: Distribution of ice discharged to the ocean from the ice masses of the Queen Elizabeth Islands, broken down by ice mass and glacier, for winter 2019/2020. GLIMS ID provided for unnamed glaciers. The red rectangle denotes the contribution from Trinity-Wykeham Glaciers. Adapted from Van Wychen et al. (2020a).

to variations in ice dynamics.

1.3.2.2 Bedrock Topography and Subglacial Hydrology

It is suggested that the geometry of the bedrock base beneath Trinity-Wykeham Glaciers is key in explaining their significant acceleration and the seasonality therein. In the interior regions of QEI glaciers, velocities are generally low (< 20 m/yr), suggesting that ice in

these regions is frozen to its base and flowing by internal deformation, or creep, alone (Van Wychen et al., 2020b). Along the main trunk of outlet glaciers, ice-penetrating radar measurements indicate that valleys in the QEI are carved deep into the underlying bedrock. This allows the ice to thicken as it is channelled from the larger caps into these valleys, increasing driving stress and causing velocities to increase, typically reaching 50–100 m/yr (Van Wychen et al., 2020b). This acceleration may indicate that the increased overburden pressure exerted by the thickened ice lowers the pressure melting point at the bed, resulting in subglacial water and, in turn, enhanced basal sliding. Figure 1.7 from Harcourt et al. (2019), a study of subglacial controls on dynamic thinning at Trinity-Wykeham Glaciers, shows the bedrock topography of the glaciers. Trinity Glacier has two overdeepenings along its trunk, likely eroded by the glacier's motion, labelled troughs #1 and #2. Wykeham Glacier has a series of overdeepenings that create an undulating bed, along with multiple sets of ridges, labelled #1–4, that jut out from the glacier margins perpendicular to ice flow. These ridges increase basal friction, thereby explaining Wykeham Glacier's lower velocity with respect to Trinity. The troughs and overdeepenings found in the bed of both glaciers create a reverse slope in areas, i.e., ice flows up-slope as it travels downglacier. A reverse slope can reduce ice stability, allow ocean water to penetrate the ice-bedrock interface, and cause rapid retreat, much like that observed at Trinity-Wykeham Glaciers (Harcourt et al., 2019; Schoof, 2007; Weertman, 1974). In addition to this, both glaciers feature a "pinning point," or an elevated region of topography, at their termini, which directly impedes the flow of ice from their respective fronts. In fact, the pinning point at Wykeham Glacier's terminus causes ice flow to diverge into two separate flow units and may be responsible for the deceleration anomaly observed at the glacier's terminus (Harcourt et al., 2019).

Harcourt et al. (2019) and Van Wychen et al. (2020b) postulate that subglacial topography is largely responsible for the rapid changes in the dynamics of Trinity-Wykeham Glaciers. Both glaciers are grounded below sea level approximately 45 km upglacier (Van Wychen et al., 2020b). Consequently, changes in velocity at their respective fronts may propagate upglacier much more rapidly due to decreased resistive forces, and this has been observed in recent velocity measurements (Harcourt et al., 2019; Van Wychen et al., 2020b). It has been suggested that because the lower areas of the glaciers are grounded below sea level, enhanced thinning of Trinity-Wykeham Glaciers has resulted in the ungrounding and partial flotation of their respective fronts, a claim supported by measurements of hydrostatic flotation depth in the area, analysis of surface crevassing patterns, and the fact that current winter velocities mirror maximum summer velocities in years prior (Harcourt et al., 2019; Van Wychen et al., 2020b). Flotation of the glaciers' fronts increases their contact with ocean waters and reduces the forces that resist flow, making them susceptible to further dynamic thinning, retreat, and ice discharge. Dynamic thin-

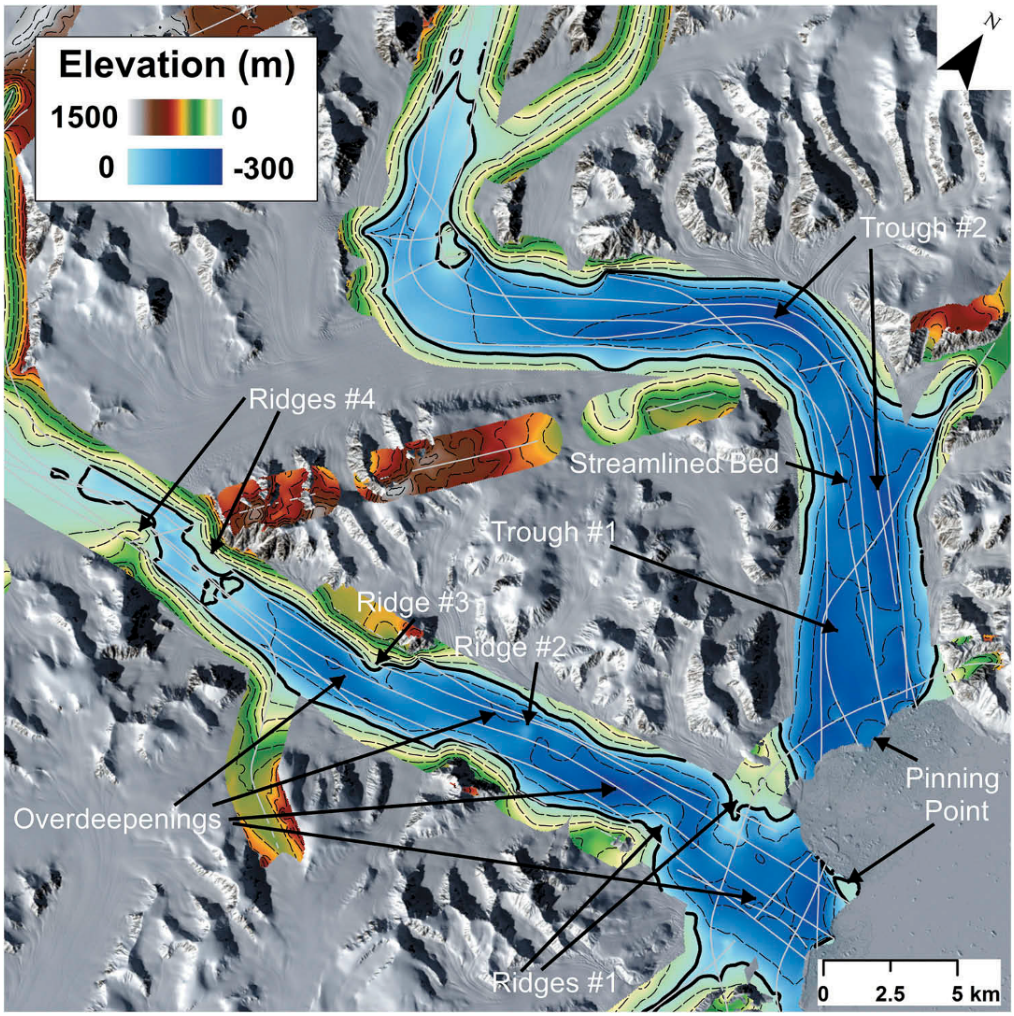

Figure 1.7: Bedrock topography derived from Natural Neighbour interpolation of the CAGE-OIB ice thickness measurements and subtracted from the ArcticDEM of ice surface elevation. Annotations describe key geomorphological features of the subglacial topography. Dashed lines show 100 m elevation contours and the bold line represents sea level (0 m). The CAGE-OIB flight lines are superimposed in light grey. The background image is a Landsat 8 natural colour image from 5 May 2014. Adapted from Harcourt et al. (2019).

ning is further influenced by subglacial features present at the bases of Trinity-Wykeham Glaciers. Trinity Glacier's troughs serve to redirect and channelise the ice, which leads to accelerated flow and dynamic extensional thinning. The ridges that extend from the

margins of Wykeham Glacier obstruct glacier flow and cause local thickening of ice, which leads to greater driving stress, flow speed, and dynamic thinning on the lee side of the ridge (Harcourt et al., 2019). The surfaces of the two glaciers feature supraglacial lakes that form in regions of heavy crevassing coincident with subglacial ridges. These lakes appear in June as the summer temperatures drive melt, and disappear by August (Harcourt et al., 2019). It is suggested that once enough pressure builds up, meltwater drains through crevasses or moulins at the floor of the lake and travels directly to the bed, concurrent with observed minima in summer velocity.

1.3.2.3 Oceanic Warming, Atmospheric Warming, and Arctic Amplification

There is strong evidence that dynamic discharge, retreat, and general mass loss of marine-terminating glaciers in the North Pole are strongly controlled by oceanic temperatures (Carr et al., 2013a). Subaqueous melt can cause severe undercutting of submerged glacier fronts, which leads in turn to enhanced retreat and calving at the terminus. In recent years, the Arctic Ocean and bodies of water connected thereto have undergone significant warming (Zweng and Münchow, 2006). This includes Baffin Bay, where rising subsurface temperatures have led to the rapid retreat of marine-terminating glaciers in western Greenland (Cook et al., 2019). Subaqueous melt rates in this region exceed surface melt rates by two orders of magnitude (Rignot et al., 2010). Similar dominance of subaqueous melt has been observed on the Antarctic Ice Sheet (Truffer and Motyka, 2016).

Subaqueous melt is driven by warm (i.e., above the freezing point) plumes of ocean water coming in contact with submerged ice at the glacial front. Waters above 1°C are found at all depths on the southwest coast of Greenland, consistent with the observed melt rates (Cook et al., 2019). Contrary to this, waters up to 200 m deep are generally below −1°C throughout the CAA. Specifically, in-situ measurements of mean ocean temperature from the World Ocean Database indicate that water temperatures were sub-zero within 100 km of the POW Icefield between 1970 and 2010 at all depths (Cook et al., 2019). This difference in temperature can be attributed to cyclonic circulation in northern Baffin Bay which transports cold Arctic waters along the east of Baffin Island and warm Atlantic waters northward along western Greenland (Cook et al., 2019). Because of this, Cook et al. (2019) determined that mean ocean temperatures were insufficient to drive the extreme retreat observed at Trinity-Wykeham Glaciers. In line with these findings, Dalton et al. (2019) suggest that it is likely that changes in ocean temperature did not play a significant role in the melting of the calving front nor in iceberg production at Trinity-Wykeham Glaciers, although without an abundance of long-term ocean temperature measurements at the termini of individual glaciers, this conclusion is not absolute.

With subaqueous melt effectively ruled out, we now consider warming atmospheric temperatures as a potential driver of Trinity-Wykeham Glaciers' dynamics. Since 2005, strong summer warming has occurred in the QEI, from 1.1° C in 2000–2004 to 1.6°C in 2005 at 700 hPa (Sharp et al., 2011). The succession of warm summers has resulted in elevated glacier surface temperatures, increased melt season duration (associated with total annual positive degree-days), and surface mass balances nearly five times more negative than the mean between 1963 and 2004 (Sharp et al., 2011). Mass loss has been dominated by enhanced surface runoff due to melting since 2005, with only 10% of mass loss due to ice discharge (Millan et al., 2017). 1-km downscaled RACMO2.3 data demonstrates a significant correlation between frontal retreat of marine-terminating glaciers and components of surface mass balance, namely mean ablation rate, ablation area ratio, and most significantly mean runoff, with changes in surface runoff and retreat essentially synchronous (Cook et al., 2019). This relationship between surface mass balance components and glacier retreat rates indicates that atmospheric warming in the North has led to the rapid retreat of Trinity-Wykeham Glaciers, and why changes to the two glaciers have occurred relatively suddenly, as opposed to on a decadal scale.

Arctic amplification has exacerbated the atmospheric temperature rise observed in the CAA in the twenty-first century. One of the main contributing factors to Arctic amplification is thought to be a reduction in surface albedo that has arisen from diminished ice surface area on land and sea in northern regions. Fresh snow has a very high albedo of 0.80 to 0.97, which is very good at reflecting shortwave radiation. This naturally degrades over time due to melt, snow metamorphism, and debris cover. Decreasing albedo results in higher shortwave absorption, which increases melt and snowpack water content, leading to more rapid albedo reduction. Glacial surface warming and melt in the summer can cause a more intense and rapid ablation period which leads to longer exposure of the underlying glacier ice which has a lower albedo than the accumulated snow. This leads to increased absorption of shortwave radiation, which drives further melt in a "positive ice-albedo feedback" (Mortimer and Sharp, 2018). Mortimer and Sharp (2018) used measurements from Moderate Resolution Imaging Spectroradiometer (MODIS) sensors to determine spatial and temporal patterns in summer (melt season) albedo for glaciers in the Queen Elizabeth Islands from 2001 to 2016. Mean summer black-sky shortwave albedo (BSA) decreased by approximately 0.0029 ± 0.0025 yearly, with the majority of albedo decline likely having occurred between 2007 and 2012 as indicated by strong BSA anomalies in this period. The largest drops in BSA occurred in July, with no changes occurring in June or August. This is likely linked to atmospheric circulation patterns that affect the QEI in July, as supported by the North Atlantic Oscillation index. Mean summer BSA reduction was largest at the margins of ice masses (where Trinity-Wykeham Glaciers are located). BSA

changes throughout the study period correlated with the 16-year record of mean summer land surface temperatures, indicating the aforementioned positive ice-albedo feedback which has caused mass loss rates to accelerate in the QEI (Mortimer and Sharp, 2018). This enhanced melt partially explains the dramatic thinning that has been observed on Trinity-Wykeham Glaciers since the beginning of the 2000s, in conjunction with dynamic thinning mechanisms.

Rising albedos in the Arctic also have an apparent effect on dynamic discharge from Trinity-Wykeham Glaciers. Arctic amplification is strongest in the autumn and winter when excess summer heat is transferred from the ocean to the lower atmosphere via turbulent fluxes and radiation (Cohen et al., 2014). The additional heat slows the formation of sea ice throughout the winter in both extent and thickness, which then allows the ocean to absorb even more energy through the summer, as it has a much lower albedo than the ice. In other words, it seems that a loss of sea ice is both a direct cause and outcome of Arctic amplification. Almost half of all plume events in the POW Icefield between 1997–2015 occurred in the summer open water season (where little sea ice is present) that lasts only 21% of the year, and plumes exceeding 20 km^2 almost never occurred outside of this season (Cook et al., 2019). This may indicate a strong correlation between the presence of sea ice and iceberg production, likely due to the buttressing effect of sea ice on the motion of outlet glacier ice through the terminus (Carr et al., 2013b; Cook et al., 2019; Dalton et al., 2019). Alternatively, it could be the case that iceberg plumes are simply more difficult to detect in the presence of extensive sea ice. The decrease in sea ice extent combined with the high velocity of Trinity-Wykeham Glaciers is a likely explanation for their dominance of dynamic discharge within the CAA.

1.4 Thesis Layout

The aim of this thesis is to investigate the regionally atypical dynamics of Trinity-Wykeham Glaciers from a hydrological perspective. The Glacier Drainage System (GlaDS) subglacial hydrology model is used to examine the development of hydrological networks at the base of each glacier in response to realistic meltwater input. In simulating the subglacial hydrology of these glaciers, valuable insight into subglacial processes at tidewater glaciers will be gained, and the advantages and shortcomings of the GlaDS model will be made evident. As the first application of coupled two-dimensional distributed and channelized subglacial hydrology in the Canadian High Arctic, this project sets a precedent for future studies of glacier hydrology and dynamics in a rapidly changing area of the cryosphere.

Chapter 2 details the tools and procedures used in simulating subglacial hydrology at

Trinity-Wykeham Glaciers. The chapter begins with an overview of the GlaDS model (Werder et al., 2013), detailing the structure of the distributed and channelized drainage systems and the equations governing the motion of water therein. The numerical solution of the model equations through weak formulation is then described. The data and procedure used in running the model are discussed along with the method used to compare glacier surface velocities to subglacial water pressure outputs.

Chapter 3 presents the main findings of the subglacial hydrology simulations. The spatial and temporal evolution of model outputs including subglacial water pressure, distributed "water sheet" thickness, and channel discharge are analysed to gain insight into the effects of variable meltwater input to the subglacial system at Trinity-Wykeham Glaciers on both a seasonal and interannual timescale. Subglacial water pressure outputs are then compared with satellite-derived surface velocities over three years to investigate the possible influence of subglacial hydrology on the dynamics of the glaciers. Finally, outputs from nine different model runs are presented as a means of testing the sensitivity of the GlaDS model to variations in sheet conductivity and channel conductivity—two parameters controlling the ease of flow through the distributed and channelized systems respectively.

Chapter 4 delves into the findings that can be taken from the results presented in Chapter 3. The general patterns observed in subglacial hydrology outputs are interpreted in the context of an evolving subglacial environment. These patterns are also compared and contrasted with in-situ hydrological measurements and observations at various tidewater glaciers in the Arctic. The results of the sensitivity tests are then discussed, providing insight into how conductivity parameters change the outputs of the GlaDs model and suggesting a useful range of values for these parameters to be used in future applications of GlaDS. The wider implications of the simulation are then discussed, including what the model indicates about the future behaviour of Trinity-Wykeham Glaciers and other similar tidewater glaciers in the Canadian Arctic Archipelago in a warming Arctic climate. Finally, a number of limitations faced in this project are explored including restrictions related to the GlaDS model and the availability of in-situ data, and future projects and methods for improving predictions are suggested.

Chapter 5 is the final chapter of this thesis. The chapter is a review of the goals of this project and summarises the major conclusions drawn from its outcomes regarding the future behaviour of Trinity-Wykeham Glaciers and the way forward for subglacial hydrology modelling in tidewater glaciers in the Canadian Arctic.

Chapter 2

Methodology

This chapter details the method for modelling subglacial hydrology at Trinity-Wykeham Glaciers between the years 2016 and 2019. First, Section 2.1 describes the structure, constituent equations, and solution of the GlaDS hydrology model, including descriptions of the distributed (Subsection 2.1.1) and channelised (Subsection 2.1.2) drainage systems. Then, the data used as inputs to the model in order to simulate the behaviour of Trinity-Wykeham Glaciers are discussed in Section 2.2. The multiple procedures for running models, including steady state, primer, and meltwater input runs, are presented in 2.3. Finally, Section 2.4 describes the comparison of glacier surface velocity data to modelled basal water pressure outputs.

2.1 The GlaDS Subglacial Hydrology Model

Subglacial hydrology modelling of Trinity-Wykeham Glaciers is performed in two dimensions with the Glacier Drainage System model (GlaDS) (Werder et al., 2013). This decision was made because GlaDS couples distributed and channelised subglacial drainage systems; this is particularly important at Trinity-Wykeham Glaciers, as there are indications of a subglacial hydrology system that transitions between distributed and channelised states, including rapid surface velocity decreases and supraglacial lake drainage events at the height of the melt season (Harcourt et al., 2019). Water transport at the bed can be a powerful control on glacier dynamics and dynamic discharge, and thus the ability of the GlaDS model to capture the shift between efficient and inefficient drainage is indispensable.

GlaDS has been widely tested and applied in the context of glaciers and ice sheets (Cook et al., 2020, 2022; Ehrenfeucht et al., 2023; Poinar et al., 2019; Scholzen et al.,

2021). However, coupled two-dimensional distributed and channelised subglacial hydrology has not been previously applied in the Canadian High Arctic. The GlaDS model is applied through the Ice-sheet and Sea-level System Model (ISSM) (Larour et al., 2012). ISSM is a thermomechanical finite element ice flow model that includes higher-order stress components, high spatial resolution capability, and high performance power owing to parallelised architecture linked to the Message Passing Interface MPI (Gropp and Lusk, 1996; Gropp et al., 1996) and the PETSc libraries.

The GlaDS model relies numerically on a two-dimensional finite element method which is applied to an unstructured, triangular mesh (see Figure 2.1). The channel network Γ is made up of channel segments Γ_j that form along the edges of the mesh and divide the domain Ω into triangular elements Ω_i that comprise the distributed system. The distributed system is represented as a continuous sheet of water beneath the glacier; each element carries a discrete "sheet thickness." The channelised drainage system is represented as a linked network of channels. Channel segments are permitted to form on all edges of the domain other than those on the domain boundary, denoted $\partial\Omega$. Water is conducted from one channel to another at mesh vertices or "nodes" Λ_k, and exchanged with adjacent distributed system elements along the channel segments.

Water is conserved at each node such that all discharge flowing into the node must sum to zero. This requirement can be expressed as

$$\Sigma_j Q_j^k = 0, \tag{2.1}$$

where Q_j^k is the discharge flowing into node k from channel j, summed over all channels attached to the node. Additionally, all channel segments are adjacent to two sheet elements Ω_{i_1}, Ω_{i_2}. Flow into the channel from these elements must equal the channel source term m_c (defined below in Subsection 2.1.2), and so

$$m_c = \mathbf{q} \cdot \mathbf{n} \mid_{\partial\Omega_{i_1}} + \mathbf{q} \cdot \mathbf{n} \mid_{\partial\Omega_{i_2}}, \tag{2.2}$$

is required for each channel, where $\mathbf{n}$ is the normal vector to the channel segment.

The location and size of channels in the GlaDS model are not prescribed. Rising subglacial water pressure in the distributed system increases the hydraulic potential gradient, in turn driving faster water flow and allowing channels to form spontaneously. Likewise, areas with low subglacial water pressure are unlikely to host channels. Because of this, channels are allowed to form driven by observable factors such as bed topography and meltwater input, as opposed to a rigid, predetermined path. The use of an unstructured mesh was an express effort to maintain this low-bias approach to channel distribution and

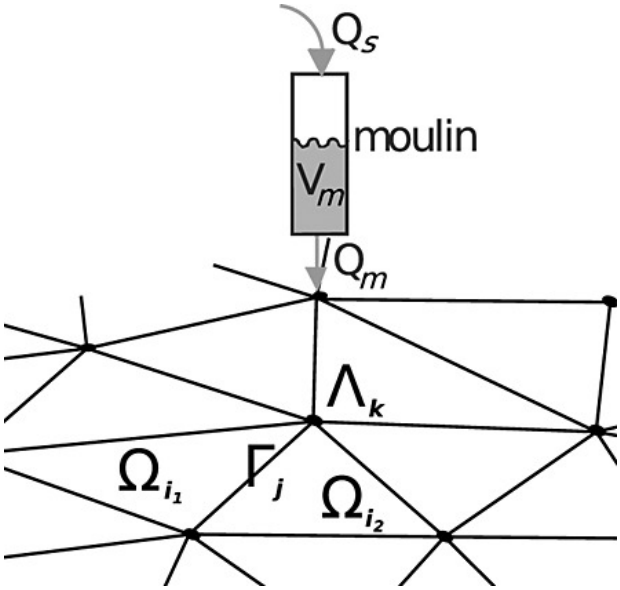

Figure 2.1: A view of part of a network Γ with a moulin connecting to one of the nodes. The network has edges Γ_j and nodes Λ_k, partitioning the domain Ω into subdomains Ω_i. The channels are constrained to lie on the edges and the sheet occupies the subdomains. The moulin has Q_s surface water input, Q_m discharge into network node, and a volume V_m. Adapted from Werder et al. (2013). Moulin input is not used for this project.

formation, although the mesh construction will cause some local bias dependent on the size and positioning of the elements. A full list of parameters used in discussing and running the model can be seen in Table 2.1, and the variables can be seen in Table 2.2.

Table 2.1: Parameters used in the GlaDS model. The absence of a value under "Default Value" indicates that the default value of a given parameter was used for this project.

Name	Symbol	Default Value	Used Value	Units
Ice hardness	B	$2.1 \cdot 10^8$	$8.3788 \cdot 10^7$	$\mathrm{Pa/s}^{1/n}$
Bed elevation	b	NaN	Variable	m
Pressure melt coefficient	c_t	-	$7.5 \cdot 10^{-8}$	K/Pa
Specific heat capacity of water	c_w	-	$4.22 \cdot 10^3$	J/kg K
Englacial void ratio	e_v	-	10^{-5}	-
Geothermal heat flux	G	NaN	0.15	$\mathrm{W/m}^2$
Acceleration due to gravity	g	-	9.81	$\mathrm{m/s}^2$
Ice thickness	H	NaN	Variable	m
Typical bedrock bump height	h_r	NaN	0.1	m
Channel conductivity	k_c	NaN	Variable	$\mathrm{m}^{3/2}\ \mathrm{kg}^{-1/2}$
Sheet conductivity	k_s	NaN	Variable	$\mathrm{m}^{7/4}\ \mathrm{kg}^{-1/2}$
Latent Heat	L	-	$3.34 \cdot 10^5$	J/kg
Channel width	l_c	NaN	Variable	m
Cavity spacing	l_r	-	2	m
Glen's law n	n	-	3	-
Channel flow law exponent	α_c	-	5/4	-
Sheet flow law exponent	α_s	-	5/4	-
Channel flow law exponent	β_c	-	3/2	-
Sheet flow law exponent	β_s	-	3/2	-
Density of ice	ρ_i	-	917	$\mathrm{kg/m}^3$
Density of water	ρ_w	1023	1000	$\mathrm{kg/m}^3$

Table 2.2: Variables used in the GlaDS model.

Name	Symbol	Units
Sheet thickness	h	m
Englacial storage	h_e	m
Channel source term	m_c	m^2/s
Sheet source term	m_b	m/s
Effective pressure	N	Pa
Normal vector	$\mathbf{n}$	m
Channel discharge	Q	m^3/s
Sheet discharge	$\mathbf{q}$	m^2/s
Sheet flow beneath channel	q_c	m^2/s
Channel cross-sectional area	S	m^2
Coordinate along edge	s	m
Time	t	s
Channel closure rate	v_c	m^2/s
Cavity closure rate	v_s	m/s
Cavity opening rate	w_s	m/s
Test function	θ	Pa
Channel press-melt	Ξ	W/m
Channel dissipation	Π	W/m
Basal stress	$\tau_{\mathbf{b}}$	Pa
Hydraulic potential	ϕ	Pa
Bed hydraulic potential	ϕ_m	Pa
Overburden hydraulic potential	ϕ_0	Pa

2.1.1 The Distributed Drainage System

Distributed drainage beneath a glacier is commonly assumed to take the form of a system of linked cavities. In the GlaDS model, this system is represented as a continuous sheet of water beneath the glacier, akin to that described in Hewitt (2011). The mass of water is conserved in the system, governed by the continuity equation

$$\frac{\partial h}{\partial t} + \nabla \cdot \mathbf{q} = m_b, \tag{2.3}$$

where h is the average sheet thickness, $\mathbf{q}$ is the sheet discharge, and m_b is the melt source term which describes both basal melt and surface water input. m_b is defined

$$m_b = \frac{G + |\tau_b \cdot \mathbf{u_b}|}{\rho_i L}, \tag{2.4}$$

where G is geothermal heat flux, $|\tau_b \cdot \mathbf{u_b}|$ is the frictional heating for basal stress τ_b and sliding velocity vector $\mathbf{u_b}$, ρ_i is the density of ice, and L is the latent heat of fusion (see Table 2.1 for values).

Sheet discharge $\mathbf{q}$ is related to the gradient of hydraulic potential ϕ at the bed:

$$\mathbf{q} = -k_s h^{\alpha_s} \left|\nabla\phi\right|^{\beta_s - 2} \nabla\phi, \tag{2.5}$$

where k_s is the sheet conductivity, and $\alpha_s = 5/4$ and $\beta_s = 3/2$ are flow law exponents defined as such to reflect turbulent flow as per the Darcy-Weisbach flow law (evidence for turbulent flow within cavities is discussed in Fountain and Walder (1998)). The Darcy-Weisbach equation is used to calculate the head loss (pressure drop) in a conduit due to friction, with a friction coefficient which dictates whether flow is laminar or turbulent. This friction coefficient is calculated based on the Reynolds number associated with the fluid, the roughness of the conduit, and other factors. Hydraulic potential is defined

$$\phi = \phi_m + p_w, \tag{2.6}$$

where $\phi_m = \rho_w g b$ is the elevation potential, ρ_w is the density of water, g is acceleration due to gravity, b is bed elevation, and p_w is water pressure.

Average sheet thickness h is calculated by averaging the thickness of cavities and their connective orifices over a sufficiently large area of the bed (one mesh element). It is assumed that cavities are always at 100% water capacity, and thus the sheet thickness evolves solely through the opening and closing of cavities as the glacier flows:

$$\frac{\partial h}{\partial t} = w_s - v_s, \tag{2.7}$$

where w_s and v_s are functions describing the opening and closing mechanisms. Cavities open when the glacier flows over bedrock bumps, and so the opening rate,

$$w_s(h) = \begin{cases} |\mathbf{u_b}|\,(h_r - h)/l_r, & \text{if } h < h_r, \\ 0, & \text{otherwise,} \end{cases} \tag{2.8}$$

depends on basal sliding speed $\mathbf{u_b}$, bedrock bump height h_r, and typical horizontal cavity spacing l_r. Cavity closure is related to hydraulic potential ϕ at the glacial bed, Effective pressure is the difference between the overburden hydraulic potential and the aforementioned hydraulic potential at the bed:

$$\begin{aligned} N &= \phi_0 - \phi \\ &= \phi_m + p_i - \phi_m - p_w \\ &= p_i - p_w, \end{aligned} \tag{2.9}$$

where $\phi_0 = \phi_m + p_i$ is the overburden hydraulic potential, $p_i = \rho_i g H$ is the ice overburden pressure, and H is the ice thickness. Cavities close through the viscous deformation of glacier ice, also known as "ice creep", which is dependent on N:

$$v_s(h, N) = \frac{2A}{n^n} h \left|N\right|^{n-1} N, \tag{2.10}$$

where A is the basal flow parameter related to ice hardness by $B = A^{1/3}$ (Larour et al., 2012), and n is the exponent in Glen's law (Glen, 1955). It is at this point that it should be noted that edits have been made to the model equations for the purposes of this project. At each time step in a simulation, the water sheet thickness h is added to the height of the bed b, and therefore, the surface elevation. This was done to account for the fact that hydraulic potential is dictated by the height of the subglacial water sheet's surface rather than the elevation of the bed.

Although the subglacial water sheet can accommodate some volume of water, the long timescale of cavity opening and closure does not capture other water storage phenomena that occur on a much faster, e.g., hourly, timescale such as the lag between peak daily surface melt rates and peak subglacial discharge at the terminus (Werder et al., 2013). Thus, an additional term representing englacial storage is added to the equation for the conservation of mass:

$$\frac{\partial h}{\partial t} + \frac{\partial h_e}{\partial t} + \nabla \cdot \mathbf{q} = m_b. \tag{2.11}$$

This additional term is representative of water flowing into or out of the system through an englacial aquifer, and is thus directly proportional to changes in water pressure at the bed:

$$h_e(p_w) = \frac{e_v p_w}{\rho_w g}. \tag{2.12}$$

Here, e_v is the englacial void ratio.

2.1.2 The Channelised Drainage System

Subglacial channels in the GlaDS model follow Röthlisberger's description of semicircular channels melted into the sole of the glacier, referred to as R-channels (Röthlisberger, 1972). The GlaDS model encompasses many defining characteristics of the channelised subglacial drainage network, such as the mechanisms of channel opening and closure, the gradual and arborescent growth of the network, and the control of hydraulic potential over the rate and direction of flow within the system.

As in the distributed system, the growth of an R-channel is governed by the conservation of water mass:

$$\frac{\partial S}{\partial t} + \frac{\partial Q}{\partial s} = \frac{\Xi - \Pi}{\rho_w L} + m_c, \tag{2.13}$$

where S is the cross-sectional area of the channel, Q is channel discharge, s is a spatial coordinate oriented along the flow direction, Ξ is the rate of dissipation of potential energy per unit length of channel, Π is the rate of change of sensible heat per unit length of channel, and m_c is a source term representative of the water entering the channel from adjacent elements of the distributed system.

Analogous to sheet thickness h in the distributed system, the cross-sectional area S of a channel is subject to opposing rates of opening and closure. The evolution of S follows the equation

$$\frac{\partial S}{\partial t} = \frac{\Xi - \Pi}{\rho_i L} - v_c, \tag{2.14}$$

with opening rate $\frac{\Xi - \Pi}{\rho_i L}$ and closure rate v_c. Channels open through two means. The dissipation of potential energy Ξ is given by

$$\Xi = \left| Q \frac{\partial \phi}{\partial s} \right| + \left| l_c q_c \frac{\partial \phi}{\partial s} \right|. \tag{2.15}$$

Here, the first term accounts for water within the channel, and the second accounts for the portion of the water sheet of width l_c lying below the channel.

$$q_c = -k_s h^{\alpha_s} \left| \frac{\partial \phi}{\partial s} \right|^{\beta_s - 2} \tag{2.16}$$

approximates the sheet discharge flowing in the direction of the channel. The sensible heat

change Π of the water is defined as

$$\Pi = -c_t c_w \rho_w (Q + f l_c q_c) \frac{\partial p_w}{\partial s} \tag{2.17}$$

where c_t is the pressure melt coefficient (also known as the Clapeyron slope), c_w is the specific heat capacity of water, and once again the contribution from the underlying sheet of width l_c is addressed. As channel width cannot assume negative values, the term f acts as a switch to allow/disallow the contribution of sheet flow to refreezing:

$$f = \begin{cases} 1, & \text{if } S > 0 \text{ or } q_c \frac{\partial p_w}{\partial s} > 0 \\ 0, & \text{otherwise.} \end{cases} \tag{2.18}$$

Channels close due to viscous ice creep, and the rate at which this occurs is dependent on cross-sectional area S and effective pressure N:

$$v_c(S, N) = \frac{2A}{n^n} S \left| N \right|^{n-1} N. \tag{2.19}$$

As in the distributed system, channel discharge Q is tied to the hydraulic potential gradient, a relationship best described through the Darcy-Weisbach turbulent flow parameterisation with $\alpha_c = 5/4$ and $\beta_c = 3/2$:

$$Q = -k_c S^{\alpha_c} \left| \frac{\partial \phi}{\partial s} \right|^{\beta_c - 2} \frac{\partial \phi}{\partial s}. \tag{2.20}$$

Channel conductivity k_c indicates the ease with which water is transported through a channel. Since channels in the GlaDS model are semi-circular, k_c can be related to the Darcy-Weisbach friction factor f_r as follows (Werder et al., 2013):

$$k_c^2 = \frac{8}{\rho_w f_r (2/\pi)^{1/2} (\pi + 2)}. \tag{2.21}$$

2.1.3 Summary of Model Equations

Two sheet equations apply to every subdomain Ω_i of the mesh. The first is an equation governing hydraulic potential ϕ, obtained through combining 2.7, 2.11, and 2.12:

$$\frac{e_v}{\rho_w g} \frac{\partial \phi}{\partial t} + \nabla \cdot \mathbf{q} + w_s - v_s - m_b = 0, \tag{2.22}$$

or, more explicitly in parabolic form,

$$\frac{e_v}{\rho_w g}\frac{\partial \phi}{\partial t} + \nabla \cdot \left(-k_s h^{\alpha_s} \left|\nabla \phi\right|^{\beta_s - 2} \nabla \phi\right) + w_s - v_s - m_b = 0, \tag{2.23}$$

where sheet discharge $\mathbf{q}(h, \nabla\phi)$ is given by 2.5, and cavity opening and closing terms $w_s(h)$ and $v_s(h, N)$ are given by 2.8 and 2.10 respectively. The second sheet equation is the time evolution equation for local sheet thickness h, here written explicitly by combining 2.8 and 2.10:

$$\frac{\partial h}{\partial t} = w_s - v_s = \frac{\mathbf{u_b}(h_r - h)}{l_r} - \frac{2A}{n^n} h \left|N\right|^{n-1} N. \tag{2.24}$$

One should note that the first term on the right-hand side is equal to 0 when $h \geq h_r$.

Each channel segment Γ_j is also subject to two governing equations. The first of these is an equation governing hydraulic potential ϕ, the result of combining 2.13, 2.14, and 2.20:

$$\frac{\partial Q}{\partial s} + \frac{\Xi - \Pi}{L}\left(\frac{1}{\rho_i} - \frac{1}{\rho_w}\right) - v_c - m_c = 0, \tag{2.25}$$

or, more explicitly as an elliptic equation for hydraulic potential,

$$-k_c S^{\alpha_c} \frac{\partial}{\partial s}\left(\left|\frac{\partial \phi}{\partial s}\right|^{\beta_c - 2} \frac{\partial \phi}{\partial s}\right) + \frac{\Xi - \Pi}{L}\left(\frac{1}{\rho_i} - \frac{1}{\rho_w}\right) - v_c - m_c = 0, \tag{2.26}$$

where $Q(S, \frac{\partial\phi}{\partial s})$ is given by 2.20, $\Xi(S, h, \frac{\partial\phi}{\partial s})$ is given by 2.15, $\Pi(S, h, \frac{\partial\phi}{\partial s})$ is given by 2.17, and $v_c(S, N)$ is given by 2.19. The second equation describes the time evolution of S locally through the opening and closing rates:

$$\frac{\partial S}{\partial t} = \frac{\Xi - \Pi}{\rho_i L} - v_c. \tag{2.27}$$

2.1.4 Boundary Conditions

The GlaDS model requires that boundary conditions regarding the hydraulic potential ϕ be applied to the edges of the domain boundary, $\partial\Omega$. The boundary can be split into two portions—$\partial\Omega_D$ to which a Dirichlet boundary condition is applied, and $\partial\Omega_N$ to which a Neumann boundary condition is applied, such that $\partial\Omega_D \cup \partial\Omega_N = \partial\Omega$.

The Dirichlet boundary condition is a static hydraulic potential applied to the grounding line of the glacier. In this application of the GlaDS model, the prescribed hydraulic

potential ϕ_D is the minimum of the overburden potential ϕ_0 across the grounding line $\partial\Omega_D$. That is,

$$\phi_D = \min_{\partial\Omega_D} \left(\rho_i g H + \rho_w g b\right). \tag{2.28}$$

This value of ϕ_D is selected to prevent the transfer of water between nodes on $\partial\Omega_D$, a process that can result in unstable channel growth.

The remainder of the domain boundary, $\partial\Omega_N$, has a Neumann boundary condition which dictates a particular water flux:

$$\frac{\partial\phi}{\partial n} = \Psi_N, \tag{2.29}$$

which corresponds to a specific discharge

$$q_N = -k_s h^{\alpha_s} \left|\nabla\phi\right|^{\beta_s - 2} \Psi_N. \tag{2.30}$$

In this application of the GlaDS model, $\Psi_N = 0$, imposing a zero-flux condition on $\partial\Omega_N$ such that no inflow may occur through this part of the boundary.

2.1.5 Weak Formulation and Numerical Solution

The coupled model equations are solved by recasting them in weak form in order to automatically take care of the coupling terms that govern the exchange of water between the two hydrological systems. First, consider the sheet model; for each subdomain Ω_i, 2.22 is multiplied by a test function θ, and integration by parts is then applied to the product:

$$\int_{\Omega_1} \left[\theta \frac{e_v}{\rho_w g}\frac{\partial\phi}{\partial t} - \nabla\theta\cdot\mathbf{q} + \theta(w_s - v_s - m_b)\right] d\Omega + \int_{\partial\Omega_1} \theta\mathbf{q}\cdot\mathbf{n}|_{\partial\Omega_1}\, d\Gamma = 0, \tag{2.31}$$

The same procedure is applied to 2.26 for each channel segment Γ_j:

$$\int_{\Gamma_j} \left[-\frac{\partial\theta}{\partial s}Q + \theta\left(\frac{\Xi - \Pi}{L}\left(\frac{1}{\rho_i} - \frac{1}{\rho_w}\right) - v_c - m_c\right)\right] d\Gamma + \left[\theta Q_j\right]_-^+ = 0, \tag{2.32}$$

where $[-]_-^+$ indicates evaluation at both ends of segment Γ_j. 2.31 and 2.32 are then summed for each Ω_i and Γ_j to produce an integral over the entirety of Ω:

$$\begin{aligned}
&\sum_{i=1}^{n_\Omega} \int_{\Omega_i} \left[\theta \frac{e_v}{\rho_w g} \frac{\partial \phi}{\partial t} - \nabla\theta \cdot \mathbf{q} + \theta(w_s - v_s - m_b) \right] d\Omega \\
&\quad + \sum_{j=1}^{n_\Gamma} \int_{\Gamma_j} \theta \left[\mathbf{q} \cdot \mathbf{n}|_{\partial\Omega_{i1}} + \mathbf{q} \cdot \mathbf{n}|_{\partial\Omega_{i2}} - m_c \right] d\Gamma \\
&\quad + \int_{\partial\Omega} \theta \mathbf{q} \cdot \mathbf{n} d\Gamma \\
&\quad + \sum_{j=1}^{n_\Gamma} \int_{\Gamma_j} \left[-\frac{\partial\theta}{\partial s} Q + \theta \left(\frac{\Xi - \Pi}{L} \left(\frac{1}{\rho_i} - \frac{1}{\rho_w} \right) - v_c \right) \right] d\Gamma \\
&\quad + \sum_{k=1}^{n_\Lambda} \sum_{j=1}^{n_\Gamma} \theta Q_j^k = 0,
\end{aligned} \tag{2.33}$$

where n_Ω, n_Γ, and n_Λ are the number of subdomains, edges (excluding the boundary, $\partial\Omega$), and nodes respectively.

By substituting the channel source term m_c, as defined in 2.2, into 2.33, it is made apparent that the second summation in the equation is equal to 0:

$$\sum_{j=1}^{n_\Gamma} \int_{\Gamma_j} \theta \left[\mathbf{q} \cdot \mathbf{n}|_{\partial\Omega_{i1}} + \mathbf{q} \cdot \mathbf{n}|_{\partial\Omega_{i2}} - \mathbf{q} \cdot \mathbf{n}|_{\partial\Omega_{i1}} - \mathbf{q} \cdot \mathbf{n}|_{\partial\Omega_{i2}} \right] d\Gamma = 0. \tag{2.34}$$

This term accounts for water exchange between the water sheet and the channel network. The exchange is now implicit; water is exchanged at precisely the rate necessary to sustain equal pressure between the adjacent sheet and the channels. The final summation in 2.33 is also equal to 0, on account of the conservation of water as per 2.1. Finally, θ must satisfy the homogenous boundary condition $\theta = 0$ where Dirichlet boundary conditions are imposed, that is on $\partial\Omega_D$, and discharge q_N as defined by 2.30 is prescribed on the

remainder of the boundary, $\partial\Omega_N$. Hence, the simplified weak form of 2.33 reads

$$\begin{aligned}\sum_{i=1}\int_{\Omega_i}\left[\theta\frac{e_v}{\rho_w g}\frac{\partial\phi}{\partial t}-\nabla\theta\cdot\mathbf{q}+\theta(w_s-v_s-m_b)\right]d\Omega\\ +\sum_j\int_{\Gamma_j}\left[-\frac{\partial\theta}{\partial s}Q+\theta\left(\frac{\Xi-\Pi}{L}\left(\frac{1}{\rho_i}-\frac{1}{\rho_w}\right)-v_c\right)\right]d\Gamma\\ +\int_{\partial\Omega_N}\theta q_N d\Gamma=0.\end{aligned} \tag{2.35}$$

The model is thus described in its entirety by 2.35 and the evolution equations for h and S, 2.24 and 2.27.

A finite element method is used to solve 2.35, which can be regarded as a parabolic equation for ϕ. An irregular triangular mesh is used to partition the domain Ω into triangular elements. The edges of these elements comprise the unstructured channel network Γ. First-order elements, i.e., those containing corner nodes only, are used to discretise ϕ and h, and constant values on each edge are used to discretise S. In the second sum of 2.35, one might expect the integrals over one-dimensional edges to be cancelled, as is customary in partial differential equation problems. However, the contribution from these integrals is essential. Thus, the integration of derivatives along the edges is performed using piecewise linear finite elements. For this application of the GlaDS hydrology model in ISSM, a biconjugate gradient with block Jacobi preconditioner is used to solve the differential equations. Time-stepping is adaptive in this project, with the duration calculated at each step based on a Courant-Friedrich-Lewy (CFL) condition (Courant et al., 1928). This condition ensures stability when calculating a solution by constraining the time step such that the model captures changes in the hydrological system in a way that accurately represents the physical processes involved, thereby avoiding numerical instabilities and unrealistic results.

2.2 Datasets

2.2.1 Mesh and Domain

To create the domain of Trinity-Wykeham Glaciers, the first step is to create a mesh that the hydrological system will occupy. The outline of Trinity-Wykeham Glaciers was initially obtained from the GLIMS Geospatial Glacier Database (Raup et al., 2007). This outline was used as a starting point; the trunks of the two glaciers were traced in QGIS using the

GLIMS outline, and the location of the grounding line was verified using Sentinel-2 L2A imagery from 2019. A ∼500 metre-wide belt connecting the grounding termini of the 2 glaciers was added in order to have one continuous domain. The final product serves as the domain boundary. The WGS 84/NSIDC Sea Ice Polar Stereographic North (ESPG:3413) coordinates that make up the boundary outline are compiled into an ARGUS file. The list of coordinates is then submitted to the ISSM mesh creation algorithm `bamg`, based on the original Bidimensional Anisotropic Mesh Generator (BAMG) software (Hecht, 1998). `bamg` creates a uniform, unstructured, triangular mesh which covers the domain. This mesh contains 19,184 vertices, 36,826 elements, and 56,009 edges with a maximum edge length of 170 m and an area of ~ 505.06 km^2 (see Figure 2.2).

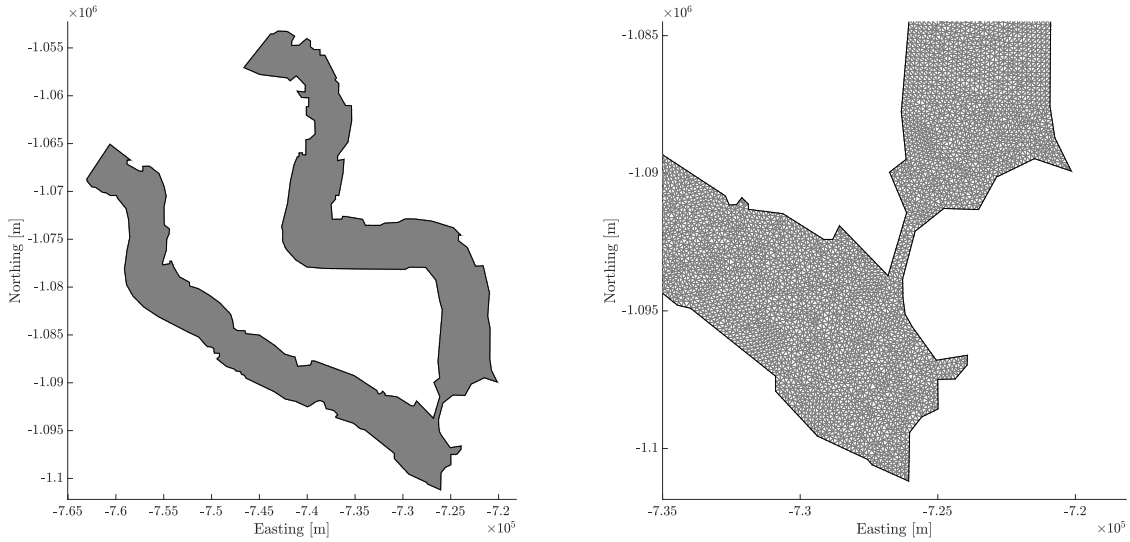

(a) (b)

Figure 2.2: Uniform, unstructured, triangular mesh of Trinity-Wykeham Glaciers. (a) Entire domain; (b) view of the mesh near the grounding line.

Next, the geometry of the glaciers is constructed. The surface elevation of Trinity-Wykeham Glaciers is taken from ArcticDEM Version 3 (Porter et al., 2018). For this project, multiple 2-m-resolution digital elevation models (DEMs), extracted from pairs of high-resolution satellite imagery, are stitched together in QGIS for full coverage of Trinity-Wykeham Glaciers. Bed elevation was provided by Dalton et al. (2022). Their bed topography DEM was created with airborne radar measurements from the Centre for Remote Sensing of Ice Sheet (CReSIS) Multichannel Coherent Data Depth Sounder (MCoRDS)

operating at a frequency range of 180–210 MHz (Paden and Hale., 2013). The DEM has a resolution of 100 m and extends approximately 40 km upglacier from the terminus. MATLAB's `fillmissing` function was used to fill in small gaps in the bed and surface topography data using a moving mean with window length 5. `InterpFromGridToMesh` is an ISSM function that interpolates a grid/array onto a set of points, i.e., the triangular mesh. The surface and bed DEMs are interpolated to the mesh using this function. The bed elevation b is then subtracted from the surface elevation to calculate the thickness H of the glacier ice. A domain-wide minimum ice thickness of 100 m is imposed to avoid numerical errors. The bed and surface topography can be seen in Figure 2.3 below. In Figure (a), areas of overdeepened topography, i.e., where the bed lies below sea level, and highlighted in green. When discussing the model outputs (Section 3), the distinction is often drawn between outputs at low, mid, and high-elevation regions of the glaciers. In Figure (b), the colour map is divided into three distinct portions: 0–350 m a.s.l., 350–575 m a.s.l., and 575–1000 m a.s.l., representing the three regions discussed.

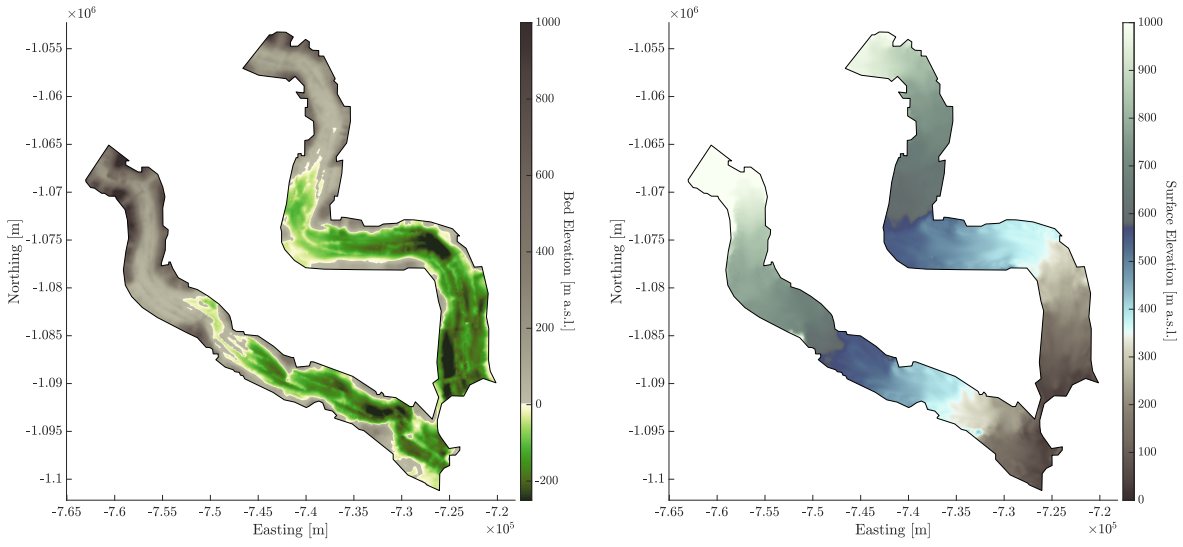

(a) (b)

Figure 2.3: Topography at Trinity-Wykeham Glaciers. (a) Bed topography [m a.s.l] (Dalton et al., 2022). Missing values are linearly interpolated, and subsequently interpolated to the GlaDS mesh; (b) Surface topography [m a.s.l] (Porter et al., 2018). Missing values are linearly interpolated and subsequently interpolated to the GlaDS mesh with a minimum ice thickness of 100 m set.

2.2.2 Velocity and Meltwater Inputs

The glaciers' velocities are initialised using an annual velocity mosaic of the Canadian Arctic in 2017, generated using auto-RIFT (Gardner et al., 2018) and provided by the NASA MEaSUREs ITS_LIVE project (Gardner et al., 2022). The x-component, y-component, and magnitude of basal sliding velocity are estimated as 90% of the corresponding surface velocity values. A single velocity mosaic is used as opposed to a temporally varying velocity because the glacier dynamics and hydrology are not coupled; the velocity serves only to influence the cavity opening rate and calculate the distributed system source term. As such, an average velocity is sufficient. The ITS_LIVE velocity mosaic can be seen in Figure 2.4. Other surface velocity data are used for comparison to model outputs. These data are image pair velocity fields derived from Sentinel-1 synthetic aperture radar (SAR) acquisitions and accessed through the University of Erlangen-Nuremberg (FAU) glacier portal (Friedl et al., 2021). These velocity fields have a temporal resolution of either 6 or 12 days and a spatial resolution of 200 m. Fields from the years 2017 to 2019 are used.

To simulate the glacial hydrology system of Trinity-Wykeham Glaciers, data indicating the volume of water to feed into the system is essential. The data used for this project, provided by Noël et al. (2018), are daily ice surface runoff products for 2016–2019 at 1 km resolution, which they statistically downscaled from the regional climate model RACMO2.3 at 11 km. These data express the daily runoff, i.e., surface melt, for the northern Canadian Arctic in mm w.e. per day, and spans 1958–2019; the dataset is an extension of Noël et al. (2018) which covers 1958–2015, and the melt rate values therein provide a reasonable estimate of the water input to the subglacial hydrological network on a given day. For many glaciers, a substantial percentage of surface meltwater is routed from the surface of the ice to the bed through crevasses and moulins. The GlaDS model is capable of including cylindrical moulins, which connect to individual nodes and transport meltwater directly to the channelised system, and this capability has been used in a number of publications (e.g., Scholzen et al. (2021); Werder et al. (2013)). Due to a lack of moulin mapping for Trinity-Wykeham Glaciers, this approach is not used in this project. The water is fed into the domain by adding the surface melt rate directly to the comparatively low constant basal melt rate of 0.0075 m/yr, a method used in other GlaDS experiments (Cook et al., 2020; Scholzen et al., 2021). This method of water delivery suggests that the water travels immediately from surface to bed without first flowing through the supraglacial and englacial systems. This is likely to result in higher sheet thicknesses, as water that would otherwise be routed directly into a channel is instead produced at the bed in the distributed system. This in turn has the capacity to raise basal water pressures domain-wide.

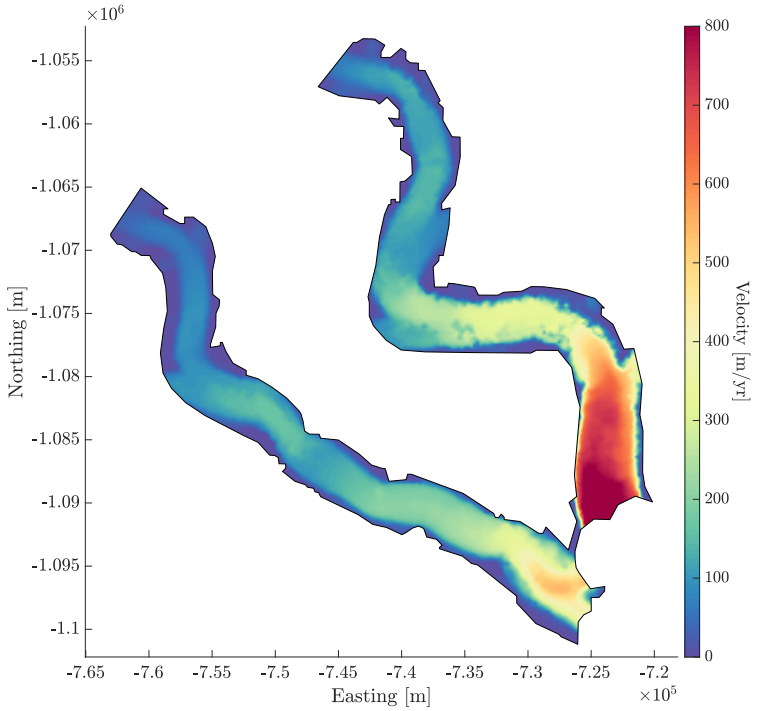

Figure 2.4: Annual velocity mosaic for 2017 used in simulating Trinity-Wykeham Glaciers [m/yr] (Gardner et al., 2022), interpolated to the triangular mesh and prescribed an upper limit of 800 m/yr.

2.3 Model Runs

The goal of the following model runs is to simulate the subglacial hydrological system of Trinity-Wykeham Glaciers, in order to produce outputs of water sheet thickness h, effective pressure N, channel discharge Q, and channel cross-sectional area S. These outputs are compared to image pair velocity fields derived from Sentinel-1 SAR acquisitions (Friedl et al., 2021) to garner an understanding of how subglacial hydrological processes may be affecting the glaciers, namely whether patterns in basal water pressure and channel formation correlate with observed velocity trends. Three types of GlaDS model runs are executed in this study:

1. "steady state" runs;
2. "primer" runs;
3. "meltwater input" runs.

These runs are completed in succession, with outputs from one run used as inputs to the next. When discussing a specific combination of parameters, the term "complete run" or simply "run" is used to refer to the steady state, primer, and meltwater input runs in conjunction.

Sensitivity tests are completed for multiple model parameters. Sheet conductivity k_s and channel conductivity k_c are varied in order to gauge their influence on the development of the subglacial hydrology system. These parameters are very difficult to measure and are thus unknown for Trinity-Wykeham Glaciers, but basal pressure outputs can be interpreted and compared to expected subglacial water pressures to provide reasonable estimates for their real-world values. Other studies using the GlaDS model have cited k_s and k_c as particularly influential on their results (Dow et al., 2018, 2020; Downs et al., 2018; Ehrenfeucht et al., 2023). A total of nine combinations of conductivities are tested (see Table 2.3).

Time-stepping is adaptive for all runs, with the ideal time step between the prescribed minimum (86.4 seconds) and maximum (90 minutes) automatically selected at each step according to the CFL condition; the corresponding CFL constant is set to 3. A number of parameters must be applied to the model as well. For some of these parameters, the default GlaDS/ISSM value is used, whereas others are altered (see Table 2.1 for a full list of default values as well as the used values for this project). An initial water sheet thickness of 0.03 m is employed. The rheological constant B (Larour et al., 2012), representing ice hardness,

Table 2.3: Models and corresponding sheet and channel conductivities used in sensitivity tests.

Model Run	k_c [$m^{3/2}$ $kg^{-1/2}$]	k_s [$m^{7/4}$ $kg^{-1/2}$]
1	10^{-1}	10^{-4}
2	$5 \cdot 10^{-2}$	10^{-4}
3	10^{-2}	10^{-4}
4	10^{-1}	$5 \cdot 10^{-5}$
5	$5 \cdot 10^{-2}$	$5 \cdot 10^{-5}$
6	10^{-2}	$5 \cdot 10^{-5}$
7	10^{-1}	10^{-5}
8	$5 \cdot 10^{-2}$	10^{-5}
9	10^{-2}	10^{-5}

is set to $8.3788 \cdot 10^7$ Pa/$s^{1/n}$ where $n = 3$ to characterise ice at $-2°$ C. The initial hydraulic potential is set to the overburden hydraulic potential $\phi_0 = \phi_m + p_i = \rho_w g B + \rho_i g H$. The Neumann boundary condition is set by prescribing zero flux for all elements of the mesh, and the Dirichlet boundary condition is set by letting the hydraulic potential for all grounding line nodes be equal to the minimum ϕ_0 across all grounding line nodes as per Equation 2.28. Basal velocity is taken to be 90% of the 2017 ITS_LIVE annual velocity mosaic (which reflects surface velocity), with a maximum velocity magnitude of 800 m/yr applied for stability. The velocity mosaic is interpolated to the triangular mesh using `InterpFromGridToMesh`.

The first set of runs discussed are the steady state runs. These runs approximate the realistic state of the subglacial hydrological system prior to the addition of any surface meltwater, as opposed to beginning with an effectively empty system that requires time to fill with water and pressurise. The final outputs of the steady-state runs are used as initial conditions in future runs. Steady-state simulations run for 12,500 days (∼34 years) with the goal of reaching a final, effectively unchanging model state with basal water pressure approaching overburden pressure along the centrelines of the glaciers. The criteria for a successful steady state run is that the water sheet thickness h changes by less than 10^{-6} m between the final two model output times. For steady state runs, the grounded ice melting rate is set to 0.0075 m/yr for a constant, minimal water input to the bed representing basal melt which occurs year-round. Each sensitivity test, which has its own combination of k_c and k_s, requires its own steady state run to keep these values consistent. Nine copies of the model are generated, and channel and sheet conductivities k_c and k_s are applied according to Table 2.3 before running the model.

The next set of model runs are referred to as primer runs. These runs simulate one year of daily meltwater input repeated over 1095 days (3 years) in order to produce a final state that realistically reflects average winter basal conditions in regard to the channelised and distributed systems. The primer run serves to activate subglacial channels and thereby prime the subglacial channel network for the meltwater input runs. Nine primer runs are completed, each with conductivities taken from Table 2.3 and channel area, hydraulic potential, and sheet thickness initialised from the final step of the corresponding steady state run. The RACMO2.3 daily runoff product for 2017 is repeated for three years in the primer runs. This is due to the fact that the volume of meltwater produced at Trinity-Wykeham Glaciers in 2017 best reflects the 2016–2019 mean. Each array representing the meltwater production of a given day is converted to m/yr and interpolated to the mesh. This output is then applied to the model at each vertex, in addition to the background basal melt rate of 0.0075 m/yr, representing the immediate transportation of meltwater from surface to bed. A time vector is created, $\mathbf{t} = \{t \mid t = \frac{j}{365},\ j = 0, 1, ..., 1094\}$. This vector contains the start point of every day of a three-year period expressed in years. Each element of this vector is applied to a specific node such that for each day of the three-year period, the correlated melting rate is applied to that.

The meltwater input runs simulate the subglacial hydrology of Trinity-Wykeham Glaciers over the four-year period of January 1, 2016, to December 31, 2019. Nine meltwater input runs are completed, each with conductivities taken from Table 2.3 and channel area, hydraulic potential, and sheet thickness initialised from the final step of the corresponding primer run. The RACMO2.3 daily runoff product is input to the system using the same procedure as described above, this time using the products from each day between January 1, 2016, to December 31, 2019 and a time vector of length 1461. The sum of all meltwater across the domain for each year can be seen below in Figure 2.5.

2.4 Surface Velocity-Water Pressure Comparisons

As a means of exploring the degree to which basal water pressure may influence the flow of Trinity-Wykeham Glaciers, basal water pressure outputs from GlaDS and SAR-acquired velocity fields, described in Subsection 2.2.2, are compared (Friedl et al., 2021). Available surface velocity data for Trinity-Wykeham Glaciers is limited, and the fields used in this project each have large areas of missing data points. Most data is concentrated in the lower portions of Trinity-Wykeham Glaciers and, as such, the comparisons with the GlaDS outputs are confined to a smaller area of the glaciers, within -733978 to -719950 m East and -1101850 to -1070430 m North. Additionally, substantial noise was captured in the areas

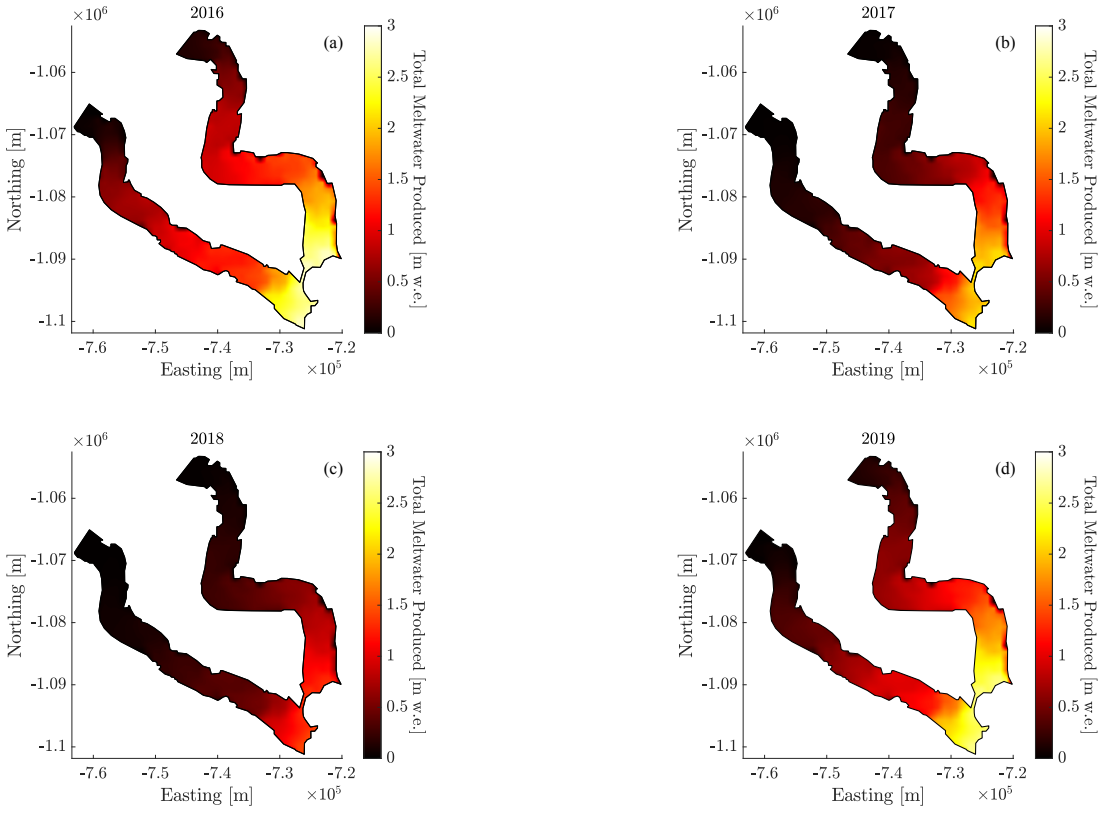

Figure 2.5: Estimate of total surface meltwater produced across Trinity-Wykeham Glaciers for the years 2016-2019 [m w.e.]. (a) 2016; (b) 2017; (c) 2018; (d) 2019. (Noël et al., 2018).

of mountain and ocean outside the domain of the model runs, so MATLAB's `inpolygon` function was used to limit the comparisons to data points within the outline surrounding the domain.

Image pair velocity fields for a given date are compared to a monthly surface velocity mosiac for April of that year, intended to represent the pre-melt season velocity. The image pair velocity fields use the WGS 84/UTM zone 15 N (EPSG:32615) coordinate system (Friedl et al., 2021), while the monthly mosaics use the WGS 84/NSIDC Sea Ice Polar Stereographic North (ESPG:3413) coordinate system. The modelling in this project is performed in the latter coordinate system, and as such the image pair velocity fields are converted to this system. A fractional change method is used to compare basal water pres-

sure and surface velocity changes at Trinity-Wykeham Glaciers. The image pair velocity field for a given date is divided point-wise by a monthly surface velocity mosaic for April of that year. This method shows the percent change in surface velocity during and after the melt season as a fraction of the relatively constant pre-melt season velocity. The same method is used for water pressure outputs, with the date of April 4 of a given year taken for pre-melt season outputs. Three time periods are selected for the outputs:

- early melt season, early to mid-June, approximately 2–4 weeks after water pressure typically increases substantially;
- peak melt season, early to mid-July, shortly before or after mean subglacial water typically pressure peaks;
- post-melt season, late September to early October, once water pressure has typically dropped and surface meltwater input approaches zero.

Table 2.4 compiles the dates taken for the three phases of the melt season in each year between 2017 and 2019. Due to the poor availability of velocity data, no comparisons are made for 2016 outputs.

Table 2.4: Dates chosen for surface velocity and water pressure output comparisons. Pre-melt season velocities are monthly composites.

	2017	2018	2019
Pre-Melt Season Velocity	04/2017	04/2018	04/2019
Pre-Melt Season Pressure	04/04/2017	04/04/2018	04/04/2019
Early Melt Season	03/06/2017	10/06/2018	17/06/2019
Peak Melt Season	21/07/2017	04/07/2018	11/07/2019
Post-Melt Season	01/10/2017	26/10/2018	03/10/2019

Chapter 3

Results

This chapter contains outputs from the GlaDS model simulating subglacial hydrology at Trinity-Wykeham Glaciers. There are nine complete runs (as defined in Section 2.3) in total, each with a unique pairing of sheet conductivity k_s and channel conductivity k_c. All outputs are from these complete runs—that is, taken from the meltwater input runs completed after the corresponding steady state and primer runs. Outputs discussed include subglacial water pressure, subglacial water sheet thickness (as defined in Section 2.1), and channel discharge.

In Section 3.1, a "baseline" run is selected to represent the average behaviour of the subglacial hydrological network of Trinity-Wykeham. Subsection 3.1.1 discusses the model outputs over the course of one year, again selected to represent an average annual cycle for the glaciers, and how they change between seasons based on meltwater input. Subsection 3.1.2 discusses the outputs across the four-year period of 2016–2019 and how the seasonal pattern changes between each year. Baseline run water pressure outputs are compared to SAR-derived surface velocity mosaics in Subsection 3.1.3 to see if patterns emerge between the two variables and how they change both seasonally and interannually.

Section 3.2 reports on the same outputs as in Section 3.1, but compares and contrasts each of the 9 runs with one another to test the sensitivity of the sheet and channel conductivity parameters. Subsections 3.2.1, 3.2.2, and 3.2.3 discuss basal water pressure, water sheet thickness, and channel discharge respectively for all 9 runs.

3.1 Baseline Run

The primary consideration when selecting a baseline run from which main results will be taken is ensuring the outputs reflect the "average" behaviour of the system. One must avoid choosing a run with outputs that diverge from the other runs too drastically. Additionally, the effective pressure is expected to approach 0 (i.e., water pressure is near overburden pressure) along the centreline of the glaciers during winter, and the baseline run must also reflect this. Of the nine runs completed, Run 5 with $k_s = 5 \cdot 10^{-5}$ $\mathrm{m}^{7/4}$ $\mathrm{kg}^{-1/2}$ and $k_c = 5 \cdot 10^{-2}$ $\mathrm{m}^{3/2}$ $\mathrm{kg}^{-1/2}$ was selected as the "baseline" run from which main results will be taken. Run 5 best fulfills the above conditions, and has the added benefit of having the median value for both k_s and k_c.

3.1.1 Seasonal Change

This subsection reports the outputs of the baseline run over the course of one simulated year. The choice of which year to analyse comes down to 2017 and 2018 because it is important for the entire pre- and post-melt season to fall within the simulation period. The year 2017 is used as the example of a typical year, because total meltwater input is nearest the four-year mean of $1.47 \cdot 10^4$ m w.e./yr of melt across the domain annually, and the pre- and post-melt season outputs resemble those of the other years more closely than those of 2018. The season-to-season evolution of the subglacial hydrological network in 2017 is discussed. Meltwater production, mean water pressure, and water sheet thickness at Trinity-Wykeham Glaciers for the duration of 2017 can be seen in Figure 3.1. For each day between January 1, 2016, and December 31, 2019, the daily melt rates provided by Noël et al. (2018) are summed across all vertices in the domain, providing the total amount of meltwater produced on a given date in m w.e./day. Outputs are divided into low, mid, and high-elevation areas of the glaciers (see Figure 2.3 (b)).

3.1.1.1 Meltwater Input

In 2017, the total meltwater input to the subglacial system, $1.19 \cdot 10^4$ m w.e., was nearest the four-year mean of $1.47 \cdot 10^4$ m w.e./yr of melt across the domain annually. From January 1 to May 4, 2017, there was no surface melt at Trinity-Wykeham Glaciers. On May 5, total meltwater jumped to 15.1 m w.e. (see Figure 3.1 (a)). At this point, daily meltwater production was still relatively low, with a mean of 25.4 m w.e. from May 5 to June 16, but on June 17, 132.8 m w.e. of water was produced at Trinity-Wykeham Glaciers, and from then until mid-August this value seldom dropped below 50 m w.e. per day.

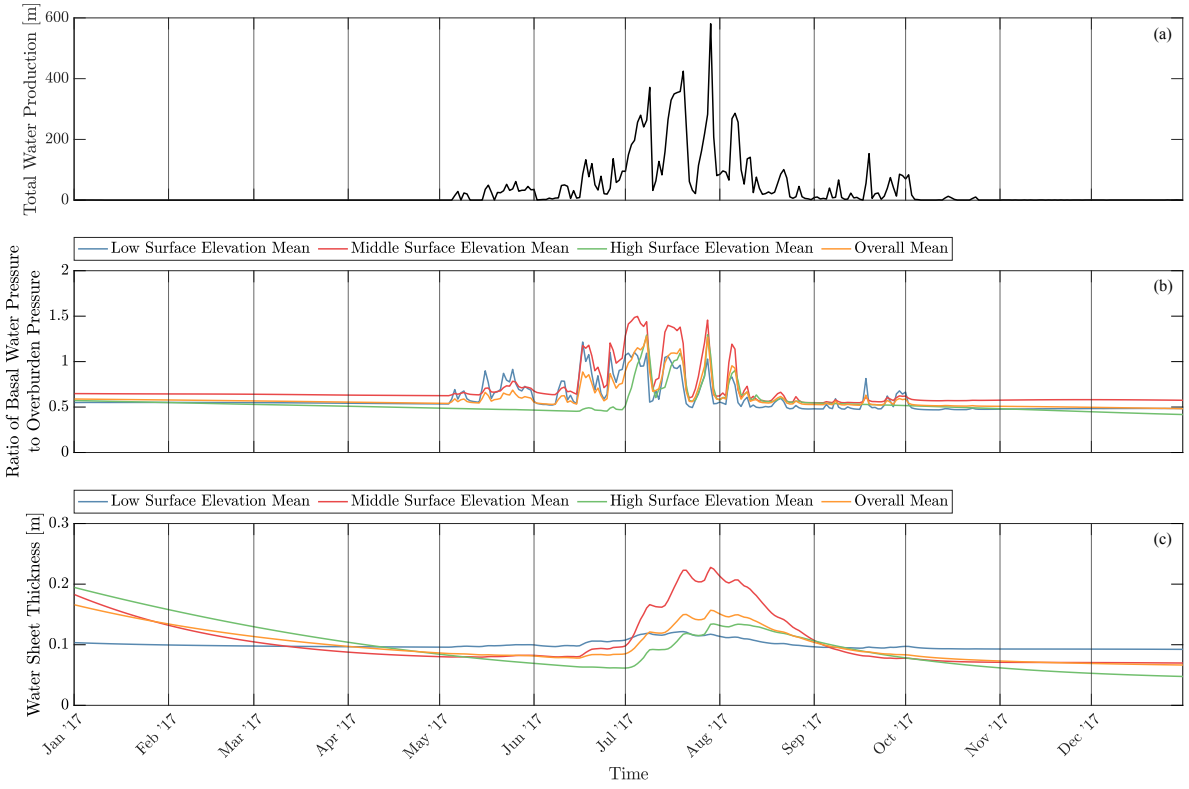

Figure 3.1: Mean model outputs at Trinity-Wykeham Glaciers in 2017 for low surface elevation ($\leq$ 350 m a.s.l), middle surface (between 350 and 575 m a.s.l), and high surface elevation ($\geq$ 575 m a.s.l) regions, and the entire domain. (a) Total meltwater production; (b) mean basal water pressure, expressed as a ratio of basal water pressure to overburden pressure; (c) mean subglacial water sheet thickness.

The peak period of the melt season fell between early July and mid-August. Four distinct peaks in meltwater production occurred, followed by large drops. On July 8, a local maximum of 370.9 m w.e. was produced, with just 31.7 m produced on the following day. The next of these peaks was 424.2 m on July 19, followed by a drop to 60.9 m two days later on July 21. The greatest of these 2017 peaks was on July 28 when meltwater production reached 580.2 m w.e. This was followed by the greatest drop of nearly 500 m w.e. in two days when meltwater production fell to 80.5 m on July 30. August 5 marked the final substantial rise in meltwater production, up to 285.8 m, which then fell to 52.5 m on August 8. The mean meltwater production rate from June 1, 2017, to August 31,

2017, was 109.4 m/day. From this point on, the melt season effectively petered out, and by October 5, daily melt fell below 1 m w.e. per day, aside from two small (< 15 m w.e.) increases in mid-October.

3.1.1.2 Basal Water Pressure

Basal water pressure values are discussed and plotted in terms of the percent of overburden pressure, i.e., the pressure exerted by the overlying ice at a given location. Model outputs of basal water pressure through 2017 are shown in Figure 3.2. The meltwater data describes the melting rate over Trinity-Wykeham Glaciers with a spatial resolution of 1 km^2. These individual melting rates are interpolated to the grid in the form of a melting rate in units of m/yr at each vertex, so the total meltwater production plot (Figure 3.1 (a)) is created by taking the sum of each of these rates on a given date and dividing by 365 to get the total amount of melt produced across the domain on that day. During the first four months of 2017, the mean basal water pressure was relatively constant, with the overall mean water pressure sitting at approximately 56.6% of overburden pressure between January 1 and May 3. This may seem to contradict the above condition that the baseline run must be near overburden prior to the melt season, but in Figure 3.2 it is clear that the centrelines of the glaciers are both pressurised, whereas the margins are at very low pressure. Pressure approached overburden within 1–3 km of the grounding lines but on average, areas of lower surface elevation (≤ 350 m a.s.l) were at lower pressure, 54.6% overburden, in the winter. The middle elevation region (between 350 and 575 m a.s.l) of each glacier was the region of highest pressure prior to the 2017 melt season, with an average of 63.8%. High elevation regions (≥ 575 m a.s.l) had a mean water pressure of 51.4% overburden prior to the melt season pressurisation (January 1 to June 15 at this elevation). In winter, water pressure was generally lowest along the steep valley walls and higher in the deeper parts of the bedrock, relative to the overburden pressure exerted by the overlying ice. The opposite was true during the summer months when input from the surface was significant. It should be noted that the ice is generally thinnest along the valley walls and, as such, applies less pressure to the bed below compared to areas of deep bedrock/thick ice. As a result, when plotting basal water pressure as a fraction of overburden pressure, a comparatively small change in pressure is required to raise the fraction of overburden by a given amount in these marginal areas compared to areas in which ice is thicker.

At the beginning of the melt season, the water pressure at the base of Trinity-Wykeham Glaciers began to rise. The increase in pressure first occurred at low elevation, and as the melt season progressed the increased pressure progressed upglacier. The areas of low and middle surface elevation first began to pressurise on May 4. Initially, the increase was both

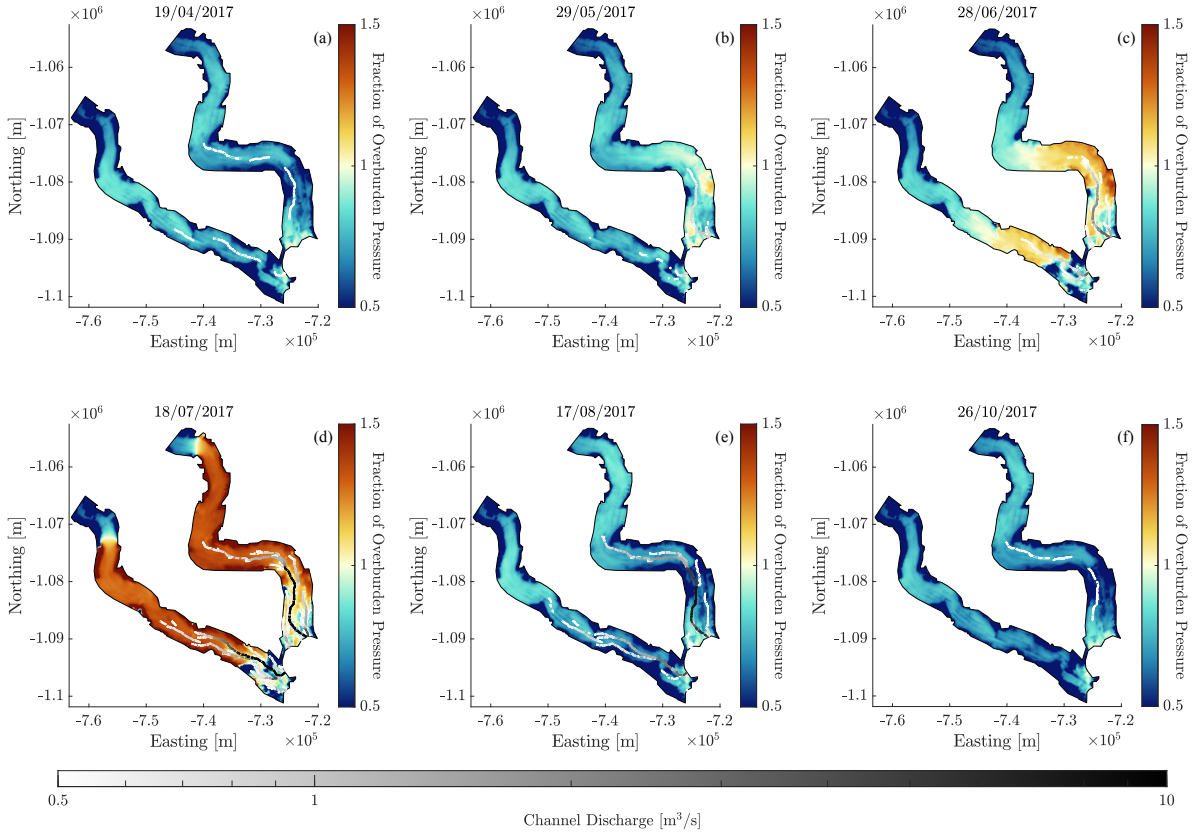

Figure 3.2: Ratio of basal water pressure to overburden pressure for Trinity-Wykeham Glaciers on various dates in 2017. Channel discharge is overlaid in grey. (a) 19/04/2017; (b) 29/05/2017; (c) 28/06/2017; (d) 18/07/2017; (e) 17/08/2017; (f) 26/10/2017.

greater and more rapid at lower elevations, reaching a local maximum of 91.5% by May 24, an increase of 38.1% overburden in 20 days. In contrast, the mid-elevation region rose from 54.0% to 68.6% in the same time frame. The upper reaches of Trinity-Wykeham Glaciers did not begin to pressurise until June 16, with the first significant increase beginning on June 30. From this date, water pressure at high elevations increased from 51.3% to 129.2% overburden in just one week.

Extreme fluctuations in basal water pressure occurred throughout the melt season, as seen in Figure 3.1 (b). There were 6 distinct periods in which overall mean water pressure increased by a minimum of 30% overburden in 2–5 days, frequently decreasing to near-

winter values 2–5 days thereafter. Each of these periods occurred between June 14 and August 7. The greatest of these spikes occurred between July 22 and 27 when overall mean basal water pressure increased from 55.9% to 126.9% overburden, a 71.0% increase, and then decreased by 63.1% overburden in the following two days. In the early melt season before the higher elevation regions are pressurised (May 4 to June 15), the mean water pressures at lower and mid elevations were 11.4% and 4.4% overburden above winter means respectively. Later in the melt season (June 16 to July 28), the low, mid, and high elevation means were 84.7%, 110.0%, and 72.8% overburden, increases of 30.1%, 46.2%, and 21.4% overburden above the respective winter means. The overall mean for the late melt season was 87.0% overburden, up 30.4% from the winter mean of 56.6%. Water pressure peaks were sequential between elevation levels; the peaks were 121.6% overburden on June 16 at low elevation, 149.7% on July 4 at mid-elevation, and 129.5% on July 27 at high elevation. One should note that there were multiple instances of high-elevation water pressures reaching a local maximum one day after a local maximum in the lower and middle regions, demonstrating a "lag" in the pressures increases as they migrated upglacier. The upper reaches underwent only 4 distinct spikes in pressure. July 7 was the date on which the mean pressure across the domain attained its maximum value of 128.1% overburden.

On August 2, mean water pressure suddenly dropped by approximately 36.8% then began to decline gradually. By the end of 2017, water pressure was approximately 8.8% lower than the pre-melt season mean across all sections of both glaciers. Basal water pressure was consistently lowest near the grounding line of Trinity-Wykeham Glaciers. Numerous small channels formed during the melt season, branching upglacier from the grounding line, and the low-pressure areas of the bed largely coincided with channel location and rates of discharge. In general, both glaciers followed similar geographical patterns of pressurisation in that "waves" of high pressures swept from lower elevation to higher elevation. However, in mid-May, the portion of Trinity Glacier that is south of $-1.075 \cdot 10^6$ m North becomes highly pressurised before any significant changes are seen at Wykeham Glacier.

3.1.1.3 Water Sheet Thickness

Modelled subglacial water sheet thickness is representative of the distributed hydrological network beneath Trinity-Wykeham Glaciers. Model outputs of sheet thickness through 2017 are shown in Figure 3.3. On January 1, 2017, mean sheet thickness sat above the average bump height of 0.100 m in all areas of the glaciers. The low, mid, and high elevation regions had mean sheet thicknesses of 0.104 m, 0.185 m, and 0.196 m respectively, with the overall mean at 0.167 m. At the beginning of 2017, sheet thickness in the mid and

high-altitude regions of Trinity-Wykeham Glaciers was still elevated as water continued to drain from the previous melt season, whereas sheet thickness at low elevations was relatively uniform. From January 1 to June 15, the low, mid, and high altitudes had sheet thickness means of 0.098 m, 0.105 m, and 0.117 m respectively, with an overall mean of 0.108 m. The mean water sheet underwent substantial change at high and mid-elevation between these two dates, decreasing by 0.133 m and 0.105 m respectively. There were multiple small reservoirs at the base of Trinity-Wykeham Glaciers that held substantially more water than the mean during winter months. The largest such reservoir was found in an overdeepening between $-7.495 \cdot 10^5$ m and $-7.520 \cdot 10^5$ m East along the northern margin of Wykeham Glacier. The reservoir was approximately 2.5 km long and 1.5 km wide and contained water 0.2–0.9 m deep. Other, smaller reservoirs were found in the high-altitude area of both glaciers and near the grounding line of Trinity Glacier (see Figure 3.3 (a)).

On June 15, sheet thickness began to increase by 1–3 mm a day in the mid-altitude region of the glaciers (see Figure 3.1 (c)). On July 2, the sheet thickness began to increase at a similar rate in the higher elevation regions of the glaciers, and the rate of increase escalated dramatically to 7–12 mm a day at intermediate elevation. Peak water sheet thickness was reached on July 28 at mid and high-elevation, at which point the glaciers had mean subglacial water sheet thickness of 0.228 m and 0.157 m in those respective regions. The mean sheet thickness at low elevation underwent very little change, with only 0.030 m between the minimum (0.092 m on December 31) and maximum (0.122 m on July 19) thickness during 2017. The mid and high-elevation regions had ranges of 0.158 m and 0.149 m respectively.

There are a number of distinctions to be drawn between the progression of the basal water pressure and the water sheet thickness. Whereas the water pressure heavily fluctuated through the melt season, the rise and fall of the mean sheet thickness was much more regular. While not purely monotonic, the trends in sheet thickness effectively traced a parabola, with insignificant oscillations throughout the melt season. There was no rapid decrease in sheet thickness; water drainage post-melt season was very gradual and followed an approximately exponential curve to winter levels. For both water pressure and water sheet thickness, the bed at mid-altitude changed most rapidly and exhibited both the deepest subglacial water and the greatest water pressure.

3.1.1.4 Channel Discharge

Figures 3.2 and 3.3 show the location and discharge of subglacial channels through 2017. In these figures, to be classified as a "channel," edges are required to exhibit a minimum of 0.5 m^3/s discharge. Figure 3.4 contains three subplots; subplot (a) depicts the total

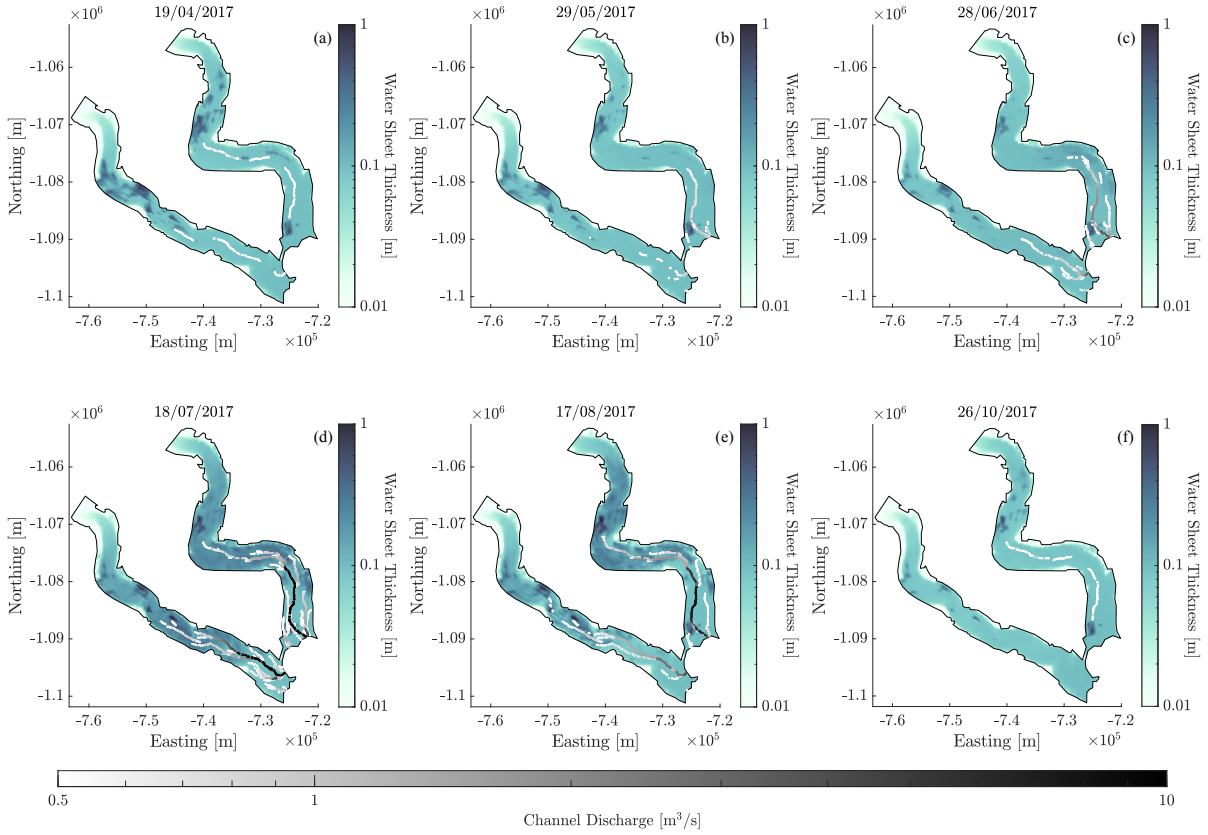

Figure 3.3: Subglacial water sheet thickness for Trinity-Wykeham Glaciers on various dates in 2017. Channel discharge is overlaid in grey. (a) 19/04/2017; (b) 29/05/2017; (c) 28/06/2017; (d) 18/07/2017; (e) 17/08/2017; (f) 26/10/2017.

meltwater produced at Trinity-Wykeham Glaciers on each day of 2017, interpreted from data from Noël et al. (2018), subplot (b) depicts the total channel discharge through all edges with at least one node on the grounding line, and subplot (c) depicts the maximum discharge through any one of these edges. The latter two subplots have separate curves for the grounding lines of Trinity and Wykeham Glaciers respectively.

In the months before the 2017 melt season began, there was minimal discharge through channels that remained from the 2016 melt season, and the rate of discharge from these channels gradually decreased. Between January 1 and April 3, the mean total discharge through the grounding lines was 2.63 m^3/s and 1.56 m^3/s for Trinity and Wykeham Glaciers

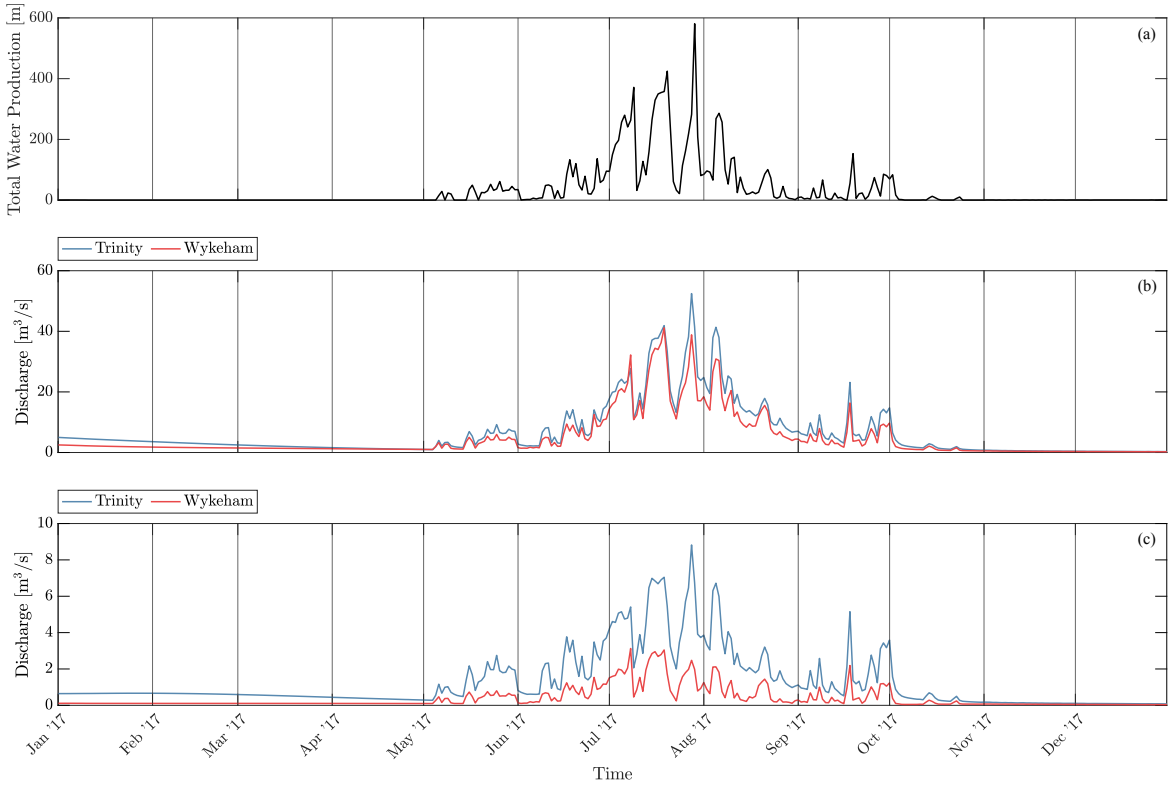

Figure 3.4: Maximum discharge through the grounding lines of Trinity-Wykeham Glaciers in 2017. (a) Total meltwater production; (b) total discharge through grounding line nodes; (c) maximum discharge through any one grounding line node.

respectively. During this period, the maximal discharge through any grounding line channel at Wykeham Glacier was below the 0.5 m^3/s threshold, and by March 20, the same is true of Trinity Glacier. By May 4, channels at Trinity Glacier began to carry water above this threshold as meltwater was added to the bed, and the same threshold was broken ten days later at Wykeham Glacier. From this point onward, channel discharge trended upward at both glaciers, with fluctuations in discharge rate coinciding with elevated levels of surface melt. The curves for both glaciers mirrored one another closely, i.e., they increased and decreased at the same intervals, differing only in magnitude. By June 28, both glaciers had a number of small (2–7 km long), relatively low-discharge ($\sim< 1 m^3/s$) channels extending from the grounding line, and one main channel with high discharge extending upglacier. The main channel at Trinity Glacier passed through the overdeepening between $-1.085 \cdot 10^6$

m and $-1.088 \cdot 10^6$ m North and reached $\sim$ 16 km upglacier, and the main channel at Wykeham Glacier extended about 14 km upglacier. Trinity reached its maximum single-channel discharge on July 27 at 8.82 m^3/s, whereas Wykeham Glacier reached its maximum of 3.13 m^3/s 20 days prior on July 7. This was the only date on which total grounding line discharge at Wykeham Glacier exceeded that of Trinity Glacier when Wykeham Glacier's discharge reached 32.2 m^3/s while Trinity Glacier's discharge was at 27.7 m^3/s. Otherwise, Trinity Glacier's maximum single-channel discharge was always 2–9 times greater than that of Wykeham Glacier. In general, sheet thickness was reduced in the vicinity of channels, especially the main channels with high rates of discharge. For instance, at -1079750 m North on Trinity Glacier, $\sim$ 10 km upglacier, the mean sheet thickness on July 27 is $\sim$ 39% lower within 700 m of the main channel (with a discharge rate of 16.8 m^3/s in that area) than across the entire width of the glacier.

From July 27, total meltwater production underwent a substantial drop from the 2017 peak of 580.6 m to 80.9 m in just two days. Discharge from Trinity Glacier dropped from 52.4 m^3/s to 25.0 m^3/s in this period, while the discharge through Wykeham Glacier fell from 38.8 m^3/s to 17.1 m^3/s. From this point until the end of 2017, channel discharge trended downward for both glaciers, decreasing at a slower, relatively uniform rate with infrequent minor increases coincident with elevated melt rates in the fall months. By October 15, no channel at the grounding line discharged above the threshold of 0.5 m^3/s. The main channels along the centreline of both glaciers persisted past this date, and by November 8, all channels ceased to discharge above the threshold.

3.1.2 Interannual Change

Each model run is designed to simulate the period between January 1, 2016 and December 31, 2019. While each year followed a similar pattern in terms of seasonal changes in subglacial water pressure, water volume, and channel formation, there are distinct differences in how the meltwater input affects these variables. Figure 3.5 depicts meltwater production, mean water pressure, and sheet thickness at low elevation, mid-elevation, high elevation, and across the entire domain, for the duration of Run 5.

A mean $1.47 \cdot 10^4$ m w.e./yr of meltwater was produced at Trinity-Wykeham Glaciers annually across the four-year period of the simulation. The year of greatest melt was 2016 at $2.18 \cdot 10^4$ m w.e., a 47.8% increase from the mean. The year of least melt was 2018 at $7.54 \cdot 10^3$ m w.e. which is only 51.2% of the mean. The 2017 and 2019 totals ($1.18 \cdot 10^4$ m w.e. and $1.79 \cdot 10^4$ m w.e.) are comparable, at $\sim$ 20% below and $\sim$ 20% above the four-year mean respectively. Figure 3.6 spatially depicts the mean melting rate at Trinity-Wykeham

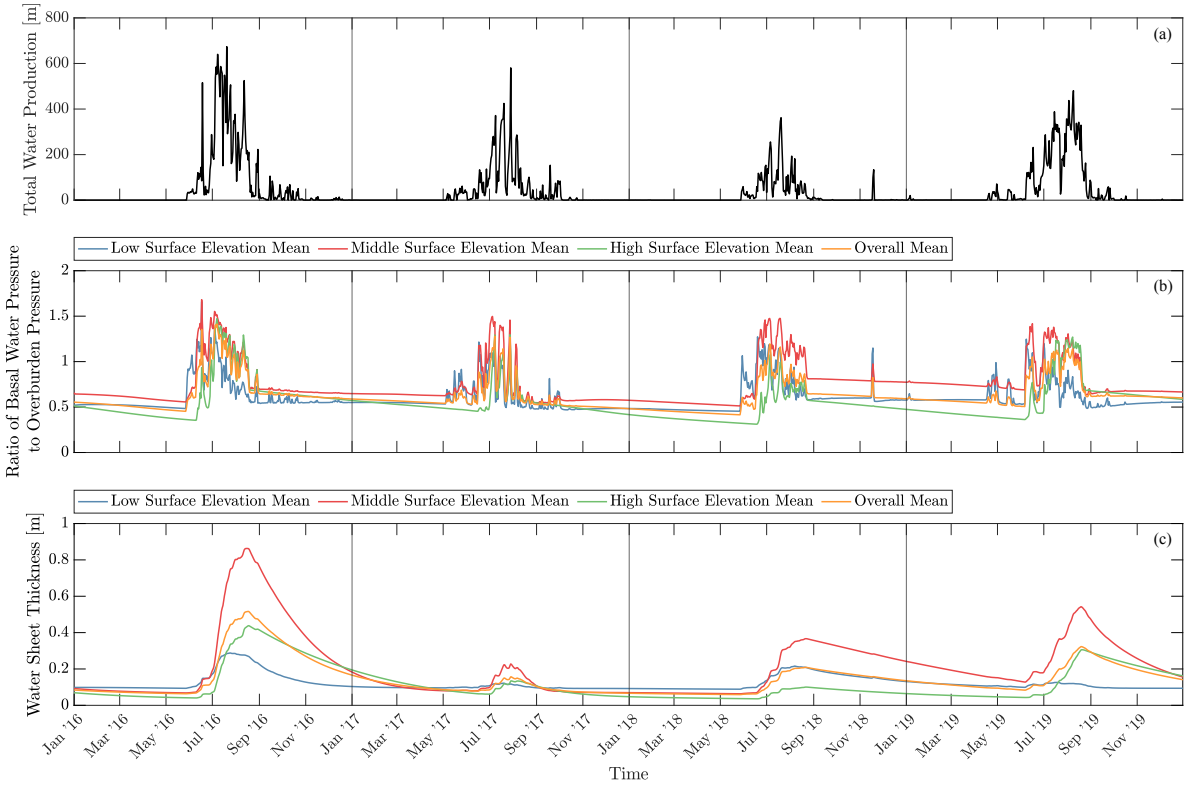

Figure 3.5: Mean model outputs at Trinity-Wykeham Glaciers for 2016–2019 for low surface elevation ($\leq$ 350 m a.s.l), middle surface (between 350 and 575 m a.s.l), and high surface elevation ($\geq$ 575 m a.s.l) regions, and the entire domain. (a) Total meltwater production; (b) mean basal water pressure, expressed as a ratio of basal water pressure to overburden pressure; (c) mean subglacial water sheet thickness.

Glaciers, including background basal melt of 0.0075 m/yr, from June 1 to August 31 of each year.

The first day of the 2016 melt season was May 28, on which 27.9 m w.e. was produced. This value stayed below 50 m w.e. until it reached 83.6 m w.e. on June 10 and then rapidly climbed to 515.2 m w.e. one week later on June 17, and dropped to 23.3 m w.e. two days further on June 19. Meltwater production did not reach these heights again until July 4 when 535.9 m w.e. was produced. Rates of melt fluctuated heavily after July 4, rising and falling by up to $\sim$ 400 m/day from one day to the next. July 19, 2016, was the day on

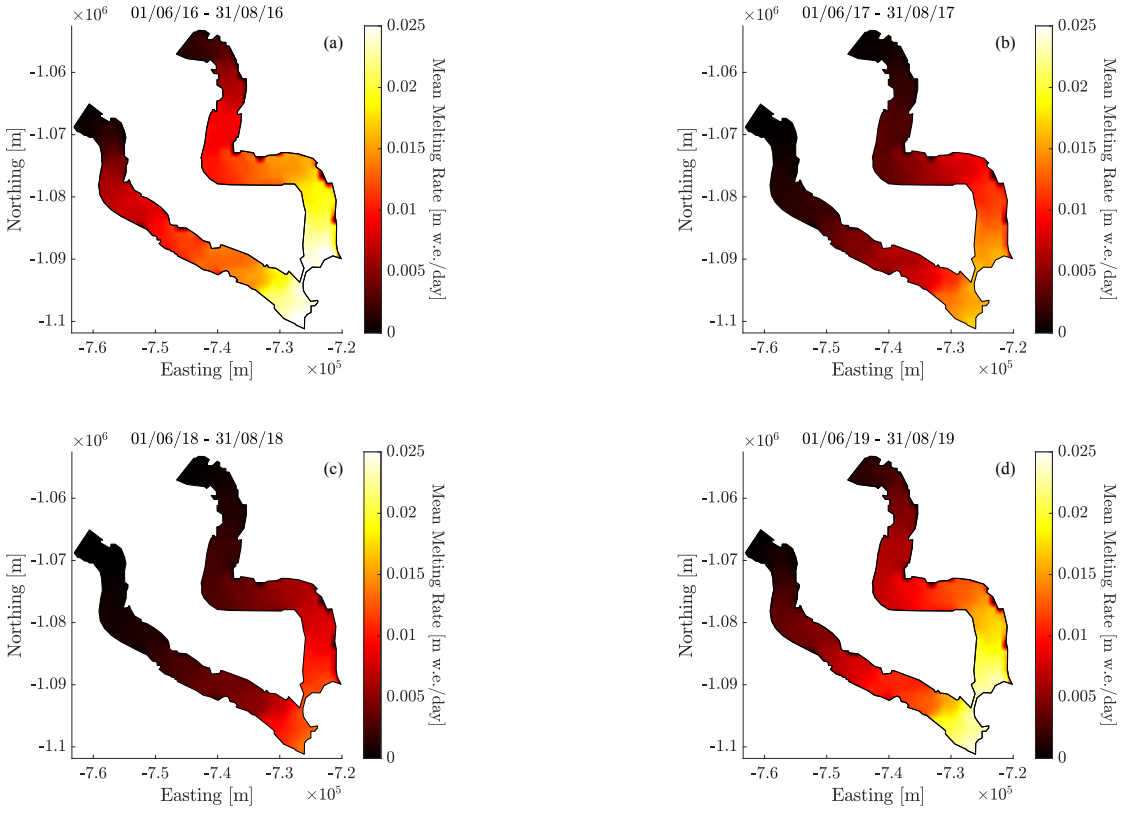

Figure 3.6: Mean melting rates at Trinity-Wykeham Glaciers between 01/06 and 31/08 for the years 2016–2019 [m w.e./day]. (a) 2016; (b) 2017; (c) 2018; (d) 2019.

which a maximal 673.4 m w.e. of water was produced at Trinity-Wykeham Glaciers, the greatest amount across the four-year period. Between June 1 and August 31, an average of 222.9 m w.e. was produced daily. By the end of August and through the end of the year, meltwater production rates were typically below 10 m w.e./day, aside from short bursts of high melt in mid-September and mid-October.

A detailed description of meltwater production in 2017 is given at the beginning of Subsection 3.1.1. As in 2016, the first day of the 2018 melt season was May 28. On this date, a total of 37.4 m w.e. was produced at Trinity-Wykeham Glaciers. June 19 was the first day of 2018 which saw over 100 m w.e. produced, with a total of 117.6 m w.e. The melt season average rate in 2018 was just 76.3 m w.e./day, taken between June 1 and

August 31. The annual maximum rate of 361.4 m w.e./day occurred on the same date as the 2016 maximum on July 19. By September 1, meltwater production rates fell below 10 m w.e./day for the remainder of the year. There was a spike from November 17–18 where water production rates reached 99.3 and 133.1 m w.e./day respectively, a significant volume in a year with such little melt.

The 2019 melt season began differently than in other years. Meltwater production first exceeded 1 m w.e./day on April 16 but remained below 50 m w.e./day until June 6, aside from a spike to 70.9 m w.e. on April 29. The mean meltwater production rate at Trinity-Wykeham Glaciers between April 16 and June 6 was 14.4 m w.e./day. After this, the main portion of the melt season began. Total melt rate spiked to 87.6 m w.e. on June 7, then climbed further to 231.0 m w.e. nine days later on June 16. After a brief period of sub-100 m w.e. days, another spike to 286.4 m w.e./day occurs on July 2. Water production rates stayed in the 140–400 m w.e./day range through the majority of the melt season, but reached maximal rates of 436.8, 425.4, and 480.2 m w.e./day on August 2, 7, and 8 respectively. After this, meltwater production rates trended downward while still fluctuating. The mean total melt rate between June 1 and August 31, 2019, was 180.8 m w.e./day, and from September 1 to the end of the year, the mean was 4.01 m w.e./day.

Figures 3.7 and 3.8 depict the water pressure (as a fraction of overburden pressure) and water sheet thickness outputs for 2016, and likewise for Figures 3.2 and 3.3 in 2017 and Figures 3.9 and 3.10 in 2018.

At the beginning of 2016, basal water pressure and sheet thickness were both slightly below the outputs of 2017. Mean pressure across the entire glacier was 50.6% overburden prior to the melt season increase, and mean sheet thickness was 0.071 m, a deficit of 6% overburden and 0.037 m respectively when compared to the following year. Lower still were the 2018 means of 44.7% overburden and 0.062 m of water at the base. However, basal conditions prior to the 2019 melt season onset were nearly identical to those in 2017 in terms of the overall means. In 2017 and 2019, mean winter water pressure sat at 56.6% and 56.3% respectively overall, though the pressure varied spatially between the two years. Prior to the 2017 melt season, areas of lower surface elevation were at 54.6% overburden, areas of intermediate elevation were at 63.8% overburden, and areas of high elevation were at 51.5% overburden in the winter, a range of 12.3% across the domain. In 2019, mean water pressure was at 51.8%, 75.3%, and 43.4% overburden at low, mid, and high elevations respectively in the winter, showing a 31.9% difference between the mid and high-elevation areas during that period. Pre-melt season sheet thickness means were also very near in 2017 and 2019, at 0.108 m and 0.107 m respectively, but once again the spatial distribution of water varied substantially. In 2017, the region of Trinity-Wykeham Glaciers at the highest altitude held the most water, with a mean of 0.117 m, but in 2019 the opposite is true, and

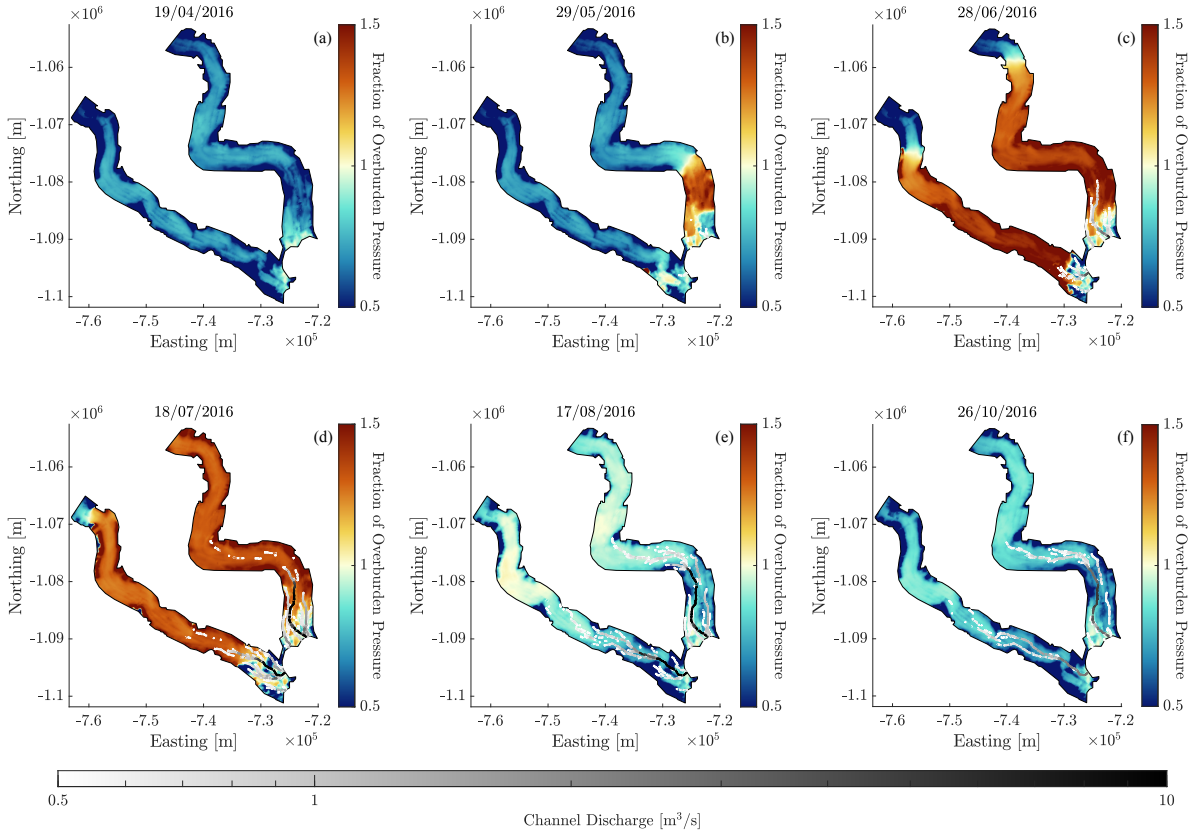

Figure 3.7: Ratio of basal water pressure to overburden pressure for Trinity-Wykeham Glaciers on various dates in 2016. Channel discharge is overlaid in grey. (a) 19/04/2016; (b) 29/05/2016; (c) 28/06/2016; (d) 18/07/2016; (e) 17/08/2016; (f) 26/10/2016.

the high-elevation region had the lowest mean sheet thickness of the entire domain at just 0.053 m. In 2017 and 2019, channels persisted from the melt season prior, though these channels were few and carried low volumes of water compared to melt season rates(< 4.5 m^3/s in 2017, < 1.5 m^3/s in 2019). In addition to the overdeepening near its grounding line which persists throughout the simulation, there was another large water reservoir present on Trinity Glacier in 2019 between $-7.25 \cdot 10^5$ m and $-7.31 \cdot 10^5$ m East (see Figure 3.12 (a)) which had a maximum depth maximum winter depth of ~ 0.9 m.

Each year exhibited a similar pattern in hydrology at the start of the melt season, although the timing of changes to the system varied. In all four years, a sharp increase in

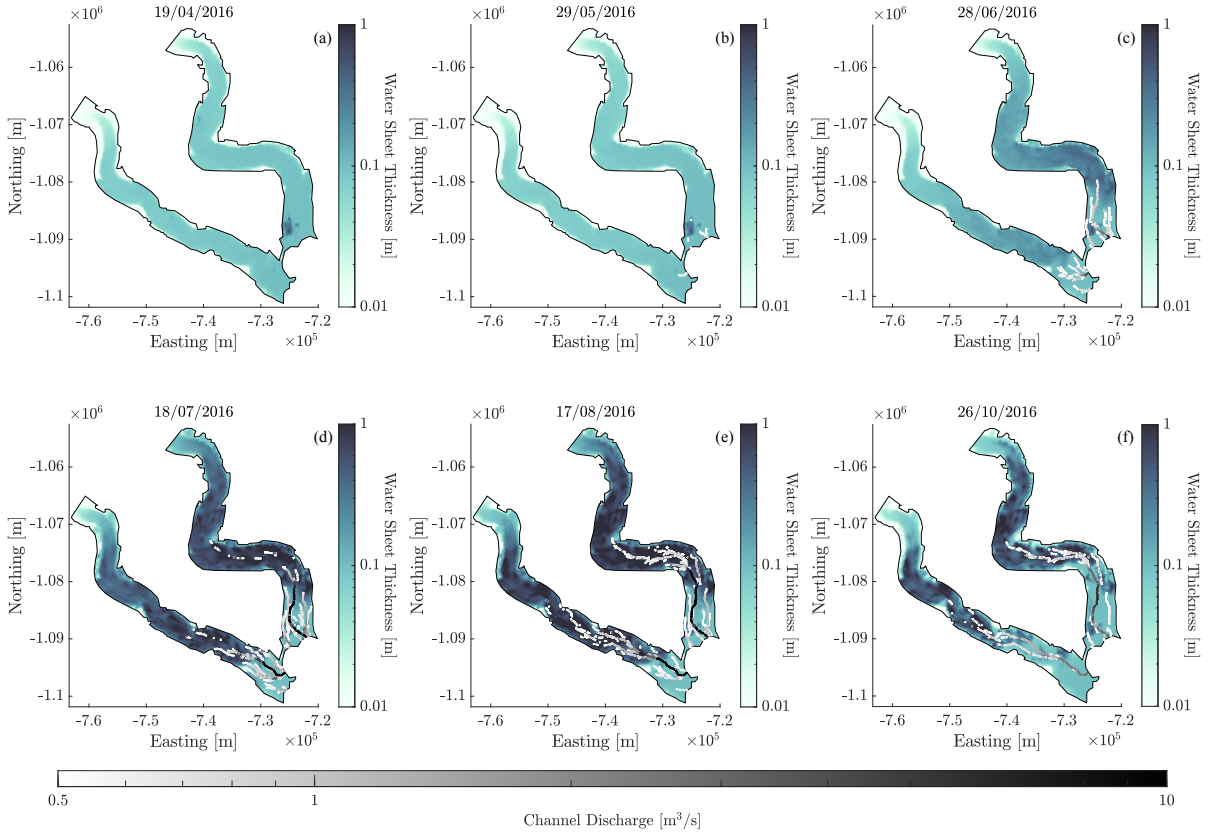

Figure 3.8: Subglacial water sheet thickness for Trinity-Wykeham Glaciers on various dates in 2016. Channel discharge is overlaid in grey. (a) 19/04/2016; (b) 29/05/2016; (c) 28/06/2016; (d) 18/07/2016; (e) 17/08/2016; (f) 26/10/2016.

basal water pressure occurred, followed by large fluctuations in pressure. The initial spike in water pressure occurred at approximately the same time each year, save for 2017, and was effectively synchronous with elevated melt rates. May 27, 2016, May 27, 2018, and June 6, 2019, all mark dates on which water pressure built in the subglacial hydrological system of Trinity-Wykeham Glaciers, but the spike in 2017 occurred 23–33 days earlier in the year on May 4. Two small, brief spikes in pressure occurred before the main pressure increase in 2019 from April 17–May 1 (with a maximum 11.5% above the winter mean) and May 12–May 20 (with a maximum 5.0% above the winter mean). A lag is observed in all years between the initial increase in basal water pressure and the rise in basal water

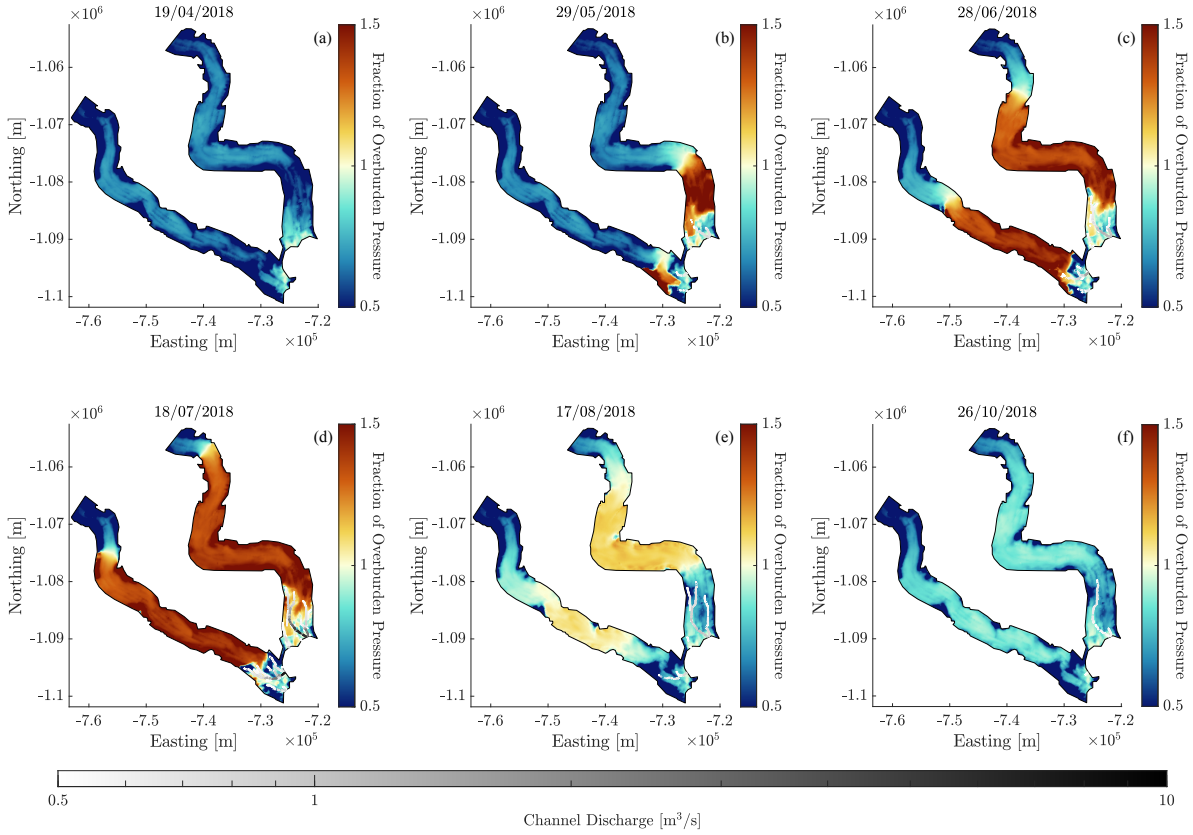

Figure 3.9: Ratio of basal water pressure to overburden pressure for Trinity-Wykeham Glaciers on various dates in 2018. Channel discharge is overlaid in grey. (a) 19/04/2018; (b) 29/05/2018; (c) 28/06/2018; (d) 18/07/2018; (e) 17/08/2018; (f) 26/10/2018.

sheet thickness. In 2016, mean sheet thickness began to climb on June 10, two weeks after the increase in mean pressure. Both the sharpest and greatest increase in sheet thickness occurred in 2016, jumping 0.020 m from 0.213 m to 0.233 m between July 6 and July 7 and reaching its maximal mean thickness of 0.516 m on August 16. The following three years saw meltwater production increase less rapidly, and the increase in sheet thickness followed suit. Sheet thickness began to increase by 1–3 mm a day on June 16, 2017, and June 19, 2018, ~ 6 and ~ 3 weeks after the pressure fluctuations began in each respective year. The maximum single-day increase for 2017 occurred between July 26 and 27 at 0.007 m, and in 2018 on July 18, up 0.011 m from the previous day. 2019 is an outlier here in

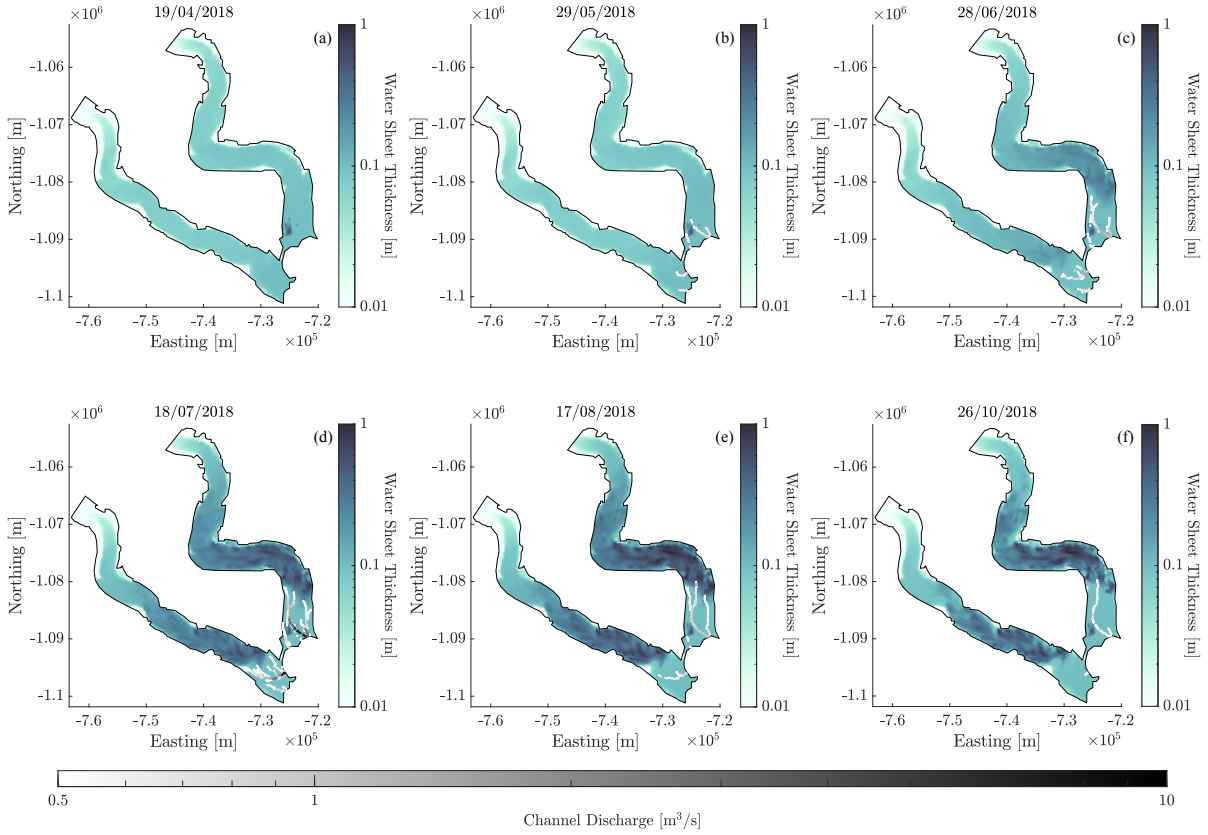

Figure 3.10: Subglacial water sheet thickness for Trinity-Wykeham Glaciers on various dates in 2018. Channel discharge is overlaid in grey. (a) 19/04/2018; (b) 29/05/2018; (c) 28/06/2018; (d) 18/07/2018; (e) 17/08/2018; (f) 26/10/2018.

that mean basal water pressure began to increase on June 6, the same day as the sharp increase in basal water pressure. The maximum one-day increase in mean sheet thickness in 2019 was 0.009 m, which occurred between August 6 and 7.

Melt season basal water pressure and sheet thickness attained their highest values across both glaciers in 2016 (see Figures 3.5 (b) and (c)). Mean melt season water pressure (taken in all years from the date on which pressure began to increase as listed above to September 1 of that year) in 2016 was 91.6% of overburden pressure. Meanwhile, the mean sheet thickness during the 2016 melt season (taken in all years from the date on which sheet thickness began to increase as listed above to September 1 of that year) was 0.338 m,

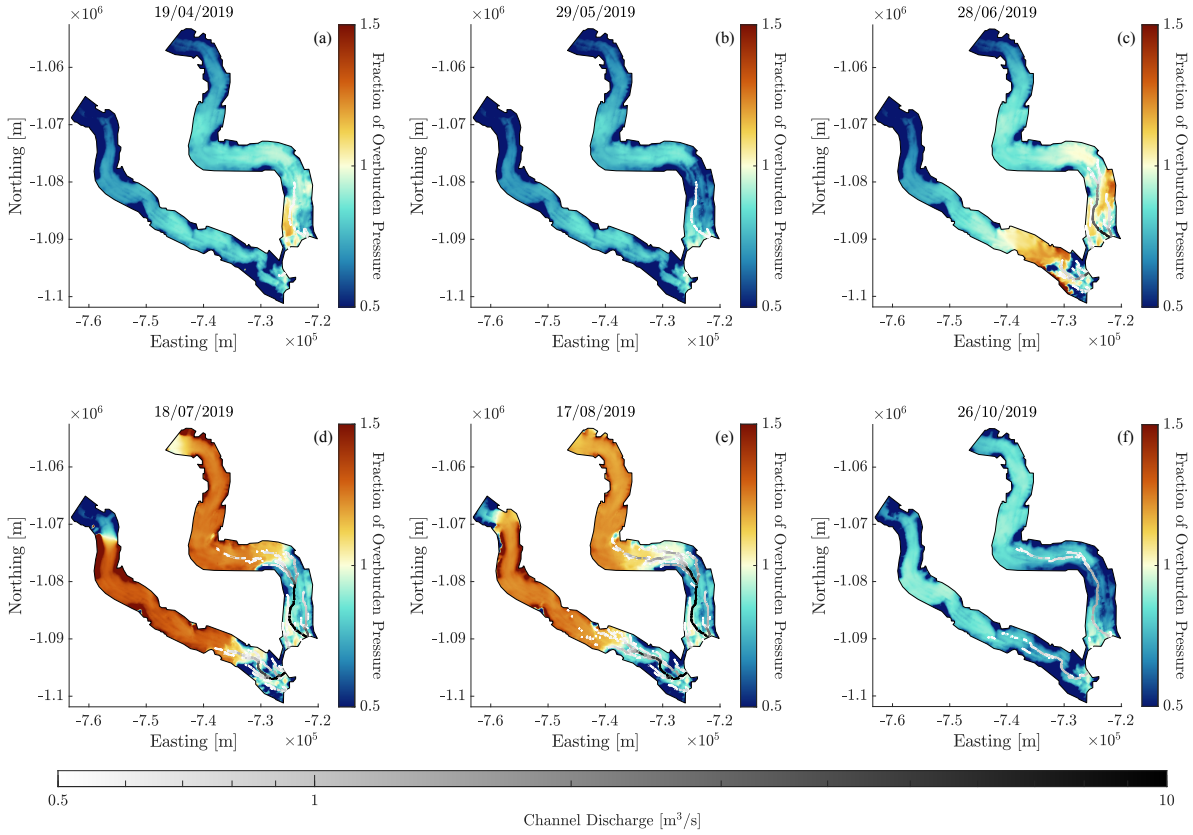

Figure 3.11: Ratio of basal water pressure to overburden pressure for Trinity-Wykeham Glaciers on various dates in 2019. Channel discharge is overlaid in grey. (a) 19/04/2019; (b) 29/05/2019; (c) 28/06/2019; (d) 18/07/2019; (e) 17/08/2019; (f) 26/10/2019.

nearly five times the winter mean. The subglacial hydrological system underwent the least change during the 2017 melt season, with mean water pressure at just 69.1% overburden and a mean sheet thickness of 0.107 m, which is actually 1 mm less than the 2017 winter mean (likely attributable to water remaining from the strong 2016 melt season). The years 2018 and 2019 both fell between these two extremes with mean melt season water pressure of 78.0% and 87.8% overburden respectively, and respective mean sheet thicknesses of 0.164 m and 0.197 m. Every year, virtually the entire length of the trunks became highly pressurised. Lower pressures were found at low elevations within ~ 5 km of the grounding line and in the highest reaches of the trunks. Waves of high pressure originated nearer the

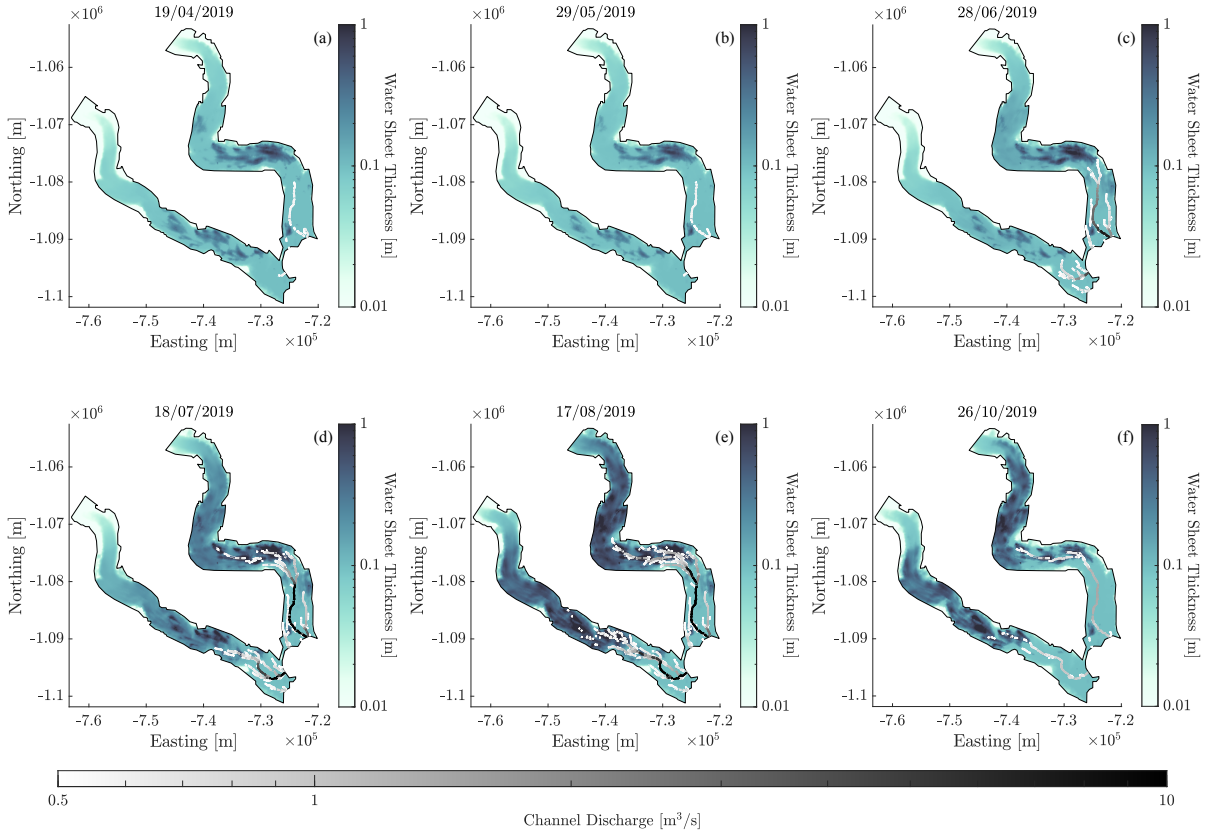

Figure 3.12: Subglacial water sheet thickness for Trinity-Wykeham Glaciers on various dates in 2019. Channel discharge is overlaid in grey. (a) 19/04/2019; (b) 29/05/2019; (c) 28/06/2019; (d) 18/07/2019; (e) 17/08/2019; (f) 26/10/2019.

grounding line and worked their way upglacier, and the pressure decreased in much the same way.

Figure 3.5 (b) shows that in the first three years of the simulation, peak water pressure occurred at roughly the same time of year; these maxima were 141.4% overburden on July 6, 2016, 128.1% overburden on July 7, 2017, and 119.4% overburden on July 4, 2018. The greatest mean basal water pressure of 2019, 114.7% overburden, was reached nearly one month later in the year on August 1. Basal water pressure also fell at roughly the same time each year, between early and mid-August. As with the initial increase, there was also a lag between the maximum pressure and maximum sheet thickness approximately

2–7 weeks in length. Overall mean sheet thickness peaked each year at 0.516 m on August 16, 2016, 0.157 m on July 28, 2017, 0.209 m on August 20, 2018, and 0.323 m on August 18, 2019. Immediately after these maxima, sheet thickness began to decline. In 2016 and 2019, this decrease took the form of exponential decay to winter water levels. The decay in 2018 was linear, and the sheet was drained at a far slower rate of just $\sim$ 3–5 mm per week, thus resulting in much higher sheet thickness in the early months of 2019 when compared to other years.

Figure 3.13 depicts three important graphs in terms of assessing channelisation at Trinity-Wykeham Glaciers. Figure (a) shows the total meltwater production, (b) shows the total discharge through all edges with one node connected to the grounding line, and (c) shows the maximum discharge through any one such edge. Figure 3.14 features the maximal range attained by the channel network for each year, overlayed upon the basal topography.

Years 2016, 2017, and 2019 all exhibited similar patterns of channelisation. Multiple channels initially formed on the grounding line and transported larger volumes of water in response to increases in surface melt. Through the melt season, total discharge increased and one channel per glacier became the dominant means of channelised drainage; these channels extended up to the high-elevation regions of the bed on Trinity Glacier and well into the mid-elevation regions on Wykeham Glacier (see Figure 3.14). The main channels at Trinity Glacier had numerous branching tributaries along their lengths at higher elevations. Comparing Figures 3.13 (a) and (b), it is evident that the discharge through Trinity-Wykeham Glaciers' grounding lines both followed variations in meltwater production closely with little to no lag between increases in melt and spikes in rate of discharge. During each melt season, daily rates of discharge through the grounding line of Trinity Glacier exceeded those of Wykeham Glacier almost without exception, typically by $\sim$ 25–75% but occasionally reaching up to 100–150% greater, with a maximum of 52.4 m^3/s on July 27, 2017. Wykeham Glacier's total grounding line melt peaked 9 days prior on July 18, 2017, at 41.1 m^3/s. Between 2017 and 2019, single-channel discharge was also dominated by Trinity Glacier, the main channel of which discharged water at rates $\sim$ 2–10 times greater than those of Wykeham Glacier through the melt season. Mean grounding line discharge during peak melt, July 3 to August 22, was 28.3 m^3/s in 2016, 22.0 m^3/s in 2017, and 27.0 m^3/s in 2019. Maximum channel discharge occurred between mid-July and early August, and discharge subsequently decreased. The rate of decay in discharge appears to be exponential, but the discharge rate was highly sensitive to fluctuations in meltwater volume when compared to sheet thickness and, as such, fluctuated itself during this decay.

The year 2018 is of particular interest in terms of channel formation. Meltwater pro-

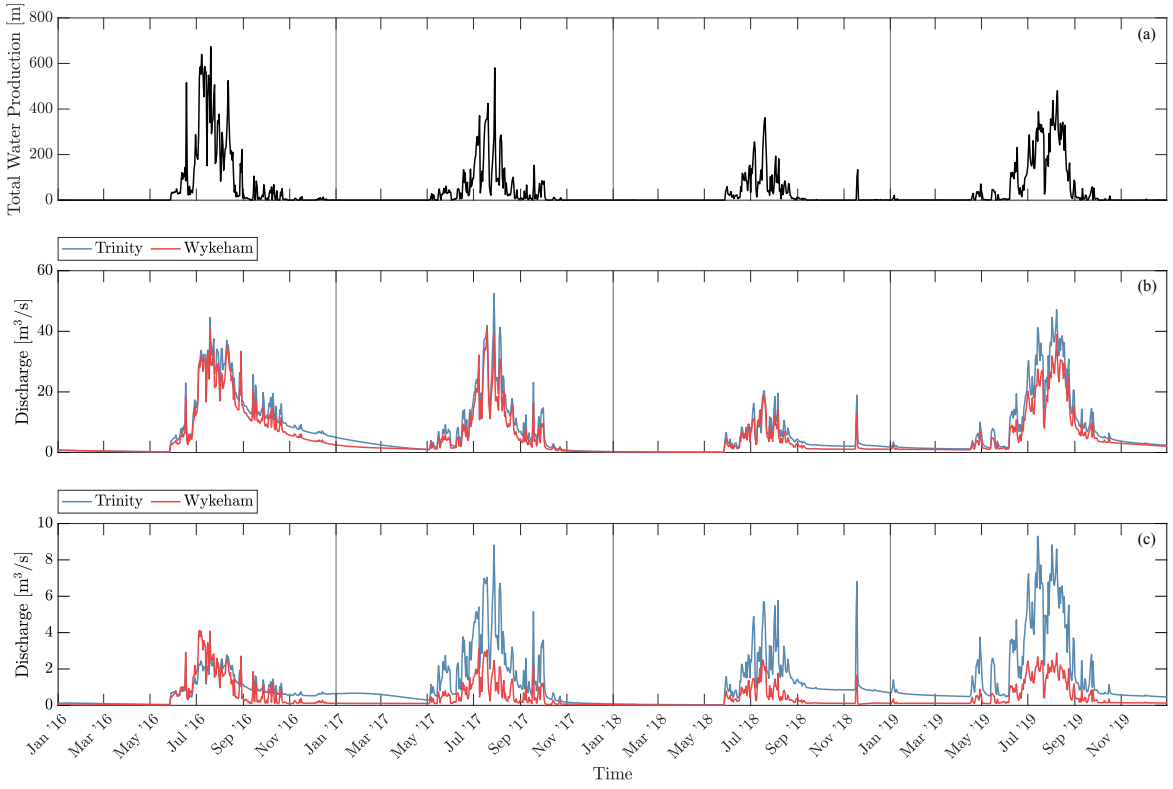

Figure 3.13: Maximum discharge through the grounding lines of Trinity-Wykeham Glaciers for 2016–2019. (a) Total meltwater production; (b) total discharge through grounding line nodes; (c) maximum discharge through any one grounding line node.

duction was considerably lower in 2018 compared to each other year, and this was reflected in the channel discharge. Peak grounding line discharge was 20.4 m^3/s, with a mean of just 8.8 m^3/s. Spatially, one main channel did form at the bed of Trinity-Wykeham Glaciers as in other years, but neither extended beyond the low-elevation regions of the glaciers (see Figure 3.14 (c)). Since channels were neither widespread nor high-volume in 2018, it seems that the distributed system dominated the subglacial hydrological network during this year. This agrees with the slow, linear decrease in sheet thickness after the melt season, and the excess of water stored in the distributed system at mid-elevation through the end of 2018 and beginning of 2019 (see Figure 3.5 (c)).

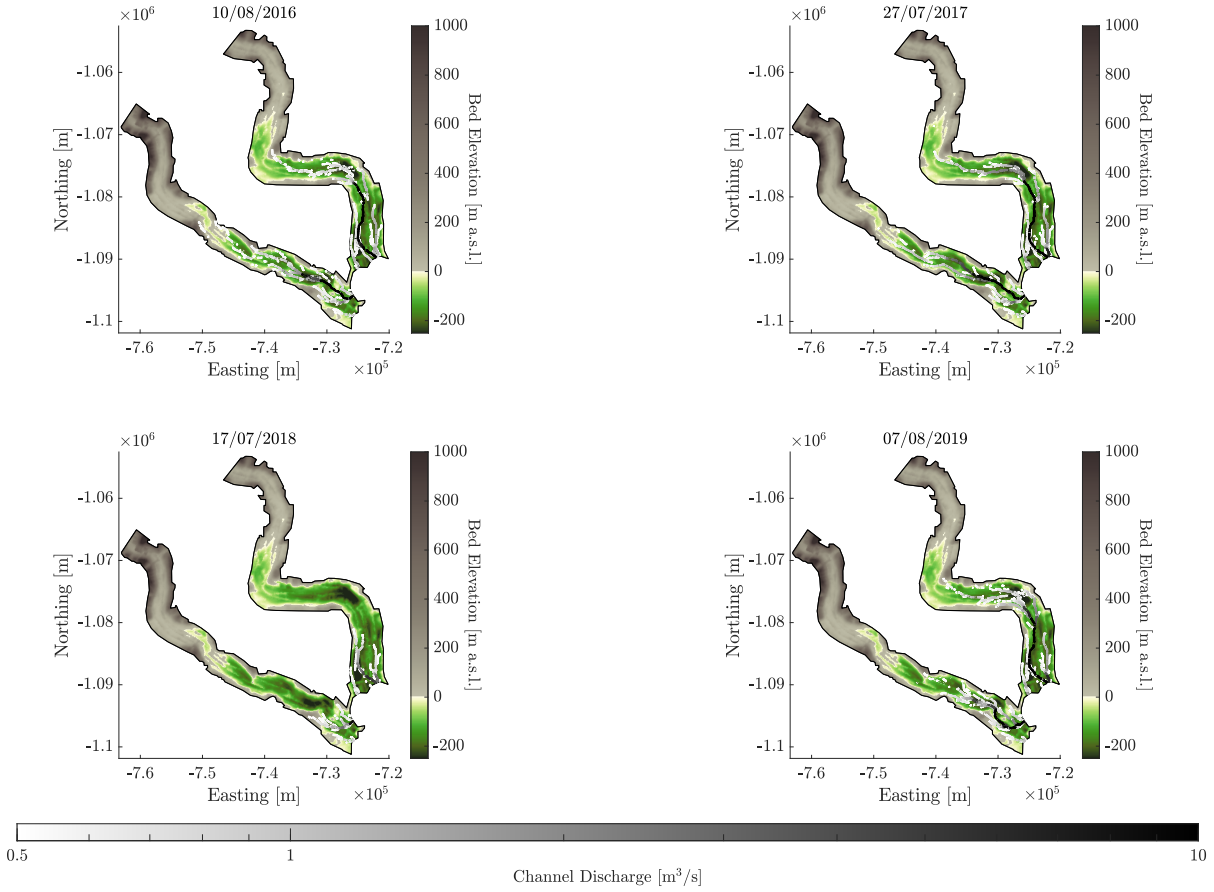

Figure 3.14: Maximal range of the subglacial channel network for the years 2016–2019, overlayed upon the basal topography. (a) 2016; (b) 2017; (c) 2018; (d) 2019.

3.1.3 Surface Velocity-Water Pressure Comparisons

In this section, glacier surface velocities derived from SAR acquisitions are compared to water pressure outputs (Friedl et al., 2021). Subglacial water pressure has been hypothesised to have a strong control on surface velocity and glacier dynamics in general (e.g., Anderson (2004); Iken and Bindschadler (1986)). To make these comparisons, the fractional change method described in Section 2.4 is implemented. Three time periods are considered for the comparisons:

- early melt season, early to mid-June, approximately 2–4 weeks after water pressure typically increases substantially;
- peak melt season, early to mid-July, shortly before or after mean subglacial water typically pressure peaks;
- post-melt season, late September to early October, once water pressure has typically dropped and surface meltwater input approaches zero.

Velocity mosaics and basal water pressure outputs are taken from these phases of the melt season and compared to those from before the melt season has begun. Velocities are compared to a monthly velocity mosaic from April of a given year, whereas water pressures are compared to the output from April 4 of that year.

Side-by-side comparisons between surface velocities and basal water pressure outputs can be seen below in Figures 3.15, 3.16, and 3.17. Missing data points are plotted in white. In general, flow was fastest near the grounding line at all times of year. Trinity Glacier often flowed at speeds above 1 km/yr at its grounding line, whereas Wykeham Glacier typically peaked around 700 m/yr during periods of accelerated flow. During periods of high meltwater production, velocities above 1 km/yr were observed further upglacier, and those grounding line velocities increased further. The year 2019 had the highest velocity during its melt season, with flow speeds approaching 1.5 km/yr. Once the melt season had ceased and subglacial water pressure had dropped, flow speed decreased abruptly on both glaciers, typically to levels well below those prior to the melt season.

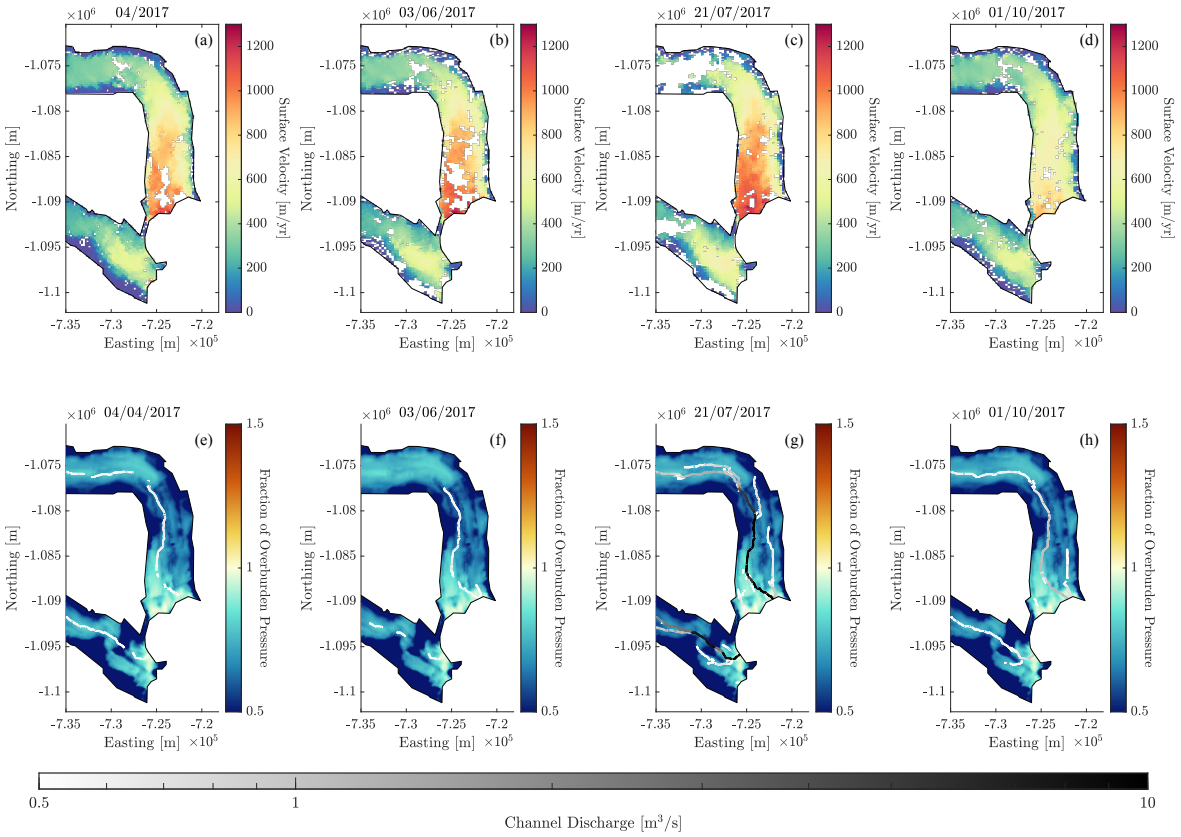

Figure 3.15: Top row: SAR derived surface velocity mosaics for Trinity-Wykeham Glaciers for 2017. Bottom row: Ratio of basal water pressure to overburden pressure for Trinity Wykeham Glaciers in 2017. Channel discharge is overlaid in grey. (a) Surface velocity mosaic for the month of 04/2017; (b) surface velocity mosaic for 03/06/2017; (c) surface velocity mosaic for 21/07/2017; (d) surface velocity mosaic for 01/10/2017; (e) basal water pressure for 04/04/2017; (f) basal water pressure for 03/06/2017; (g) basal water pressure for 21/07/2017; (h) basal water pressure for 01/10/2017.

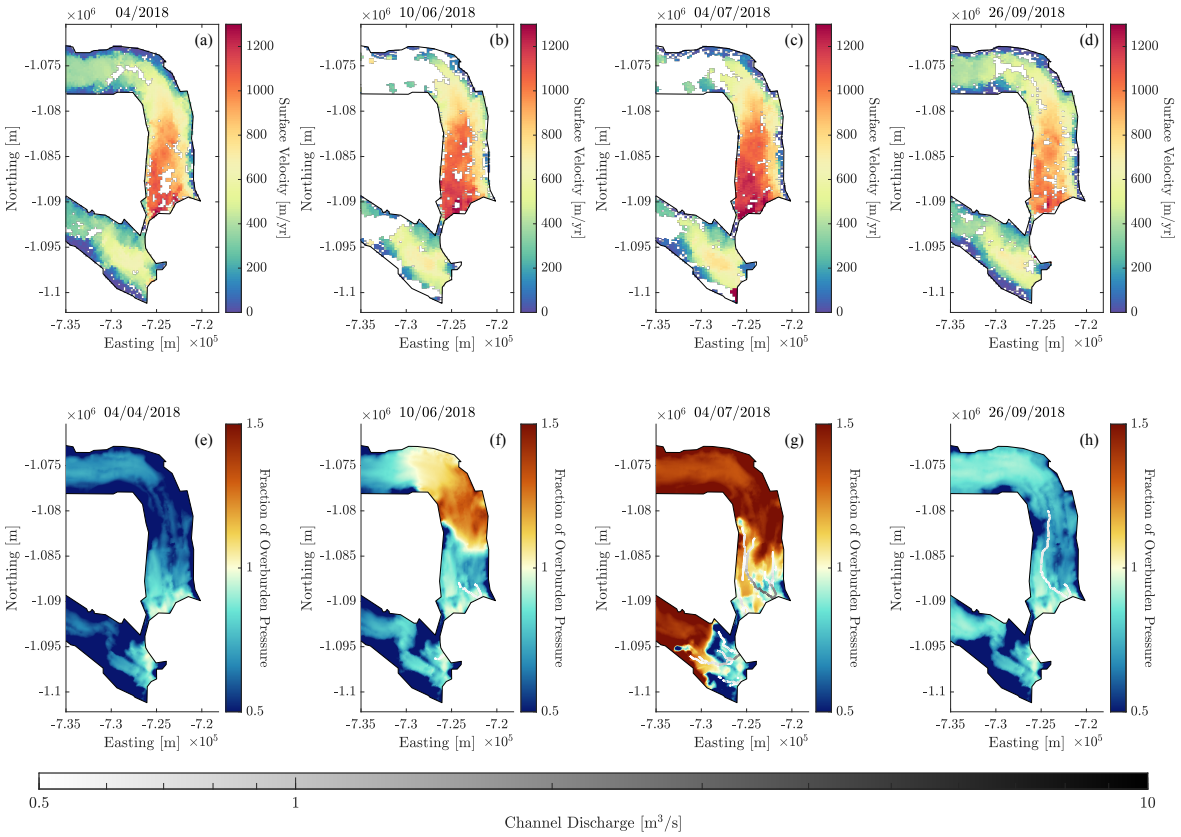

Figure 3.16: Top row: SAR derived surface velocity mosaics for Trinity-Wykeham Glaciers for 2018. Bottom row: Ratio of basal water pressure to overburden pressure for Trinity Wykeham Glaciers in 2018. Channel discharge is overlaid in grey. (a) Surface velocity mosaic for the month of 04/2018; (b) surface velocity mosaic for 10/06/2018; (c) surface velocity mosaic for 04/07/2018; (d) surface velocity mosaic for 26/09/2018; (e) basal water pressure for 04/04/2018; (f) basal water pressure for 10/06/2018; (g) basal water pressure for 04/07/2018; (h) basal water pressure for 26/09/2018.

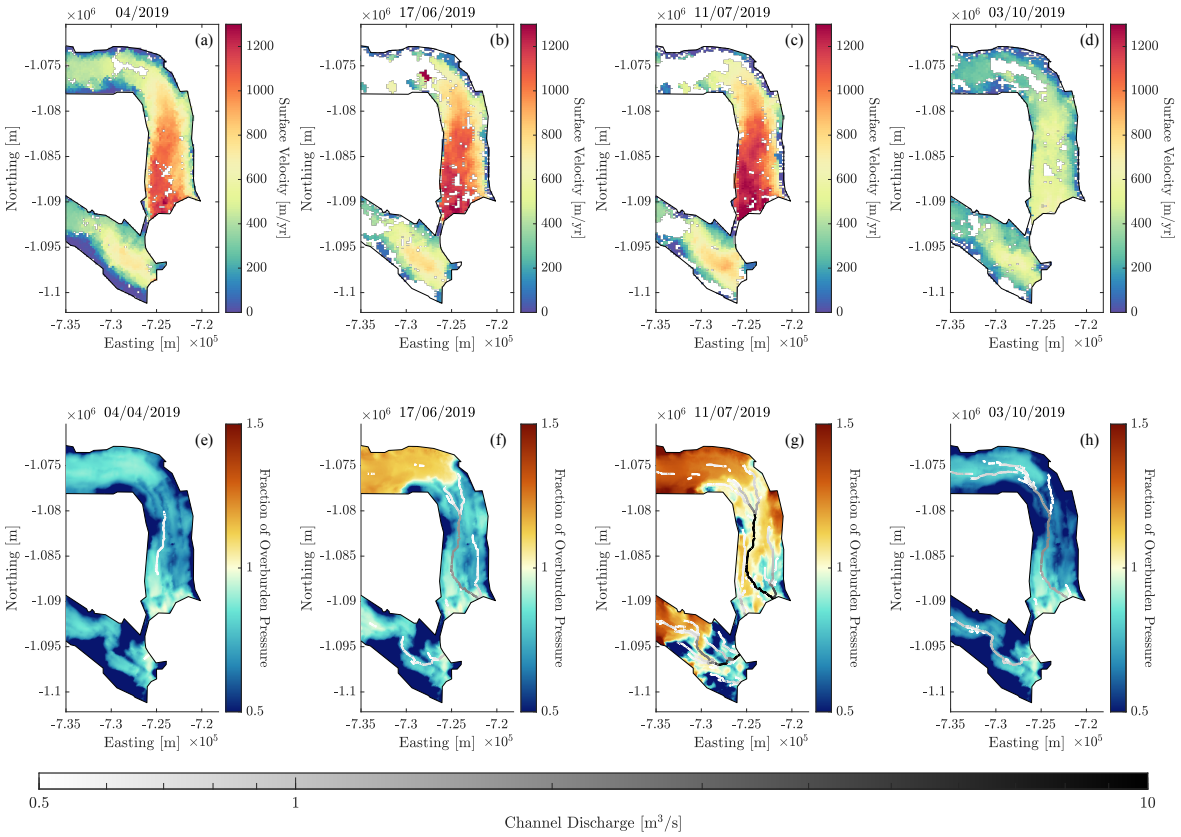

Figure 3.17: Top row: SAR derived surface velocity mosaics for Trinity-Wykeham Glaciers for 2019. Bottom row: Ratio of basal water pressure to overburden pressure for Trinity Wykeham Glaciers in 2019. Channel discharge is overlaid in grey. (a) Surface velocity mosaic for the month of 04/2019; (b) surface velocity mosaic for 17/06/2019; (c) surface velocity mosaic for 11/07/2019; (d) surface velocity mosaic for 03/10/2017; (e) basal water pressure for 04/04/2019; (f) basal water pressure for 17/06/2019; (g) basal water pressure for 11/07/2019; (h) basal water pressure for 03/10/2019.

Figure 3.18 depicts the fractional change in surface velocity and water pressure from pre-melt season values within the first month of the 2017, 2018, and 2019 melt seasons. Despite some interannual variation, a general pattern did emerge between the two variables. In 2017 and 2019, subglacial water pressure primarily increased along the valley walls of Trinity Glacier, with more subtle increases along the centre. Pressures more than doubled 10–15 km up Trinity Glacier in 2018, across the entire width of the trunk. The lower 5–10 km of Trinity Glacier underwent little to no change in water pressure during that period. Wykeham Glacier was less consistent between years in the early melt season. In 2017, the trunk of Wykeham Glacier was at $\sim$ 90% pressure as in April, and the valley walls were at about $\sim$ 110%. In the following two years, this configuration of high and low pressures is reversed. Pressures were elevated along the trunk of Wykeham Glacier and decreased along its margins, with 2018 being the year in which these changes were greatest, once again exceeding a 100% change in some areas. Early melt season velocities exhibited a pattern similar to that of the basal water pressure, in that the greatest changes in velocity also largely occurred on the margins of the glaciers. Along the centreline, velocity increased by $\sim$ 5–15% at Trinity Glacier. Along the valley walls of Trinity Glacier and much of Wykeham Glacier, flow was often 20–60% faster than prior to the melt season in 2017. These increases reached up to 80–110% in 2018, while still affecting a narrow band along the glacier periphery on Trinity Glacier and large regions of Wykeham Glacier. Early in the 2019 melt season, Trinity Glacier underwent acceleration similar to that of 2018, though along its eastern wall flow slowed substantially to as low as 10% of winter values. In all years, the flow slowed by $\sim$ 25–70% directly adjacent to the Wykeham Glacier grounding line.

Velocity changes during periods of the peak period of the melt season are depicted in Figure 3.19. The percent acceleration was once again fairly consistent between the three years. Peak-melt season velocities exceeded winter velocities by up to 80%, and slower flow along the marginal regions persisted into this period. The year 2019 saw the greatest acceleration over the largest area, and 2018 saw the least change to its flow regime between April and July. Water pressure patterns also varied between years. In 2017, pressure was largely unchanged from April, with small areas of the glaciers' trunks up to 20% lower. As seen in Figure 3.5 (b), pressure was highly sensitive to changes in melt and, as such, fluctuated dramatically throughout the melt season. Water pressure was at a local minimum—a "trough" in the pressure oscillations—on 21/07/2017, the date of comparison. In 2018, pressures exceeded 200% of the winter values over almost the entire comparison area, aside from within $\sim$ 3 km of the grounding line and in low-pressure patches along the valley walls. Pressure was similarly elevated in 2019, approaching 200% along the margins and $\sim$ 150% along the centreline.

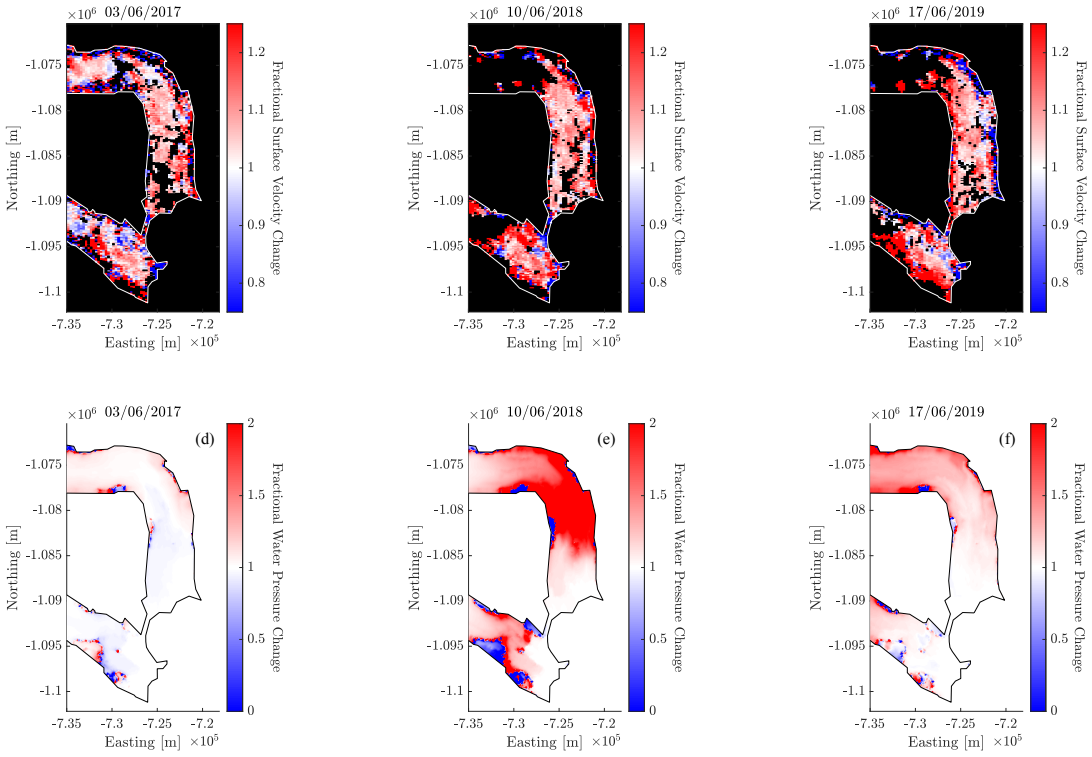

Figure 3.18: Top row: Fractional change in surface velocity from pre-melt season to early melt season (as defined in 2.4) at Trinity-Wykeham Glaciers for 2017–2019. Bottom row: Fractional change in basal water pressure from pre-melt season to early melt season (as defined in 2.4) at Trinity-Wykeham Glaciers for 2017–2019. (a) Change in surface velocity from the month of 04/2017 to 03/06/2017; (b) change in surface velocity from the month of 04/2018 to 10/06/2018; (c) change in surface velocity from the month of 04/2019 to 17/06/2019; (d) change in basal water pressure from 04/04/2017 to 03/06/2017; (e) change in basal water pressure from 04/04/2018 to 10/06/2018; (f) change in basal water pressure from 04/04/2019 to 17/06/2019.

Figure 3.20 shows the fractional change in velocity and water pressure after the melt season has ended. In each year, flow speeds decreased from their elevated values during the melt season, and in 2017 and 2019, much of Trinity Glacier flowed at velocities well

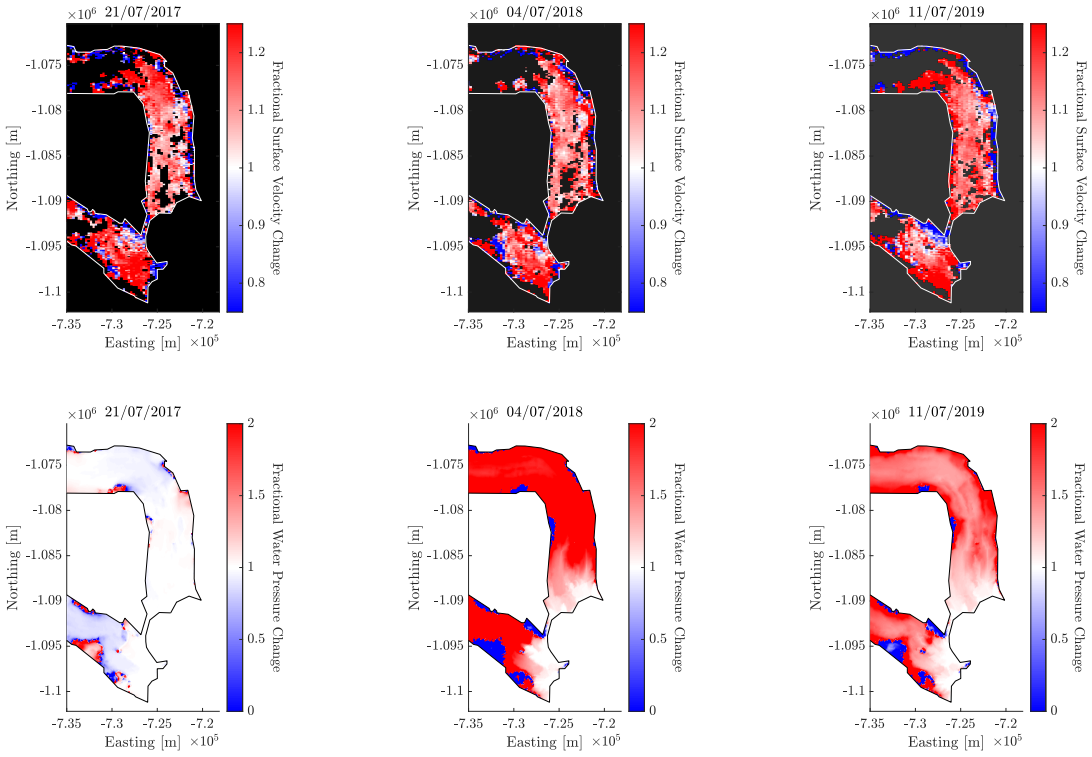

Figure 3.19: Top row: Fractional change in surface velocity from pre-melt season to peak-melt season (as defined in 2.4) at Trinity-Wykeham Glaciers for 2017–2019. Bottom row: Fractional change in basal water pressure from pre-melt season to early melt season (as defined in 2.4) at Trinity-Wykeham Glaciers for 2017–2019. (a) Change in surface velocity from the month of 04/2017 to 21/07/2017; (b) change in surface velocity from the month of 04/2018 to 04/07/2018; (c) change in surface velocity from the month of 04/2019 to 11/07/2019; (d) change in basal water pressure from 04/04/2017 to 21/07/2017; (e) change in basal water pressure from 04/04/2018 to 04/07/2018; (f) change in basal water pressure from 04/04/2019 to 11/07/2019.

below the corresponding pre-melt season rates. The lower $\sim$ 10–15 km of Trinity Glacier flowed at about 70–80% velocity during 2017, a substantial decrease compared to the 350% reached during the melt season. Wykeham Glacier continued to flow at elevated

rates comparable to the peak of the melt season, especially along its southern margin. Surface velocity remained relatively high after the 2018 melt season. A large area near the terminus of Trinity Glacier continued to flow above 1 km/yr despite slowing to $\sim$ 50–90% of the prior winter velocity, with the greatest decrease occurring along the eastern margin. Surface velocity at Wykeham Glacier also decreased from the peak of the melt season but still exceeded that of the previous winter. Surface velocity after the 2019 melt season decreased significantly at both glaciers. Trinity Glacier slowed down to 35–55% velocity across the entirety of its trunk which was used in the comparison after the melt season had ended. Much of Wykeham Glacier slowed to about 60–90%, aside from a narrow band along the southern wall which still approached 200% of the winter velocity. Basal water pressure similarly dropped after the melt season had ended. In 2017 and 2019, basal water pressure was just below winter values (within $\sim$ 20%) across the majority of the domain, save for small patches of elevated pressure along the glacier margins where valley walls are steepest. Pressure was comparatively high after the 2018 melt season, with much of both glacier trunks at pressures 1.2–1.6 times those attained in April 2018. Marginal areas were also under higher pressure in 2018.

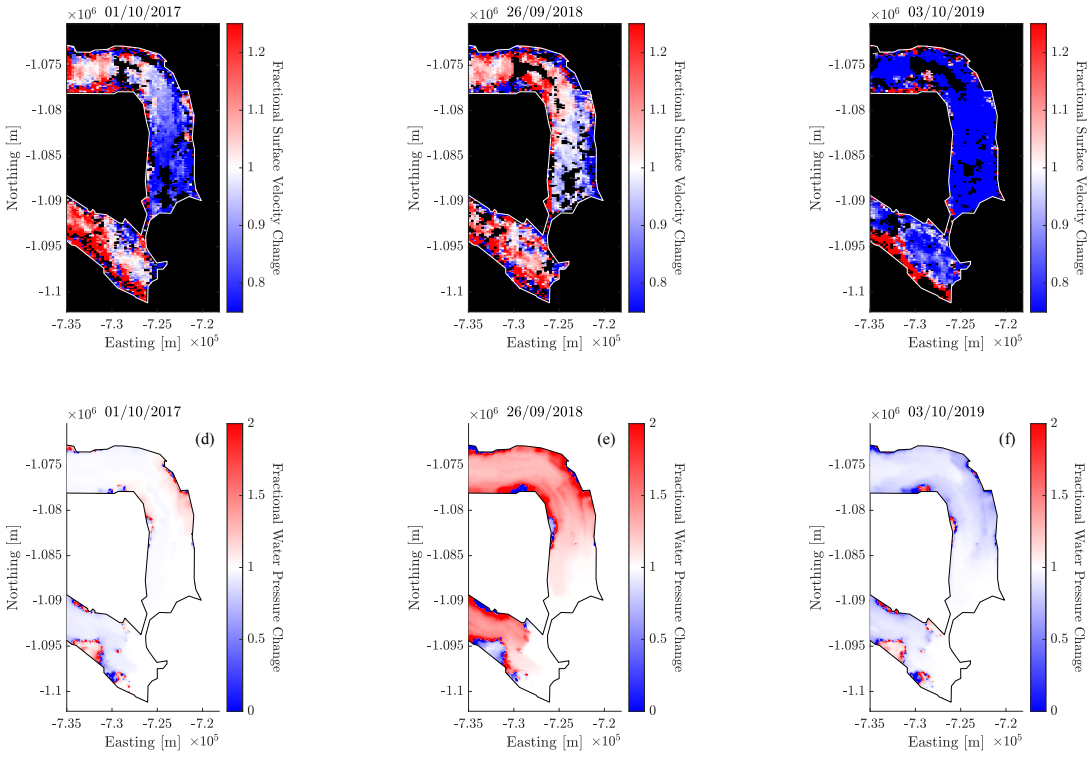

Figure 3.20: Top row: Fractional change in surface velocity from pre-melt season to post-melt season (as defined in 2.4) at Trinity-Wykeham Glaciers for 2017–2019. Bottom row: Fractional change in basal water pressure from post-melt season to early melt season (as defined in 2.4) at Trinity-Wykeham Glaciers for 2017–2019. (a) Change in surface velocity from the month of 04/2017 to 01/10/2017; (b) change in surface velocity from the month of 04/2018 to 26/09/2018; (c) change in surface velocity from the month of 04/2019 to 03/10/2019; (d) change in basal water pressure from 04/04/2017 to 01/10/2017; (e) change in basal water pressure from 04/04/2018 to 26/09/2018; (f) change in basal water pressure from 04/04/2019 to 03/10/2019.

3.2 Sensitivity Tests

Identical runs were completed for nine different combinations of k_c and k_s, as shown in Table 2.3 in order to gauge the effect these parameters may have on the subglacial hydrological system of Trinity-Wykeham Glaciers. Water pressure, water sheet thickness, and channel discharge outputs are compared on four dates in 2017:

- 19/04/2017, prior to the beginning of the melt season;
- 28/06/2017, early in the melt season;
- 18/07/2017, during the peak of the melt season;
- 26/10/2017, after the melt season has ended.

These four dates are chosen to show how channel and sheet conductivities changed the system's behaviour during the four main stages of the melt season. Time series of meltwater input, basal water pressure, and water sheet thickness throughout the simulation period are seen in Figure 3.21. This figure demonstrates that the time series took on the same general shape across all runs, varying primarily in magnitude, but there are important distinctions to be drawn resulting from the interplay between low and high conductivities imposed in the subglacial hydrological system.

3.2.1 Basal Water Pressure

First, consider the effects of varying channel and sheet conductivities on water pressure at the bed of Trinity-Wykeham Glaciers. As before, basal water pressure is plotted as a ratio of water pressure outputs to overburden pressure. Figure 3.22 shows basal water pressure outputs for 19/04/2017, a date representative of pressures prior to the 2017 melt season. The greatest domain-wide pressure was attained in Run 9, in which both conductivities were assigned their lowest value. Mean basal water pressure was 74.4% overburden, 19.8% overburden higher than the baseline run (Run 5). The lowest pressure of 36.6% was observed when both conductivities were set to their highest values in Run 1. The remaining runs had basal water pressures between 45.2% and 63.6%. Trinity and Wykeham Glaciers exhibited similar patterns of pressurisation in all runs other than Run 7 which showed Trinity Glacier approaching overburden pressure along much of its trunk, and Wykeham Glacier at a pressure similar to the other runs in which k_c was high; both glaciers exhibited the most extensive winter channel formation in Run 7 as well. Neither k_c nor k_s appear to

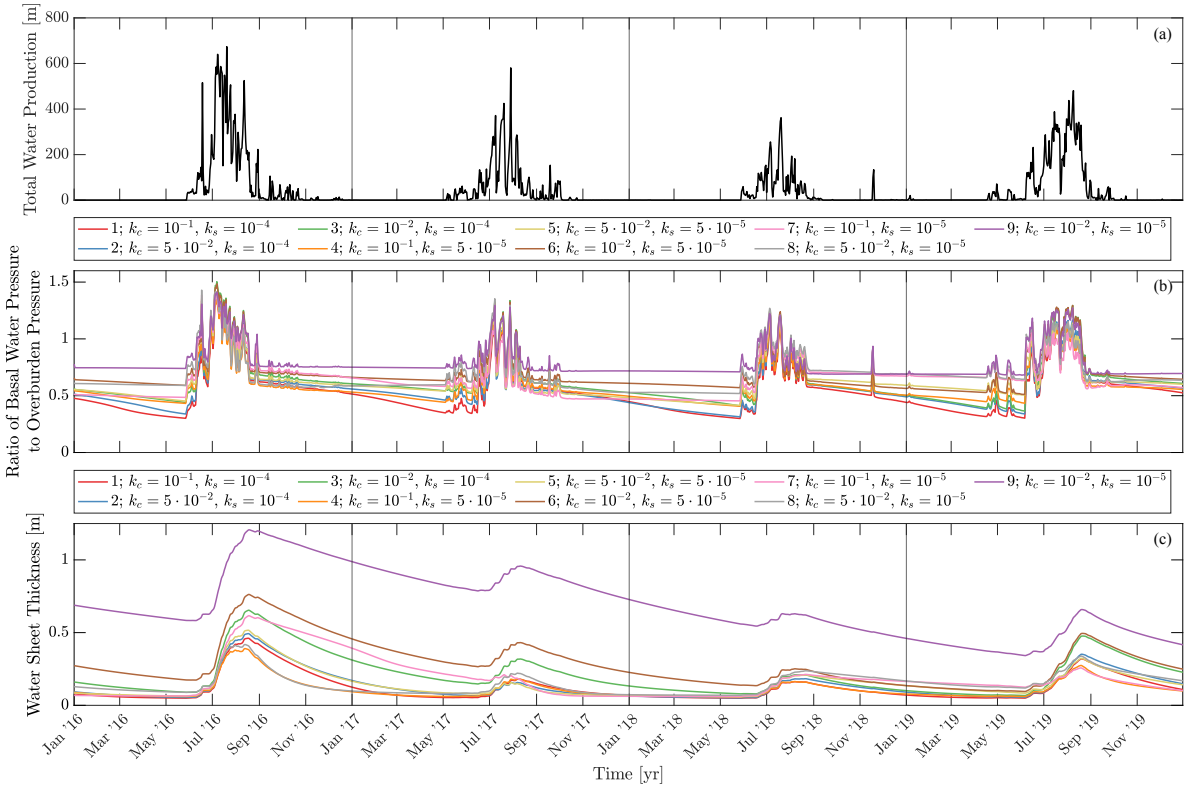

Figure 3.21: Mean model outputs at Trinity-Wykeham Glaciers for 2016–2019 for all combinations of k_c and k_s as listed in Table 2.3. (a) Total meltwater production; (b) mean basal water pressure, expressed as a ratio of basal water pressure to overburden pressure; (c) mean subglacial water sheet thickness.

have significantly stronger control on winter water pressures. Rather, lower conductivities applied to either the sheet or channels resulted in higher pressures during months of little or no melt.

Figure 3.23 shows basal water pressure outputs on 28/06/2017, shortly after meltwater production accelerated at Trinity-Wykeham Glaciers. The lowest mean water pressure still belonged to Run 1 at 59.2%, although patterns of pressure were fairly consistent across runs, with a few exceptions. Across all runs, pressures were relatively low, i.e., below overburden pressure, at the lowest 5 to 10 km of both glacier's trunks adjacent to the grounding line, with additional low-pressure bands observed further upglacier in close

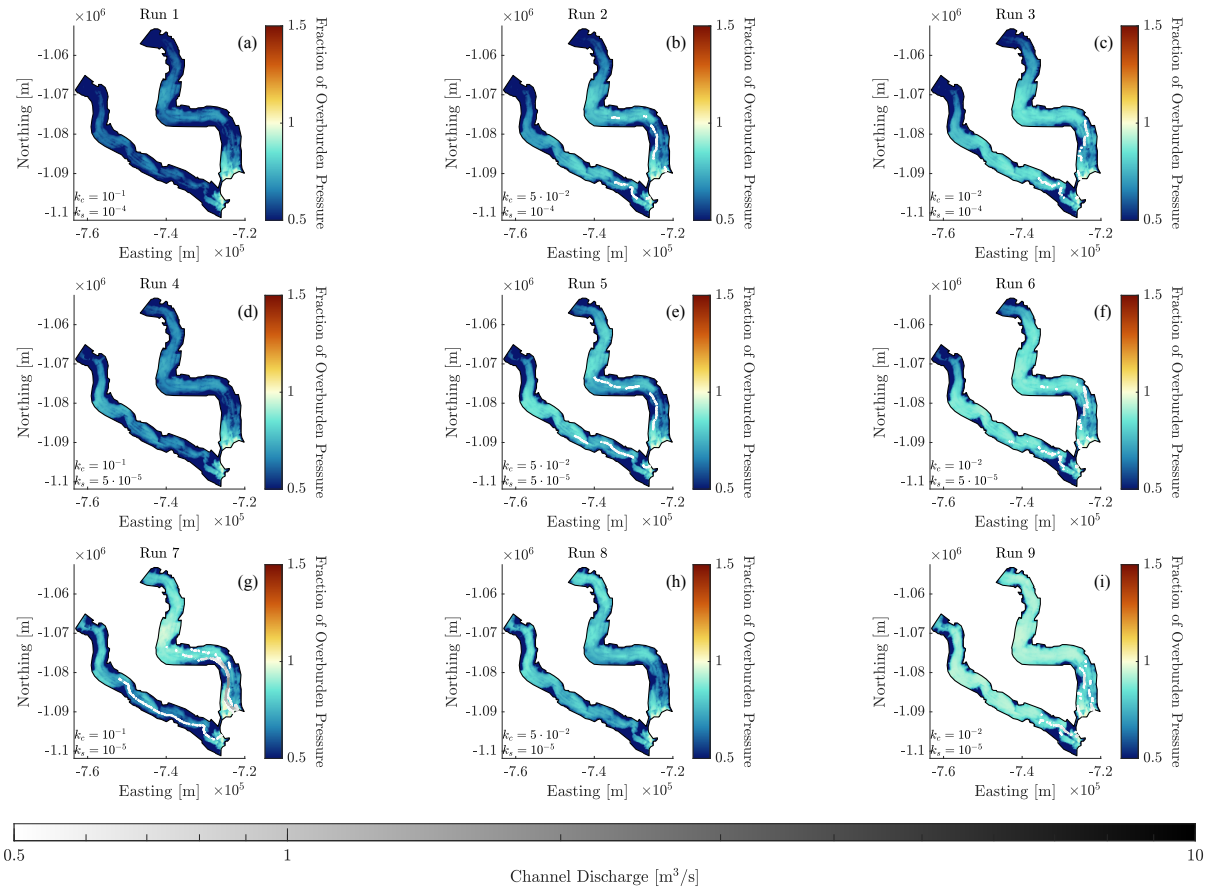

Figure 3.22: Ratio of basal water pressure to overburden pressure for Trinity-Wykeham Glaciers on 19/04/2017 for all combinations of channel conductivity k_c and sheet conductivity k_s. Channel discharge is overlaid in grey. (a) Run 1; (b) Run 2; (c) Run 3; (d) Run 4; (e) Run 5; (f) Run 6; (g) Run 7; (h) Run 8; (i) Run 9. See Table 2.3 for conductivities corresponding to each run.

proximity to high-volume channels. These channels formed on Trinity Glacier in all runs other than those in which channel conductivity was at its lowest value, $k_c = 10^{-2}$ $\mathrm{m}^{3/2}$ $\mathrm{kg}^{-1/2}$. Short, disjoint channels with low discharge formed when channel conductivity was set to this value. During this phase of the melt season, the mid-elevation area of both glaciers was at the highest pressure, whereas the upper reaches of the glaciers remained, in most cases, at water pressures comparable to those prior to the melt season. The most

notable departure from this configuration of pressures was in the case of Run 9. Run 9 had the greatest mean pressure of any run at this output date at 90.2%, but pressures in mid-altitudes only marginally exceeded overburden pressure at Trinity Glacier and did not exceed overburden at Wykeham Glacier. The other outlier was Run 7; Wykeham Glacier's pressure regime resembles other runs, but Trinity Glacier's mid and high-elevation areas were at 5% to 10% lower pressure than observed on 19/04/2017, and a high-discharge channel extends over 30 km upglacier.

In 2017, overall water pressure peaked in mid to late July. Figure 3.24 presents basal water pressure outputs on 18/07/2017, and best demonstrates the influence that sheet and channel conductivity had on subglacial drainage. Run 3, in which sheet conductivity was highest and channel conductivity was lowest, exhibited the greatest mean water pressure on this date. Channelisation was very limited in Run 3, with the network composed almost entirely of very short, very low discharge channels dispersed across the lower trunks of both glaciers; there was no one primary channel that facilitated efficient drainage. In contrast, Run 7 in which sheet conductivity was lowest and channel conductivity was highest, was at the lowest pressure of all runs at that time. High-volume channels extended approximately 42 km and 26 km upglacier from the grounding line at Trinity and Wykeham Glaciers respectively, the greatest channel length in any run. Similar channels formed in runs in which $k_c > 10^{-2}$ $m^{3/2}$ $kg^{-1/2}$, and basal water pressure was decreased significantly in the vicinity of these channels, particularly in areas where the channels' discharge exceeded 1 m^3/s. It should be noted that the three highest mean pressures were seen in Runs 3, 6, and 9 at 123.8%, 123.0%, and 120.2%, which indicates some positive relationship between pressure and sheet conductivity, albeit a minor one. The three lowest pressures were seen in Runs 7, 1, and 4 at 103.5%, 109.3%, and 110.4%.

Figure 3.25 shows basal water pressure outputs for 26/10/2017 and Figure 3.26 is a difference plot, subtracting the pressures from 19/04/2017 from the 26/10/2017 values to assess how the 2017 melt season altered the state of the bed of Trinity-Wykeham Glaciers with respect to each combination of conductivities. Run 9 once again exhibited the highest pressure at 71.6% overburden, only 2.8% lower than the winter value. Run 7 was the lowest at 47.2%, an 11.3% drop from 58.5% in April. In all runs, the pressure was nearly identical to the pre-melt season value within $\sim$ 3 km of the grounding line. Otherwise, there was little consistency between runs in terms of comparing pressures before and after the melt season, although Runs 2, 3, 5, and 6 shared some broad similarities in their respective difference plots. For these runs, basal pressures were up to 10% lower at low and mid-elevations and up to 25% higher at high elevation on 26/10/2017 compared to 19/04/2017. The difference plots in which k_c was highest and/or k_s was lowest (Runs 1, 4, 7, 8, and 9) each exhibited unique patterns. In Run 1, the difference in pressure increased spatially

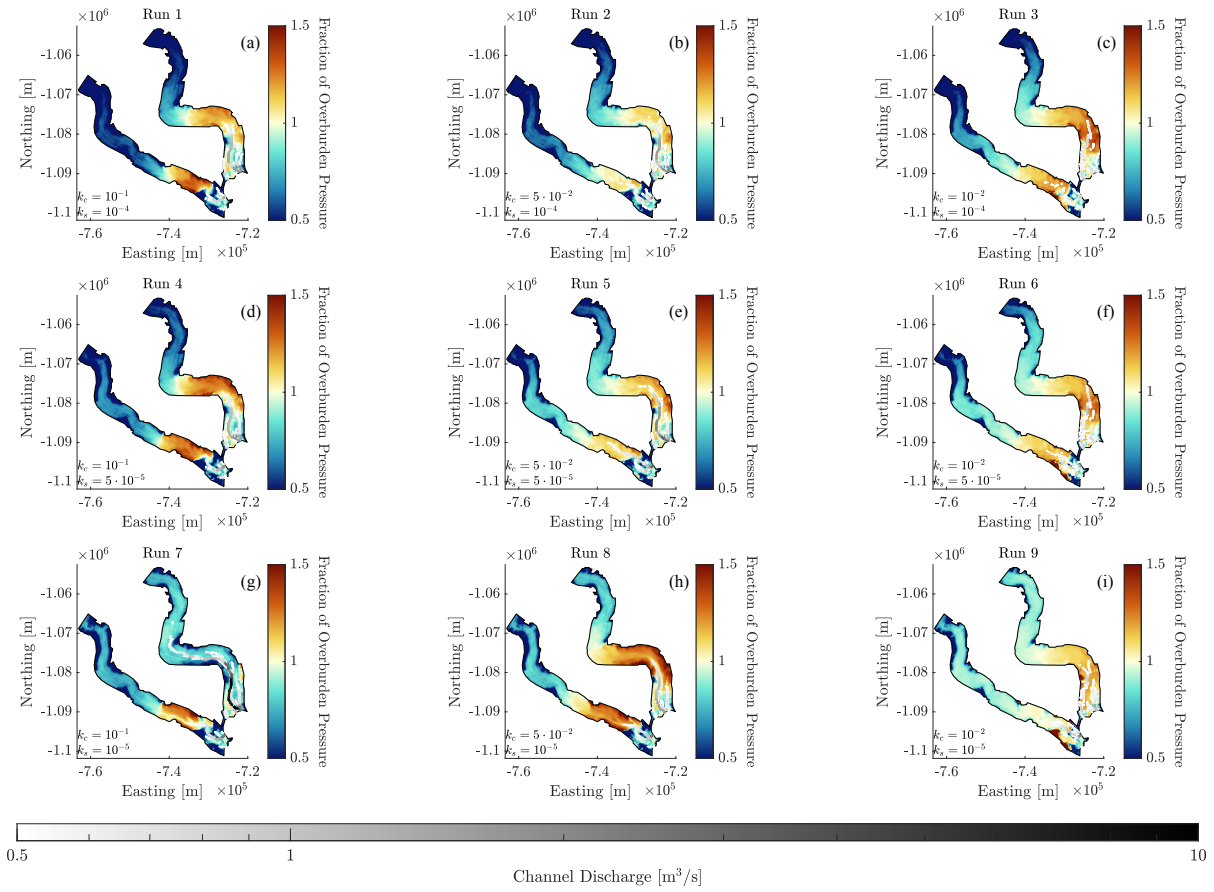

Figure 3.23: Ratio of basal water pressure to overburden pressure for Trinity-Wykeham Glaciers on 28/06/2017 for all combinations of channel conductivity k_c and sheet conductivity k_s. Channel discharge is overlaid in grey. (a) Run 1; (b) Run 2; (c) Run 3; (d) Run 4; (e) Run 5; (f) Run 6; (g) Run 7; (h) Run 8; (i) Run 9. See Table 2.3 for conductivities corresponding to each run.

from $\sim$ 5% at low elevation to $\sim$ 25% along the mid and upper trunk of Trinity Glacier, and Wykeham Glacier was 20–25% higher along the majority of its trunk. Trinity Glacier was very similar in Run 4, though Wykeham Glacier was only $\sim$ 10% higher than the April output. Run 7 interestingly showed quite the opposite of the previous two runs, despite the fact that they each share $k_s = 10^{-1}$ m$^{7/4}$ kg$^{-1/2}$; much of Trinity Glacier was at 20–25% lower pressure in September than in the April output, and Wykeham Glacier was also up

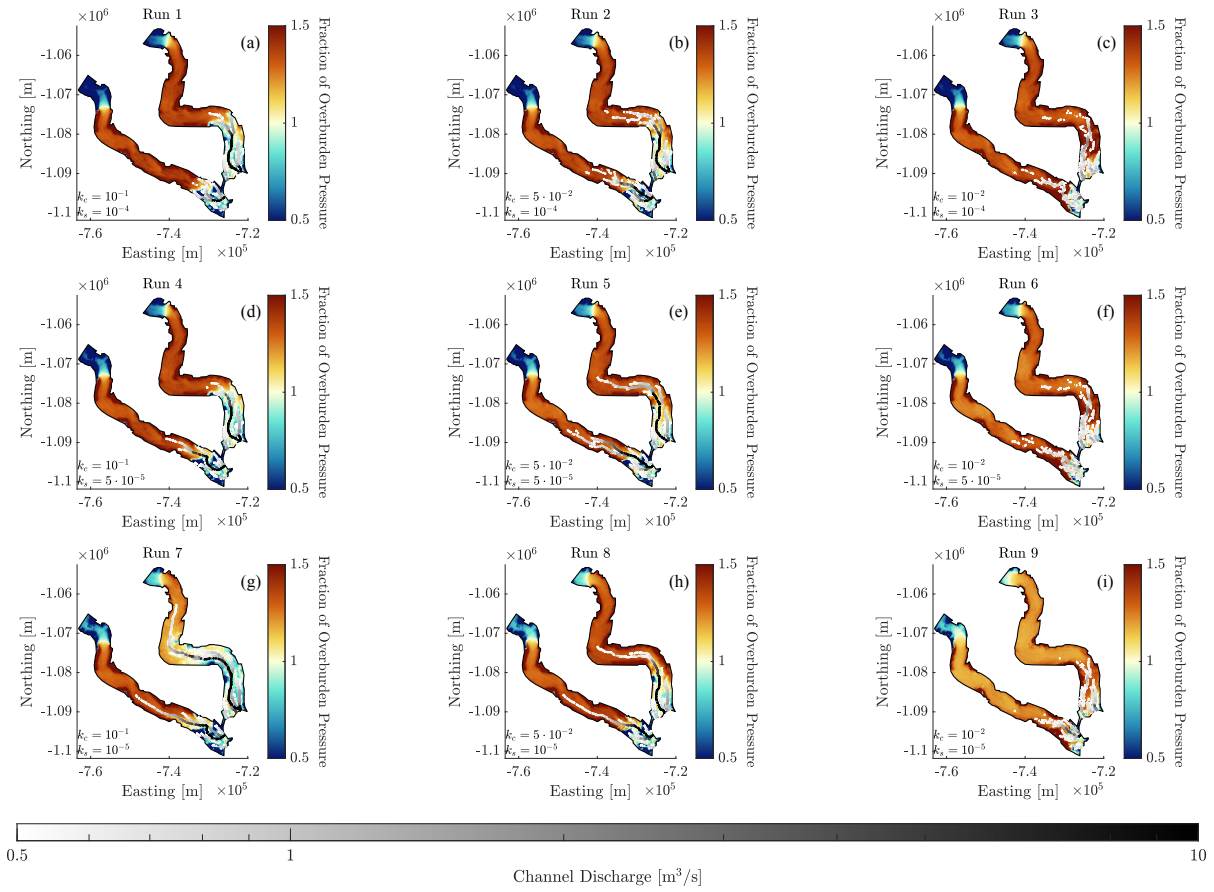

Figure 3.24: Ratio of basal water pressure to overburden pressure for Trinity-Wykeham Glaciers on 18/07/2017 for all combinations of channel conductivity k_c and sheet conductivity k_s. Channel discharge is overlaid in grey. (a) Run 1; (b) Run 2; (c) Run 3; (d) Run 4; (e) Run 5; (f) Run 6; (g) Run 7; (h) Run 8; (i) Run 9. See Table 2.3 for conductivities corresponding to each run.

to 10% lower along its trunk. Run 8 produced pressures approximately 5–10% lower along the centreline of both glaciers, but with isolated areas of pressures 5–10% higher along the glacier margins. Lastly, in Run 9 in which both conductivities were lowest, all pressures were within 5% of April values aside from a small low-pressure patch on the southern wall of Wykeham Glacier.

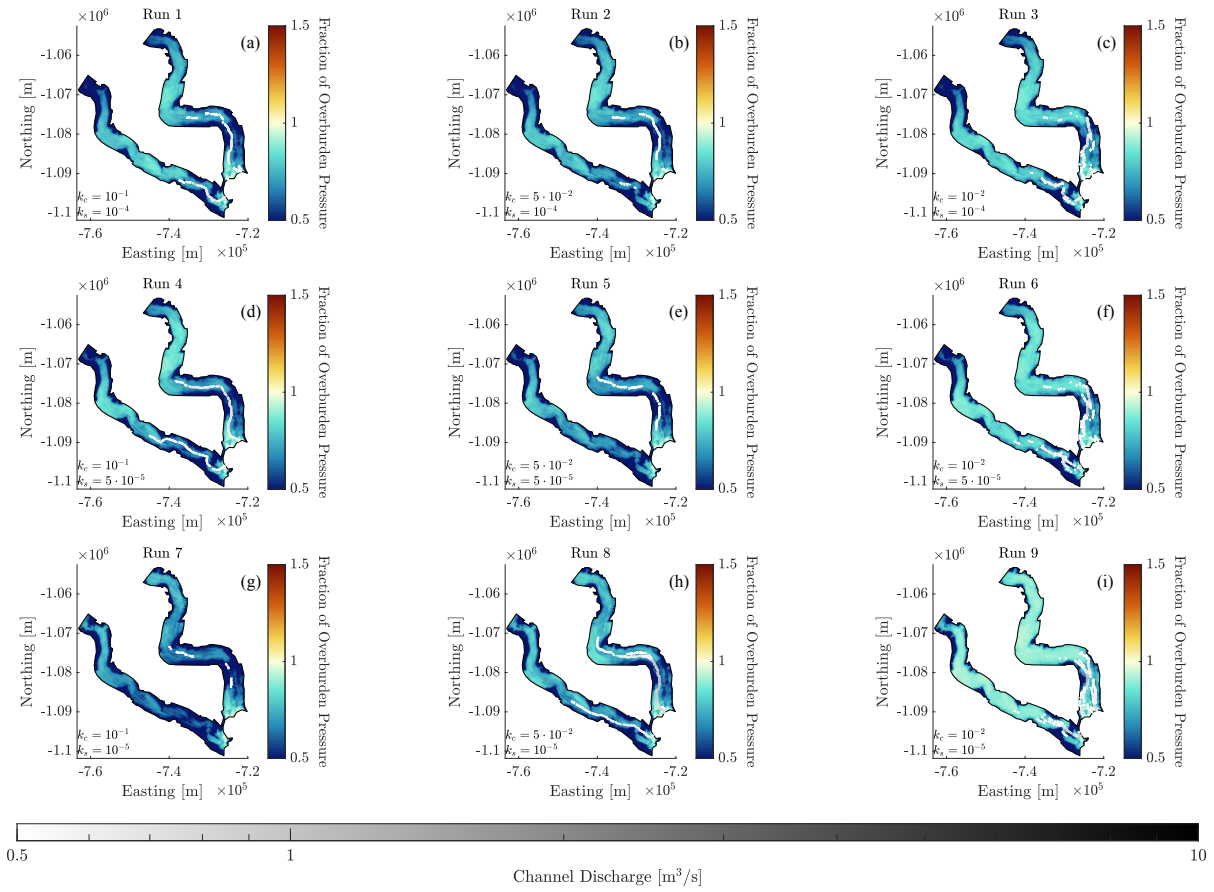

Figure 3.25: Ratio of basal water pressure to overburden pressure for Trinity-Wykeham Glaciers on 26/10/2017 for all combinations of channel conductivity k_c and sheet conductivity k_s. Channel discharge is overlaid in grey. (a) Run 1; (b) Run 2; (c) Run 3; (d) Run 4; (e) Run 5; (f) Run 6; (g) Run 7; (h) Run 8; (i) Run 9. See Table 2.3 for conductivities corresponding to each run.

3.2.2 Water Sheet Thickness

Water sheet thickness is plotted on a logarithmic scale for all runs. Figure 3.27 depicts sheet thickness on 19/04/17. For runs in which $k_c > 10^{-2}$ m$^{3/2}$ kg$^{-1/2}$, much of the domain had a sheet thickness of ~ 0.1 m prior to the 2017 melt season, with steep marginal areas with thin ice holding little to no water. A number of subglacial reservoirs in which water

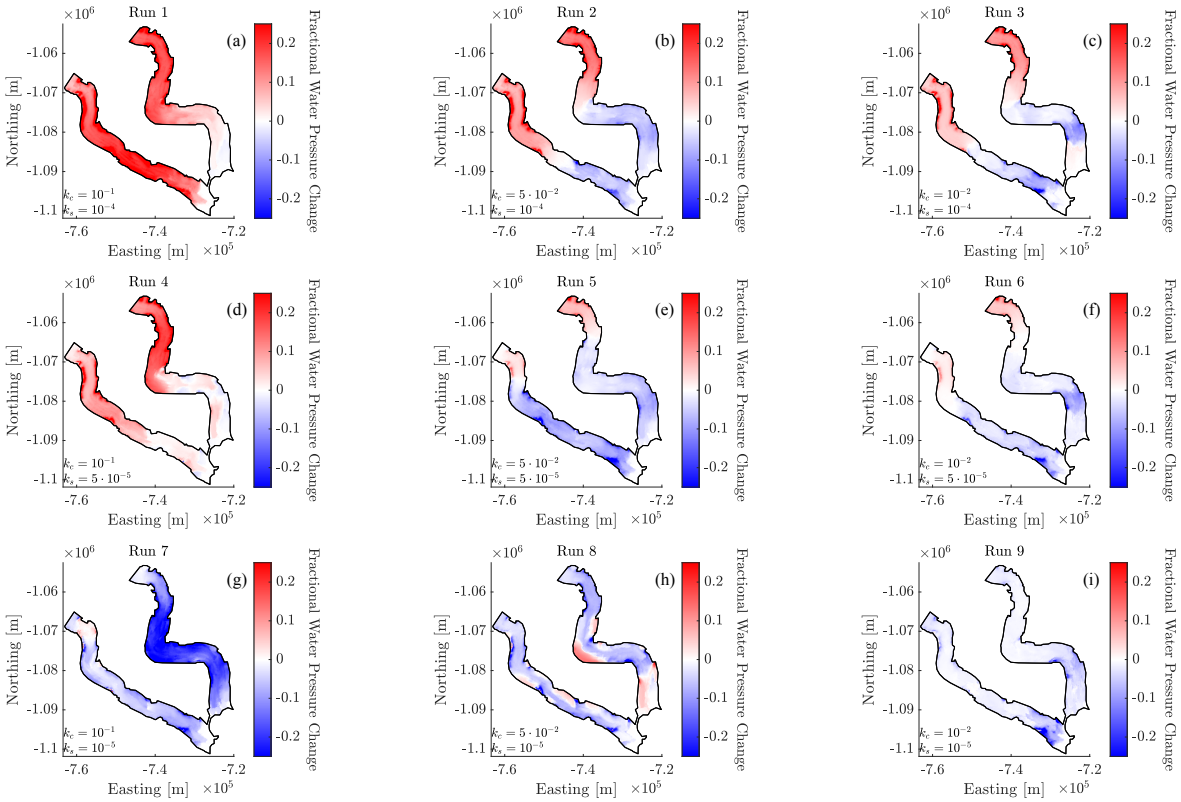

Figure 3.26: Difference in the ratio of basal water pressure to overburden pressure for Trinity-Wykeham Glaciers from 26/10/2017 to 19/04/2017 for all combinations of channel conductivity k_c and sheet conductivity k_s. Channel discharge is overlaid in grey. (a) Run 1; (b) Run 2; (c) Run 3; (d) Run 4; (e) Run 5; (f) Run 6; (g) Run 7; (h) Run 8; (i) Run 9. See Table 2.3 for conductivities corresponding to each run.

pooled were visible in these runs at both glaciers. The reservoir near the grounding line of Trinity Glacier, between $-1.084 \cdot 10^6$ m and $-1.089 \cdot 10^6$ m North, was present in all runs, although the volume of water contained varied between runs. Otherwise, reservoirs formed in the mid and high-altitude areas of the glaciers for Runs 2, 5, and 8 (in which $k_c = 0.05$ $\mathrm{m}^{3/2}\ \mathrm{kg}^{-1/2}$) with little consistency between the three runs. Run 7 showed a high volume of water occupying the distributed system of Trinity Glacier in its mid-to-high latitude regions, approaching a depth of 1 m. A channel of significant discharge extended from this

body of water to the grounding line of Trinity Glacier. Runs 3, 6, and 9 had the lowest channel conductivity, and showed a large quantity of water covering a larger percentage of the domain, with the greatest volume stored at mid-altitude. Unlike the area of high thickness seen in Run 7, the deeper water was not stored in one continuous body but in many irregular "patches" of water greater than or equal to 1 m in depth. Run 9 exhibited a mean sheet thickness far above the other runs at 0.842 m; for comparison, Run 6 exhibited the second highest mean sheet thickness on this date at 0.312 m, only $\sim 37\%$ of the Run 9 mean. The remaining runs each had a mean sheet thickness < 0.25m and Run 1 exhibited the lowest at 0.055 m.

In the early melt season, specifically on 28/06/2017, the mean water sheet thickness was largely unchanged. Figure 3.28 depicts the water sheet thickness for all runs on 28/06/2017. Runs 1, 4, and 8 experienced a minor increase in mean sheet thickness (< 0.015 m), reaching 0.064 m, 0.074 m, and 0.096 m respectively. All other runs saw a decrease in sheet thickness. The greatest change occurred in Run 7, which had a mean thickness of 0.171 m, a decrease of 0.056 m. This was reflected in the noticeable reduction of water thickness in the mid- to high-altitude area of Trinity Glacier, and the increased discharge through the main channel that extended into that region. Mean sheet thickness in Run 9 was 0.790 m, a decrease of 0.052 m but still $\sim 293\%$ of the next highest mean, 0.270 m as observed in Run 6. The lowest mean sheet thickness was Run 1 at 0.064 m. For runs in which $k_c > 10^{-2}$ $\mathrm{m}^{3/2}$ $\mathrm{kg}^{-1/2}$, elevated sheet thickness was observed in the low-mid altitude area of Trinity Glacier, and a long, high-discharge channel formed, extending through this area of increased thickness and into the mid-altitude region of the glacier. A similar, shorter channel also formed at the grounding line of Wykeham Glacier in these runs.

The date 18/07/2017 represents the peak of the 2017 melt season. At this time, water sheet thickness was elevated from pre-melt season values for all conductivities. Figure 3.29 depicts the water sheet thickness outputs for 18/07/2017. Runs 3, 6, and 9 each had the lowest channel conductivity, and also underwent the largest increase in mean sheet thickness, each greater than 0.1 m. Run 9 continued to hold the highest mean sheet thickness at 0.892 m, Run 6 was second at 0.372 m, and Run 3 was third at 0.258 m. Run 7 had the greatest channel conductivity and the lowest sheet conductivity, and as such the subglacial water sheet underwent the smallest increase in thickness at just 0.036 m. However, the large channels in this run reached the greatest length (~ 25 km at Wykeham Glacier and ~ 40 km at Trinity Glacier) and transported the greatest volume of water of any run. Similar channels formed in Runs 1, 2, 4, 5, and 8, but only reached lengths of 15–30 km on Trinity Glacier. Sheet thickness resembled pre-melt season values in the lower elevation area of each glacier in each run. The most significant increase in sheet thickness

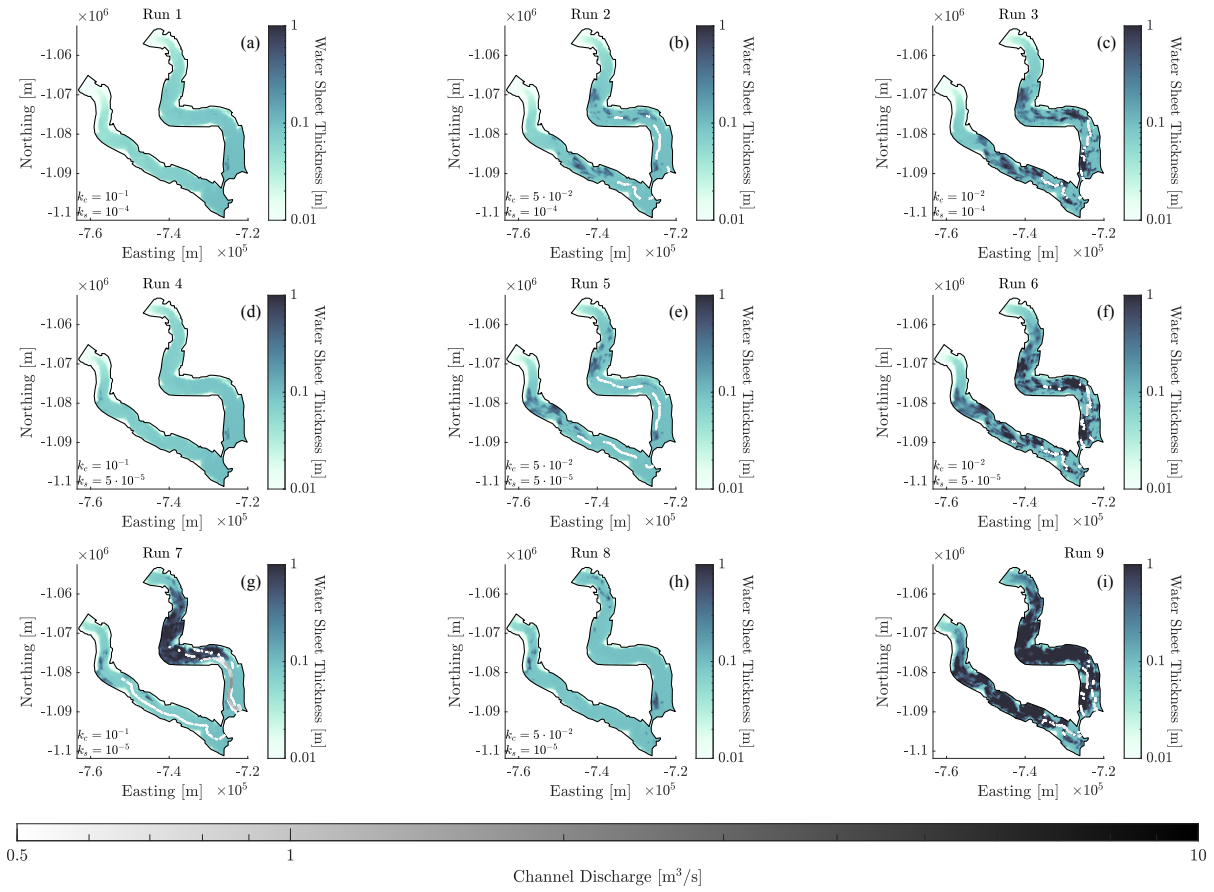

Figure 3.27: Subglacial water sheet thickness for Trinity-Wykeham Glaciers on 19/04/2017 for all combinations of channel conductivity k_c and sheet conductivity k_s. Channel discharge is overlaid in grey. (a) Run 1; (b) Run 2; (c) Run 3; (d) Run 4; (e) Run 5; (f) Run 6; (g) Run 7; (h) Run 8; (i) Run 9. See Table 2.3 for conductivities corresponding to each run.

was in the mid-elevation range. Run 2 had the lowest mean sheet thickness at 0.137 m.

After the melt season, sheet thickness generally decreased much more gradually than subglacial water pressure. Figure 3.30 shows water sheet thickness outputs for all runs on 26/10/2017. Runs 9, 6, and 3 each decreased by 0.025 m or less since 18/07/2017, and continued to hold the three highest mean sheet thicknesses at 0.878 m, 0.347 m, and

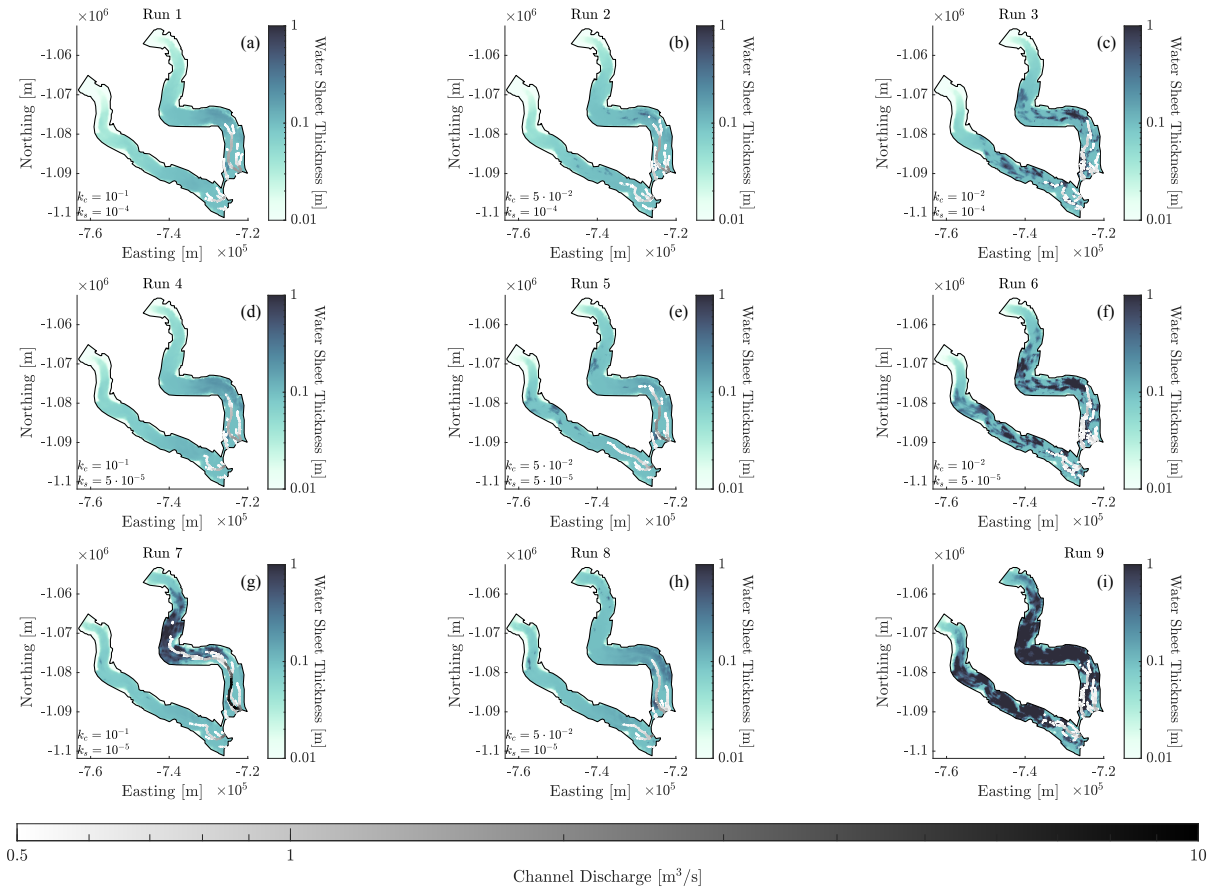

Figure 3.28: Subglacial water sheet thickness for Trinity-Wykeham Glaciers on 28/06/2017 for all combinations of channel conductivity k_c and sheet conductivity k_s. Channel discharge is overlaid in grey. (a) Run 1; (b) Run 2; (c) Run 3; (d) Run 4; (e) Run 5; (f) Run 6; (g) Run 7; (h) Run 8; (i) Run 9. See Table 2.3 for conductivities corresponding to each run.

0.234 m respectively. Run 7 underwent the greatest decrease in mean sheet thickness, decreasing to 0.075, 0.152 m below the mean before the melt season began. Runs 1, 2, 4, 5, and 8 all showed water remaining in the mid-altitude region of the distributed network of both glaciers. Channel discharge was substantially decreased from the melt season as well, although the channels do persist far upglacier.

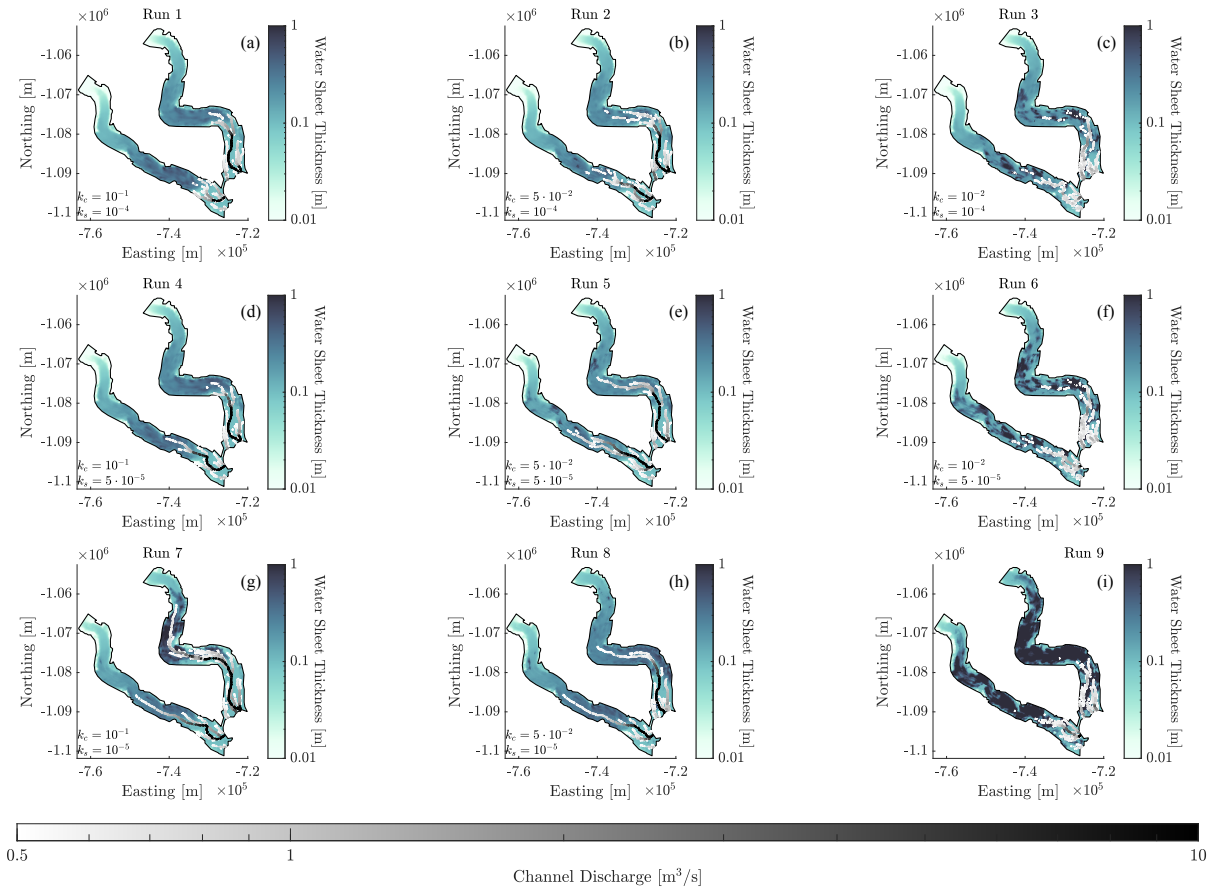

Figure 3.29: Subglacial water sheet thickness for Trinity-Wykeham Glaciers on 18/07/2017 for all combinations of channel conductivity k_c and sheet conductivity k_s. Channel discharge is overlaid in grey. (a) Run 1; (b) Run 2; (c) Run 3; (d) Run 4; (e) Run 5; (f) Run 6; (g) Run 7; (h) Run 8; (i) Run 9. See Table 2.3 for conductivities corresponding to each run.

3.2.3 Channel Discharge

Figures 3.22 through 3.30 show the location and discharge of subglacial channels through 2017 for all nine sensitivity tests. Figures 3.31 and 3.32 depict time series of the channel discharge through the grounding line of Trinity Glacier and Wykeham Glacier respectively from 2016 to 2019 for each combination of k_c and k_s. In each figure, subplot (a) depicts

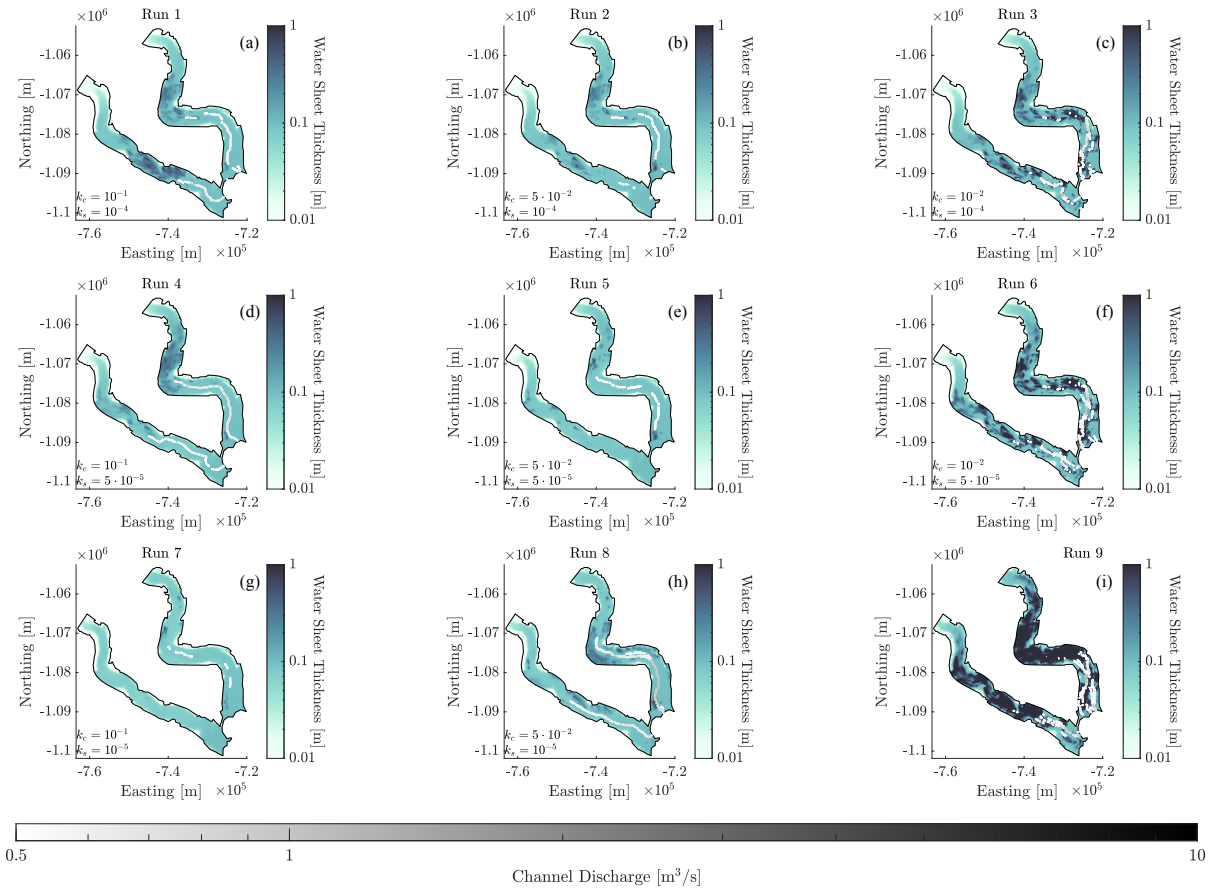

Figure 3.30: Subglacial water sheet thickness for Trinity-Wykeham Glaciers on 26/10/2017 for all combinations of channel conductivity k_c and sheet conductivity k_s. Channel discharge is overlaid in grey. (a) Run 1; (b) Run 2; (c) Run 3; (d) Run 4; (e) Run 5; (f) Run 6; (g) Run 7; (h) Run 8; (i) Run 9. See Table 2.3 for conductivities corresponding to each run.

the total channel discharge through all edges with at least one node on the grounding line, and subplot (b) depicts the maximum discharge through any one of these edges.

In general, water was discharged at a higher rate from Trinity Glacier than from Wykeham Glacier during each melt season. There is no one run in which total discharge was consistently greatest across each year nor between both glaciers. However, the maximum

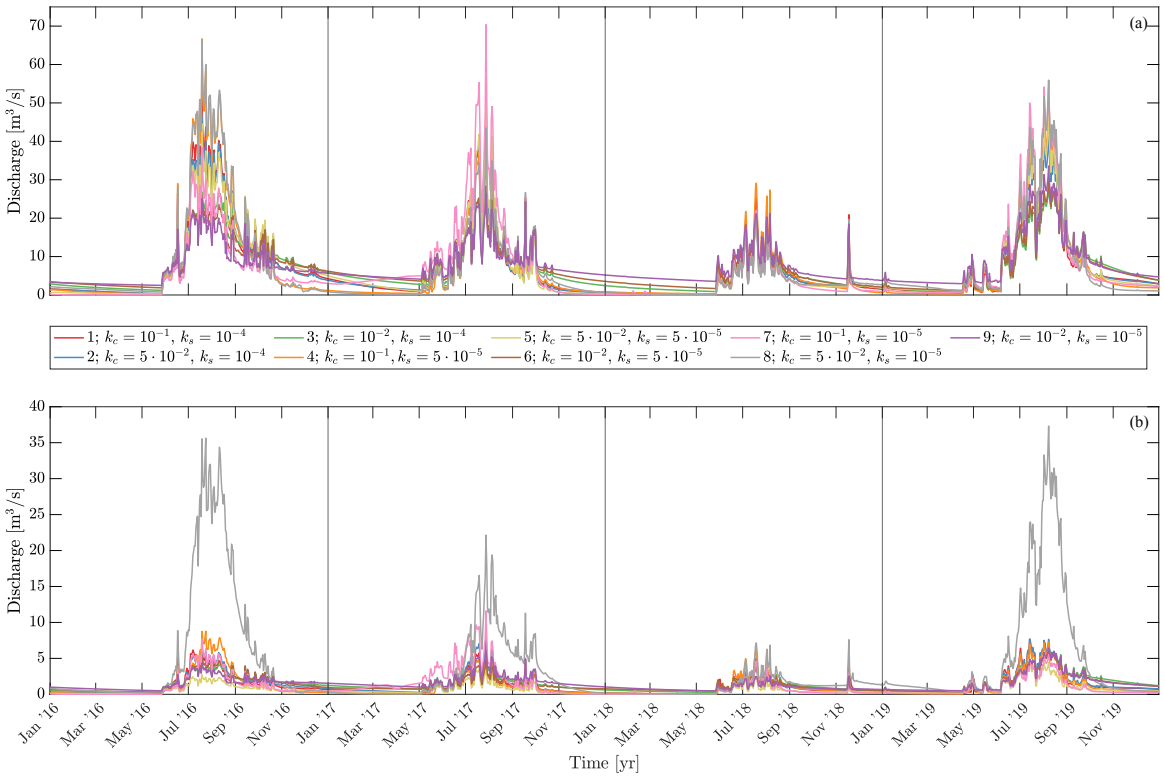

Figure 3.31: Maximum discharge through the grounding line of Trinity Glacier for 2016–2019 for all combinations of k_c and k_s, as listed in Table 2.3. (a) Total discharge through grounding line nodes; (b) maximum discharge through any one grounding line node.

discharge through any one channel remained the same at each respective glacier across each year during the peak melt season. In 2016, total grounding line discharge at Trinity-Wykeham Glaciers peaked on July 18, with Runs 4 and 8 reaching peaks of 66.7 m^3/s and 66.3 m^3/s respectively at the former, and Runs 1, 2, 4, 5, 7, and 8 (each with $k_c > 10^{-2}$ m$^{3/2}$ kg$^{-1/2}$) all exceeding 35.0 m^3/s at the latter. The greatest peak of 2016 at Trinity Glacier was $\sim$ 58% higher than that at Wykeham Glacier. The lowest peak in total discharge was more even between glaciers, with Run 9 at 25.1 m^3/s at Trinity Glacier and Run 3 at 26.8 m^3/s at Wykeham Glacier. Maximal single-channel discharge values covered a wide range at Trinity Glacier, where Run 8 reached 35.6 m^3/s through one grounding line channel on July 23. The next highest was during Run 4 at only 8.79 m^3/s. Wykeham

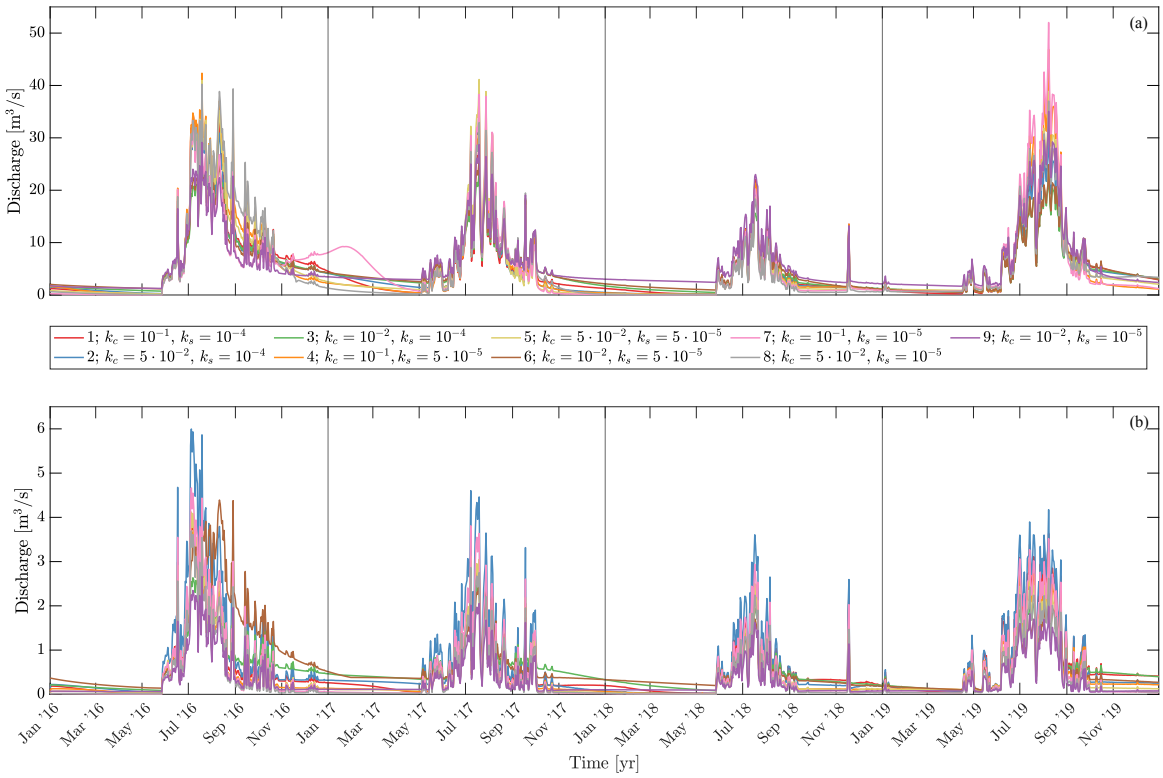

Figure 3.32: Maximum discharge through the grounding line of Wykeham Glacier from 2016–2019 for all combinations of k_c and k_s, as listed in Table 2.3. (a) Total discharge through grounding line nodes; (b) maximum discharge through any one grounding line node.

Glacier's maximum occurred in Run 2, in which a grounding line channel discharged 6.00 m^3/s on July 4, the maximum for that glacier throughout the simulation period at the glacier.

On July 27, 2017, Trinity Glacier discharged water at its maximal rate of 70.4 m^3/s during Run 7, the highest across the simulation period. Wykeham Glacier's 2017 peak occurred 9 days earlier in Run 5, with a discharge rate of 41.1 m^3/s. Runs 9 and 3 had the lowest peak total discharge rate at Trinity (26.4 m^3/s) and Wykeham (23.4 m^3/s) Glaciers respectively. Run 8 once again had the highest single-channel discharge during the Trinity Glacier melt season, reaching a maximum of 22.1 m^3/s on the same day as the peak in

total discharge, while 4.60 m^3/s was the maximum at Wykeham Glacier, attained twenty days prior on 17/07/2017.

Total grounding line discharge is lowest across both glaciers and all runs in 2018. As such, there was a smaller discrepancy between maximum single-channel discharge values across runs. The maximum total discharge across the grounding line at Trinity Glacier was 29.1 m^3/s during Run 4, only 4 m^3/s more than the 2016 minimum. Wykeham Glacier had a peak total discharge of 23.0 m^3/s in 2018 during Run 9, which was less than the lowest peak rate of the prior two years. Run 3 was minimal for both glaciers, with a maximum of 18.3 m^3/s on July 18 at Trinity Glacier and 15.6 m^3/s on July 17 at Wykeham Glacier. Trinity Glacier had a maximum of 7.59 m^3/s through its maximal channel during Run 8, which occurred late into the year on November 17 in response to a brief but substantial spike in meltwater production. Wykeham Glacier discharged its 2018 maximum of 3.05 m^3/s during Run 2.

Run 7 and Run 3 were the runs in which the greatest and least peak total discharge rates occurred respectively in 2019 for Wykeham Glacier. The glacier reached the greatest peak total discharge through the grounding line across the simulation at 52.0 m^3/s, and its lowest peak was less than half of that value at 24.0 m^3/s. Trinity Glacier peaked in Run 8 at 55.9 m^3/s, and had its lowest peak in Run 3 at 28.4 m^3/s, also approximately half of the maximum. Unlike previous years, both total grounding line discharge and single-channel discharge peaked in the late stages of the melt season on 08/07/2019 across all runs. Trinity Glacier reached its greatest single-channel discharge through the grounding line throughout the simulation at 37.3 m^3/s during Run 8, and Wykeham reached its 2019 maximum rate of 4.17 m^3/s during Run 2.

Chapter 4

Discussion

This chapter is centred around interpreting the outputs of modelling subglacial hydrology at Trinity-Wykeham Glaciers presented in Chapter 3 and discussing what these outputs imply about the glaciers and Arctic tidewater glaciers in general. Section 4.1 explores the main findings from the hydrology model runs. Subsection 4.1.1 examines general patterns that emerge in the model outputs from the baseline run, and how they compare to other studies. The effects of interannual variations in meltwater input and the conductivity parameters prescribed to the subglacial hydrological system are discussed in Subsections 4.1.2 and 4.1.3 respectively. Subsection 4.1.4 touches on the implications the results hold for the future of Trinity-Wykeham Glaciers and the wider CAA.

Section 4.2 considers the limitations faced in modelling the subglacial hydrology of Trinity-Wykeham Glaciers and work that can be done in the future to mitigate these limitations and build upon the results presented in this project. Limitations (Subsection 4.2.1) include those imposed by the model, those relating to the data used as inputs to the model, and those inherent to Trinity-Wykeham Glaciers and the modelling of glaciers in general. Subsection 4.2.2 discusses ways in which similar models can be improved. This includes not only advancements in the functionality of the model itself, but suggestions for future datasets that could serve to improve the accuracy, scope, and ease with which glacier models can simulate their real-world counterparts, particularly in the Canadian High Arctic.

4.1 Hydrology Trends

4.1.1 General Patterns and Comparisons with Existing Studies

Seasonal hydrology trends are evident in the model outputs at Trinity-Wykeham Glaciers between 2016 and 2019. These outputs are compared to other models of tidewater glaciers in the Arctic and data collected from Trinity-Wykeham Glaciers to determine whether they agree with previous work and what they might indicate about the influence of subglacial hydrology on the dynamics of the glaciers. Changes in subglacial water pressure can be associated with changes in velocity and subglacial drainage in outlet glaciers (Bartholomew et al., 2010; Iken and Bindschadler, 1986; Schoof, 2010). Figure 3.5 shows mean subglacial water pressure outputs across the domain in comparison to meltwater input between 2016 and 2019. The model outputs suggest that water pressures follow seasonal trends, mirroring the changes in meltwater production closely.

Pressures were relatively stable during the winter and early spring, with mean pre-melt season water pressures between 44.7% and 56.6%. During this time, new channels did not emerge at the bed of Trinity-Wykeham Glaciers, suggesting that frictional and geothermal heat alone did not generate enough meltwater to form channels. This is in line with various studies that point to supraglacial water as the primary driver behind the evolution of the subglacial hydrology network of Arctic and mountain glaciers (Bartholomew et al., 2010; Nienow et al., 1998). The "spring event" is a phenomenon in which the sudden influx of meltwater to a glacier's bed at the beginning of the melt season causes a sharp increase in subglacial water pressure and surface velocity when the subglacial system is largely distributed (Bartholomew et al., 2010; van de Wal et al., 2015). High subglacial water pressures are known to reduce friction at the bed and induce basal sliding, thereby causing accelerated flow rates (Benn and Evans, 2010). The spring event was reflected in the model outputs at Trinity-Wykeham Glaciers; the start of each melt season was marked by rapid pressurisation in the lower $\sim$ 30 km of each glacier. Trinity-Wykeham Glaciers are the only two glaciers in the QEI that currently flow at over 1 km/yr (Van Wychen et al., 2020b). Both glaciers reached their annual peak velocities in the spring and early summer months when water pressure outputs were highest (see Figures 3.15 to 3.20). The first channels began to form in May at the glaciers' termini as melting rates rose in the ablation zones. The upglacier expansion of channel networks from the terminus is generally accepted in theory and has been reproduced in previous subglacial hydrology models (Hewitt, 2011; Werder et al., 2013).

Figure 3.14 depicts the maximal range of the subglacial channel network during each year of the simulation, overlayed upon the basal topography. Channel distribution was

largely consistent across each year of the simulation. The network gradually grew in both length and cross-sectional area through the melt season (see Figures 2.5, 3.6), as also reported by Nienow et al. (1998) from dye tracing results at Arolla Glacier, Switzerland. In July when channels were most numerous, channels showed an average cross-sectional area between 5–13 m^2, corresponding to radii of 1.8–2.0 m, and the mode channel area at this time was 0.63–1.85 m^2, corresponding to radii of 0.63–1.09 m. Basal topography also influenced the location of major channels; these channels typically developed in overdeepened areas and diverted flow around areas of raised bedrock such as the prominent pinning point at the grounding line of Wykeham Glacier (see Figures 4.1 (a), (b), and (c) below). The channel networks at both glaciers were largely arborescent and interconnected, and most channels served as tributaries to one high-volume channel extending far upglacier. These channels intersected the grounding lines at $-7.221 \cdot 10^5$ m East and $-1.090 \cdot 10^6$ m North at Trinity Glacier and $-7.257 \cdot 10^5$ m East and $-1.096 \cdot 10^6$ m North at Wykeham Glacier in each year of every model run aside from those in which $k_c = 10^{-2}$ $m^{3/2}$ $kg^{-1/2}$. Total discharge through the grounding lines of Trinity-Wykeham Glaciers was both proportional to and synchronous with variations in meltwater input across all years (Figures 3.13 (a) and (b)). One notable difference between the two glaciers is that in all years other than 2016 (to be touched on in the following subsection), the maximum single-channel discharge over the grounding line of Trinity Glacier was typically more than double that at Wykeham Glacier, despite the total discharge being fairly even. The main channel of Trinity Glacier extended $\sim$ 25%–80% further upglacier and therefore drained a much larger portion of the bed than the main channel of Wykeham Glacier, explaining the discrepancy in discharge through these channels. The upglacier extension of the channel network was likely influenced by the basal topography. The bed of Wykeham Glacier has a prominent reverse slope which has been shown to impede channel formation as water is forced to flow uphill (Harcourt et al., 2019; Röthlisberger, 1972). The differences in channel discharge may also have been affected by the initial velocity of the glaciers. Trinity Glacier flowed 250–500 m/yr faster than Wykeham Glacier near the terminus (after the 800 m/yr limit imposed for the model), and over a much larger area. As per Equation 2.8, the cavity opening rate $w_s(h)$ is directly proportional to the sliding velocity u_b. This means that cavities open at a higher rate when sliding velocity is increased, thereby increasing the overall efficiency of the distributed system (Werder et al., 2013).

Irregular, short-term fluctuations in water pressure outputs occurred through the melt season with average diurnal fluctuations of $\sim$ 3%, but amplitudes frequently exceeding 10%. Subglacial water pressures can undergo periods of increase and decrease through the melt season in response to variations in meltwater production which, in the Queen Elizabeth Islands, are likely attributable to variations in air temperature and precipitation

(Millan et al., 2017; Sharp et al., 2011). Peak water pressure was reached in early July in the first three years of the simulation, and early August in 2019. Subglacial channels alleviated high pressures in the distributed system by drawing water from adjacent cavities and transporting it efficiently from the bed. Figures 3.2, 3.7, 3.9, and 3.11 confirm this, showing water pressures in the lowest regions of the glaciers significantly lower than at mid-elevation where melt rates were high but channels covered a smaller portion of the bed. As such, within 2–4 weeks of the spring event, summer water pressures were generally lowest at the grounding line. Pressures were reduced in the proximity of channels in proportion to the rate of discharge within the channel. Figure 4.1 depicts water pressure across a transect of Trinity Glacier at three locations in the lower elevation region, each subsequently closer to the grounding line from left to right. In Figures (a) and (b), it is evident that high-discharge channels coincided with local pressure minima, with a possible radius of effect of $\sim$ 350 m from a channel. Figure (c) shows a prominent pressure low, below 90% overburden up to 350 m East of the largest channel. The pattern is less clear here, though the greatest velocities (i.e., cavity opening rates) and discharge rates occurred near the grounding line, leaving room for variability in the pressures. It should be noted that low pressures also coincide with topographic lows. Beginning in July, water pressure outputs trended downward through the end of the melt season, and stabilised at winter values between the beginning of September and the beginning of October. There are two likely reasons for this downward trend. First, meltwater production also trended downward during this period. Secondly, the channel network was at its largest size at that time and therefore drained the greatest area of the bed.

The modelled subglacial water pressure and channelisation patterns during the melt season bear similarities to observations taken from borehole measurements of basal water pressure at tidewater glaciers in Canada and Greenland. Rada Giacaman and Schoof (2023) measured subglacial water pressure at a small (4.28 km^2) alpine glacier in Yukon, Canada using 157 borehole pressure sensors. Measurements showed a sharp rise in subglacial water pressure at the end of May, i.e., the beginning of the melt season, followed by short-term fluctuations and a downward trend that accelerated at the beginning of July. These measurements mirror melt season pressure outputs at Trinity-Wykeham Glaciers and follow the pattern of a distributed drainage system early in the melt season that transitions into efficient channelised drainage as the melt season progresses. The model outputs also agree somewhat with western Greenland borehole measurements by Wright et al. (2016) in terms of overall behaviour. Stable basal water pressures in the winter, a spring event, mid-melt season pressure fluctuations, and restabilisation between the start of September and the start of October were all observed. Some substantial differences can be seen between the two studies, however. In the work of Wright et al. (2016), borehole

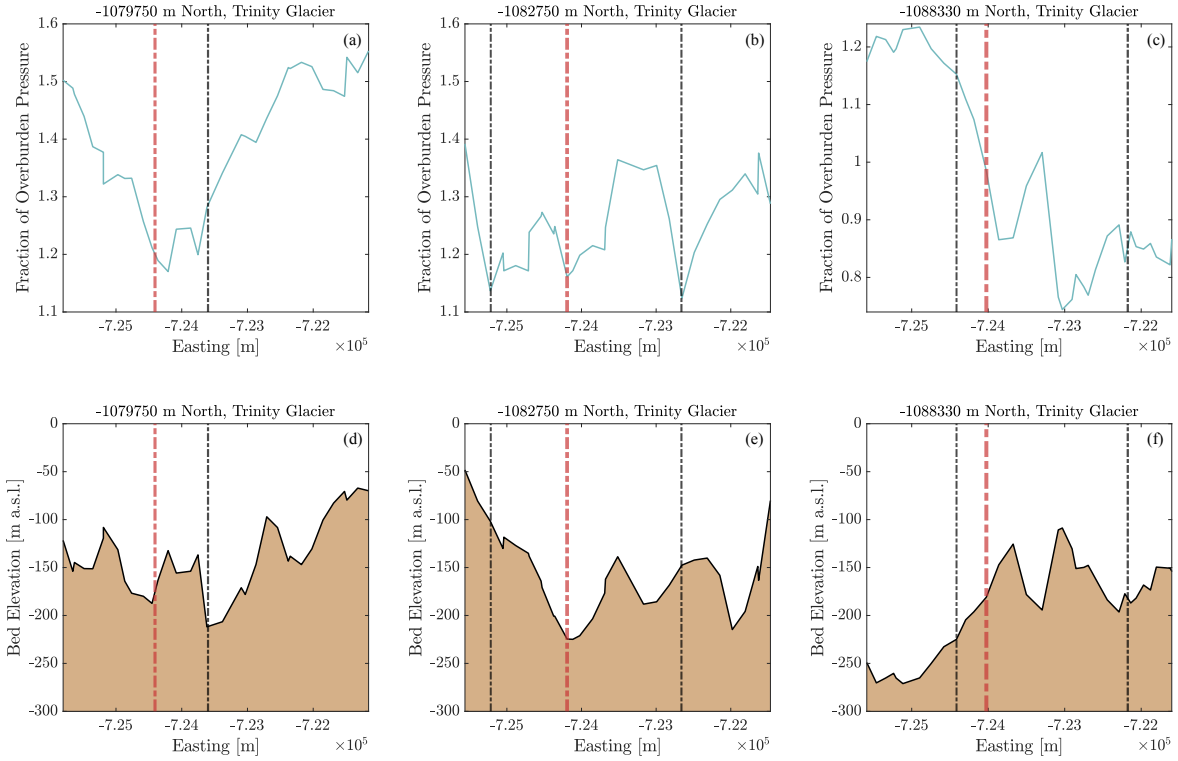

Figure 4.1: Top row: Ratio of basal water pressure to overburden pressure in the proximity of subglacial channels at Trinity Glacier on 27/07/2017, during the peak of the 2017 melt season. Pressure values are taken from nodes within 100 m of the listed transect. Bottom row: Bed elevation along the listed transect. (a) Pressure at -1079750 m North; (b) pressure at -1082750 m North; (c) pressure at -1088330 m North; (d) bed elevation at -1079750 m North; (e) bed elevation at -108275 m North; (f) bed elevation at -1088330 m North. Red lines represent the approximate location of the largest channel at a given transect, and black lines represent other channels at the transect with discharge rates exceeding 1 m^3/s. Line widths are scaled to the discharge rate of each channel.

pressure measurements taken 27 km inland from the terminus of Insunnguata Sermia during the winter months were considerably higher than the modelled subglacial water pressure outputs at Trinity-Wykeham Glaciers, in most cases 95–105% overburden. Additionally, the diurnal summer fluctuations typically saw pressures between 85–105% overburden, levels that were, more often than not, below those observed in winter. Fluctuations in mean

melt season pressures from the modelled Trinity-Wykeham outputs virtually never fell below winter values, and mid-elevation pressures (between ∼15–32 km up Trinity Glacier and ∼12–27 km up Wykeham Glacier) exceeded 120% of overburden on an average of 31 nonconsecutive days of the melt season each year, including 4 consecutive weeks from June 25 to July 23 and 42 days total in 2016. Ryser et al. (2014) and van de Wal et al. (2015) also reported high winter water pressures from borehole observations in the ablation zone of the western Greenland Ice Sheet. Ryser et al. (2014) drilled boreholes at two sites 26 km and 20 km downstream from Swiss Camp, West Greenland. They concluded from their measurements that subglacial drainage was inefficient year-round at the drill site nearest the margin where subglacial water pressures exceeded overburden pressure, and that the drill site further inland accessed an efficient drainage network that persisted through all seasons, characterised by water pressures below overburden year-round. van de Wal et al. (2015) measured basal water pressure in two boreholes 7 km from the western margin. These boreholes showed near identical patterns in pressures over five years, with gradually rising water pressures through the winter and a brief peak at the beginning of the melt season, followed by a rapid drop coincident with a sharp increase in velocity of up to 13%. From these results, van de Wal et al. (2015) concluded that their boreholes were drilled in the vicinity of an efficient network of channels at the glacial bed. It should be noted that high melt inputs have been observed to cause high subglacial water pressures even in the presence of extensive channelisation (Cook et al., 2020). One must keep in mind that in-situ data regarding subglacial hydrology, including subglacial water pressures, are quite limited. Possible causes and solutions regarding discrepancies in basal water pressure outputs are explored in Subsection 4.2.1.

Landsat 7, Landsat 8, and ASTER image pairs of Trinity-Wykeham Glaciers showed sharp decreases in velocity late in the melt season (Harcourt et al., 2019). This deceleration coincided with a drop in modelled basal water pressures seen each August (see Figures 3.2, 3.7, 3.9, 3.11 (c) and (d)). These simultaneous events reflect the efficient channelised system seen in the model at this time. Channels can efficiently drain water from the bed and reduce water pressure in their vicinity, creating a pressure gradient that permits the rapid evacuation of water from the terminus. Theory and observations at northern alpine glaciers suggest that a reduction in water pressure increases basal friction and reduces flow speeds (Andersen et al., 2010, 2011; Iken, 1981; Iken and Bindschadler, 1986; Stevens et al., 2022). Velocity trends indicate that the areas in which channelisation was most prominent in this simulation coincided with the areas of Trinity-Wykeham Glaciers that are most susceptible to short-term and seasonal velocity fluctuations—in agreement with observations in Southwest Greenland by Sole et al. (2013) and van de Wal et al. (2015)—and that the late-summer slowdown observed in most years was, in part, the product of

widespread channelisation (Harcourt et al., 2019; Van Wychen et al., 2020b).

Channels formed during the 2016 and 2018 melt seasons persisted into the spring of the following years. One should note that 2016 and 2018 were the years of greatest and least meltwater production respectively. The mid-elevation region is the area in which these winter channels—largely the main channels—discharged water at the greatest rates post-melt season. No channels persisted at high elevations, and discharge rates were comparatively minimal or nonexistent at lower elevations through the winter. Channels formed during the 2017 melt season disappeared by November 2017 despite higher rates of surface melt compared to 2018, likely due to ice creep. Considering Figure 3.5, it is likely that channel persistence is not strictly a function of total meltwater input, but one of water storage in the distributed system post-melt season. Model outputs suggest that channels were kept open through the winter by a constant supply of water accumulated in the distributed system during the melt seasons of 2016 and 2018, particularly in the mid-elevation regions of each glacier where mean sheet thickness was highest by a wide margin. This notion is supported by satellite observations in western Greenland which suggest that high rates of surface melt can result in extensive channelisation and slower post-melt season velocities due to persistent drainage of basal water (Davison et al., 2020; Sole et al., 2013; Sundal et al., 2011; van de Wal et al., 2008). Additionally, Bartholomaus et al. (2008) proposed that water input in excess of a channel network's capacity at a given time increases water pressure within the channels and forces water back into the distributed system. The excess of water in subglacial cavities in 2016 was likely the result of a rapid influx of meltwater that overwhelmed the efficient system, and once surface melting rates decreased, this water drained through the established channel network and allowed the channels to remain full into the following spring. Total meltwater production was roughly half of the four-year mean in 2018, so it is likely that meltwater could not be drained efficiently due to the limited formation of channels during the melt season and thus remained in the inefficient distributed system through the winter, sustaining those few channels.

4.1.2 Variations in Response to Meltwater Input Rates

Considering that melting rates were the only time-variant input to this model, one can conclude that any year-to-year differences observed in the hydrology of Trinity-Wykeham Glaciers were the direct result of changes in meltwater input. A stark contrast is evident in the hydrology outputs between years of high and low melt. In terms of meltwater production, only approximately half of the four-year mean ($1.47 \cdot 10^4$ m w.e./yr) was produced during 2018, making the year a clear outlier compared to the other three years. Patterns in winter water pressure, sheet thickness, channelisation and velocity show a

departure from the behaviour observed in the other years of higher melt, providing insight into how water at the bed can change the nature of a glacier's dynamics. Table 4.1 provides a summary of the subglacial hydrology outputs and surface velocities of Trinity-Wykeham Glaciers through the simulation period.

Table 4.1: Interannual variation in the subglacial hydrology outputs and surface velocities of Trinity-Wykeham Glaciers (2016–2019).

	2016	2017	2018	2019
Mean Melt Season Melting Rate (m w.e./day, Jun 1–Aug 31)	223.5	109.7	76.8	181.1
Channelization	Widespread	Widespread	Low Elevation	Widespread
Post-Melt Season Channels	Persist into Next Spring	Close by November	Persist into Next Spring	Persist Until End of Simulation
Melt Season Velocity	N/A	Slowest	Fast	Fastest
Mean Post-Melt Season Pressure at Mid-Elevation (Nov 1–Dec 31)	65.6% Overburden	57.9% Overburden	78.8% Overburden	67.2% Overburden
Mean Melt Season Sheet Thickness	0.338 m	0.107 m	0.164 m	0.197 m
Post-Melt Season Sheet Thickness	Exponential Decrease	Exponential Decrease	Linear Decrease	Exponential Decrease

Despite widely varying volumes of meltwater, patterns in melt season water pressure were similar in each year of the simulation, including 2018, with a difference of only 22.5% of overburden pressure between the highest (2016 at 91.6% overburden) and lowest (2017 at 69.1% overburden) mean melt season pressures (see Figure 3.5 (b)). The comparisons between subglacial water pressure and surface velocity at Trinity-Wykeham Glaciers in Subsection 3.1.3 are in line with prevailing theories regarding the transition between distributed and channelised drainage at tidewater glaciers as described in Subsection 1.1.2. Pressure and velocity patterns in 2016, 2017, and 2019 seem to exemplify this cycle, with climbing pressure and velocity through the melt season followed by drops in pressure and

deceleration once channelisation was widespread and melting rates had decreased. While the changes in velocity during 2017 clearly followed this pattern (Figures 3.18 to 3.20 (a)), the corresponding plots of fractional pressure change show very little change in pressure throughout the year (Figures 3.18 to 3.20 (d)). However, the dates used for comparison do not reflect the overall pattern of basal water pressure through the 2017 melt season. Pressures in each year underwent large fluctuations, alternating between short-term upward and downward trends that last between a couple of days and two weeks. These fluctuations saw mean pressures reach as high as 128% overburden and fall to near-winter levels, and the 2017 dates—dictated by the availability of velocity data—each happen to coincide with local pressure minima. Figure 4.2 shows these same comparisons for dates within one week of the velocity mosaics. While the dates are not aligned exactly, these comparisons better demonstrate the trend of elevated pressures that likely drove the acceleration of Trinity-Wykeham Glaciers in 2017. Percentage-wise, the simultaneous increases in pressure and velocity in 2019 were comparable to other years, with roughly a 50% increase in velocity overall. However, the post-melt season decrease in velocity was proportionally the largest compared to the pre-melt season velocity in 2019. One must consider that in April 2019, low and mid-elevations were at considerably higher pressures and velocities than in previous years—further evidence pointing to inefficient drainage throughout 2018. As such, this explains why even in this high-melt year, increases in pressure and velocity only appeared moderate compared to the already-elevated April values, and why the winter slowdown was proportionally much larger than in other years. High rates of melt and channelisation have been associated with slower post-melt season velocities in western Greenland (Davison et al., 2020; Sole et al., 2013; Sundal et al., 2011; van de Wal et al., 2008), and these factors were both observed in modelled and satellite-derived data respectively for Trinity-Wykeham Glaciers in 2019.

Subglacial water sheet thickness varied to a greater degree between years, as seen in Figure 3.5 (c). The greatest mean melt rates occurred during the 2016 and 2019 melt seasons, and this was reflected in the rapid and substantial increase in sheet thickness. This proportionality was broken in 2017; approximately 55% more water was input to the bed in 2017 than in 2018, but the maximum sheet thickness in 2017 was nearly 6 cm lower than in 2018. This may seem counterintuitive in a year when melting rates are higher. A potential explanation for this is that because of the higher rates of melt in 2017, channelisation was more widespread and channel discharge was greater (see Figures 3.14 and 3.13 (b) and (c)). Thus, water was drained too quickly from the distributed system into the channel network for substantial growth in the subglacial water sheet to occur.

There was minimal channelisation during 2018 (see Figure 3.14 (c)). The effects of this, and of the low meltwater input in general, were most evident post-melt season. As

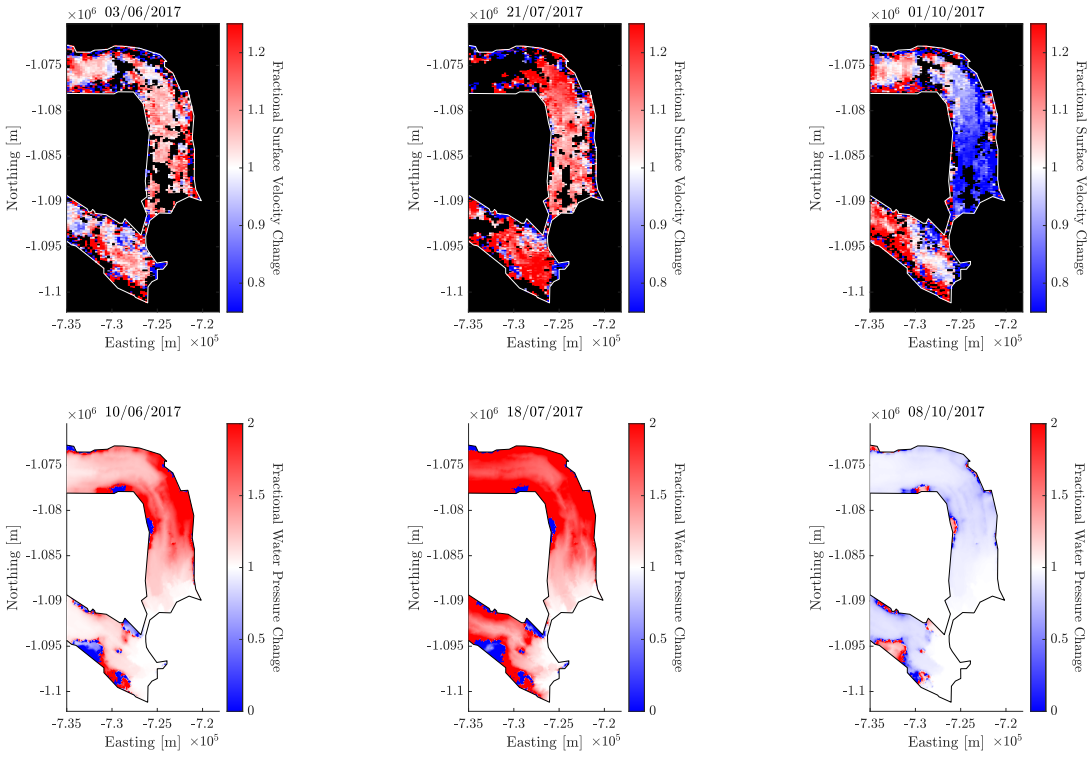

Figure 4.2: Top row: Fractional change in surface velocity from pre-melt season (as defined in 2.4) at Trinity-Wykeham Glaciers for 2017. Bottom row: Fractional change in basal water pressure from pre-melt season (as defined in 2.4) at Trinity-Wykeham Glaciers for 2017. (a) Change in surface velocity from the month of 04/2017 to 03/06/2017; (b) change in surface velocity from the month of 04/2018 to 21/07/2017; (c) change in surface velocity from the month of 04/2019 to 01/10/2017; (d) change in basal water pressure from 04/04/2017 to 10/06/2017; (e) change in basal water pressure from 04/04/2018 to 18/07/2017; (f) change in basal water pressure from 04/04/2019 to 08/10/2017.

seen in Figures 3.18 to 3.20 (e), 2018 had the highest percentwise increase in pressure throughout the melt season, and remained at elevated pressure once the melt season had ended. In particular, the mid- and high-elevation regions of Trinity-Wykeham Glaciers were at 20–30% higher water pressure after the 2018 melt season than before the season began.

Similarly, surface velocity did not decrease as drastically as in other years, remaining above 1 km/yr in lower elevation areas of Trinity Glacier. Van Wychen et al. (2020a) reported considerably higher velocities in the winter of 2018/2019 than in any other winter in the study period, especially when comparing the regions $\sim$ 18–30 km from the calving front. Elevated pressures and surface velocities are associated with large volumes of water in the distributed system, and this indicates that much of the water produced during the melt season was not efficiently transported to the grounding line and discharged. After reaching its maximal mean value during the 2016, 2017, and 2019 melt seasons, sheet thickness decayed along an approximately exponential curve in response to mean melting rates dropping below $\sim$ 50 m w.e./day. Sheet thickness continued to climb during this period in 2018, and did not begin to fall until melting rates were negligible. The water sheet drained at a comparatively slow and linear rate of $\sim$ 3–5 mm per week. This finding also supports the idea that efficient drainage never became the dominant mode of drainage in 2018. The velocity increase observed at the peak of the 2018 melt season (Figure 3.19 (b)) was the lowest of the three years considered, though this can be explained by the comparatively low amount of meltwater present at the bed to act as a lubricant.

Total discharge through the grounding lines of Trinity-Wykeham Glaciers was both proportional to and synchronous with variations in meltwater input across all years (Figures 3.13 (a) and (b)). Single-channel discharge rates, as seen in Figure 3.13 (c), similarly traced the meltwater input in 2017, 2018, and 2019, although Trinity Glacier discharged more than twice as much water as Wykeham Glacier did through a single channel. The year 2016 told a different story; while single-channel discharge at Wykeham Glacier was highest in 2016—as expected from the high melt rates—with a maximum discharge rate of 4.12 m^3/s, Trinity Glacier peaked at just 2.78 m^3/s. This can be attributed to the fact that in 2016, more subglacial channels formed at the grounding line of Trinity Glacier than in other years, and the total volume of water at the bed was divided between them (see Figure 3.14). At the peak, there were 9 separate conduits passing over the grounding line of Trinity Glacier in 2016, over half of which exceeded 2 m^3/s of discharge. Each other year showed a maximal number of 6 or 7 channels, with less than half of them exceeding discharge rates of 2 m^3/s. Discharge at the grounding line of Wykeham Glacier was split more evenly every year. Single-channel discharge rates at Trinity Glacier were highest in 2017 and 2019, which may have been a result of the persistence of the main channel through the preceding winter. Because this channel was fed through the winter, it could retain a greater cross-sectional area and therefore transport a greater volume of water once melting rates increased.

The outputs of the model runs in conjunction with surface velocity observations point to the conclusion that surface melt and subglacial hydrology directly influence the velocity

of Trinity-Wykeham Glaciers. The beds of Trinity-Wykeham Glaciers pressurise during the melt season due to the influx of meltwater. Friction between the bedrock and ice is reduced, resulting in basal sliding and accelerated velocities until excessive water and pressure lead to the formation of a channel network that drains water efficiently. Pressure, and in turn velocity, drop in the absence of the lubricating water, often to levels below the winter prior. When there is not enough water input to the bed during the melt season, efficient drainage does not become the primary mode of water evacuation from the bed. This can lead to elevated pressures, greater volumes of water in the distributed system, and comparatively high velocities post-melt season and into the following year (Iken and Bindschadler, 1986). It should be noted that frequent calving occurring at Trinity-Wykeham Glaciers may also be a determinant in the seasonal velocity patterns; glacier mass at the terminus can resist flow through basal and lateral friction (Carr et al., 2013a; Hill et al., 2018). Both glaciers discharge enormous amounts of ice into Talbot Inlet (Dalton et al., 2019; Van Wychen et al., 2016, 2020a) (see Subsection 4.1.4). The rates of calving are likely augmented by the extreme retreat and thinning of the glaciers' termini (Cook et al., 2019; Dalton et al., 2019; Millan et al., 2017; Van Wychen et al., 2020a). This loss of ice in the summer months may be contributing to the extreme speedup. Models that couple such ice dynamics with glacial hydrology would provide a more complete picture of the factors influencing the velocity of tidewater glaciers.

4.1.3 Sensitivity Analysis of Conductivity Parameters

Sheet conductivity k_s and channel conductivity k_c are parameters that are used to simplify and quantify important aspects of glacier hydrology—the rates at which subglacial water can travel through the distributed and channelised systems, respectively—for which direct measurement is not possible. The sensitivity tests in Section 3.2 were completed in order to examine the influence that these conductivities and their interactions have over the outputs of the GlaDS subglacial hydrology model, providing constraints on their values that can inform future modelling efforts.

When determining an ideal range of values for sheet and channel conductivities, one determining factor is how true-to-life the model outputs are when a given combination of conductivities is applied. The conductivities applied in each run are listed in Table 2.3. In-situ measurements by Walder and Hallet (1979) and Jansson et al. (1996) of subglacial cavities and bumps yielded heights between 0.1 and 1.5 m. Sheet thickness in Run 9 was often in excess of this range over large areas of the glacier beds. For example, 22.1% of the bed or approximately 107.5 km^2 was at thicknesses above 1.5 m on 28/06/2017, with a maximal thickness of 14.2 m. Subglacial topography can be highly variable, and

while topographic irregularities such as protrusions and depressions can theoretically create cavities of this size, this is relatively uncommon and the modelled sheet thickness outputs in Run 9 are clear outliers compared to other runs. As such, the combination of conductivities in Run 9 can be disregarded. Subglacial water pressures at alpine glaciers are often observed to approach overburden pressure during the winter months (Ryser et al., 2014; van de Wal et al., 2015; Wright et al., 2016). With this in mind, Runs 1, 2, and 4 can be eliminated based on the fact that each had mean water pressures below 50% on 19/04/2017 (see Figures 3.21 (b) and 3.27 (a), (b), and (d)). Run 7 can also be excluded due to the length of its main channel at Trinity Glacier. This channel extended over 40 km upglacier, well beyond the reach of any channel in the other runs. This large channel also decreased melt season water pressures too significantly to be considered a practical representation of real subglacial hydrological processes; Figure 3.24 (g) shows water pressures below overburden up to 25 km upglacier in the proximity of the channel. Run 8 can also be eliminated on the basis of channels; considering Figure 3.31 (b), it is evident that the single-channel discharge at Trinity Glacier during Run 8 was an outlier from the other runs, with melt season discharge rates 3–15 times those of other runs in every year but 2018. It should be noted that total channel discharge during Run 8, while frequently high, was much more in line with the outputs of other runs compared to the single-channel discharge. This implies that a large percentage of the water discharged over Trinity Glacier's grounding line was transported through one channel in Run 8. The assumption in GlaDS that the volume of a channel is 100% occupied by water at all times can lead to unrealistically high channel growth and discharge when numerical instabilities arise (Scholzen et al., 2021). With the other runs taken out of consideration, Runs 3, 5, and 6 remain with k_s between 10^{-4} and $5 \cdot 10^{-5}$ $\mathrm{m}^{7/4}$ $\mathrm{kg}^{-1/2}$ (moderate-to-high) and k_c between $5 \cdot 10^{-2}$ and 10^{-2} $\mathrm{m}^{3/2}$ $\mathrm{kg}^{-1/2}$ (low-to-moderate). Overall, these runs exhibited very similar outputs. This consistency between runs grants confidence in the validity of this range of values for k_s and k_c within the GlaDS model.

A number of tentative conclusions can be drawn from the sensitivity tests. Sheet conductivity has a strong control on water pressure; the three runs at the lowest k_s consistently exhibited the highest melt season pressures. Equation 2.5 shows that sheet discharge q is directly proportional to k_s. When water cannot be transported through the distributed system easily, i.e., when sheet discharge is low, water pressure builds up in the elements of the distributed system. Channel conductivity has a strong control over both sheet thickness and channel discharge. The three runs at lowest k_c had by far the highest sheet thicknesses throughout the simulation and, generally, the lowest melt season grounding line discharge, but also exhibited the highest pre- and post-melt season discharge. A possible explanation stems from the idea that lower channel conductivity implies a greater resistance to flow.

Analogous to the sheet conductivity equation, Equation 2.20 shows that channel discharge Q is directly proportional to k_c. As a consequence of the lower channel conductivity, the large quantities of meltwater produced during the summer months were not discharged as efficiently, as evident from the comparatively low discharge rates at that time (see Figures 3.31 and 3.32). However, once the melt season ended, much of the water expelled during the melt season in the other runs remained in the distributed system (see Figure 3.21 (c)) and continued to feed the channel network through the winter months. When k_c is high, water flows at a greater rate within the channels and melts their walls through frictional heat, thereby increasing the volume discharged through the channels—melted ice contributes to this volume, and channels in the GlaDS model are always assumed saturated. There is no clear trend between k_s and channel discharge; total channel discharge at the highest channel conductivity was typically 1–1.5 times that observed at intermediate channel conductivity, and 1.5–2.5 times that observed at the lowest channel conductivity, regardless of sheet conductivity. Years of greater melt showed a greater differentiation between discharge rates when comparing different values of k_c.

Channel conductivity also has an apparent influence on the arborescence of the channel networks. Broadly speaking, when k_c was high, there were fewer, longer channels with high rates of discharge (see Figures 3.29 (a), (d), and (g)). At the intermediate value of k_c, there were more small low-discharge channels acting as tributaries to the main one (see Figures 3.29 (b), (e), and (h)). When k_c was at its lowest, channels were numerous, but they were quite short, largely disjoint, and exhibited very low rates of discharge (see Figures 3.29 (c), (f), and (i)). Channel length may also be influenced by the combination of conductivities in that when k_c was high, decreasing k_s resulted in longer channels. This effect was weakened as k_c decreased.

Sheet and channel conductivity play a role in determining where water depth and pressure are high, and the spatial extent and arborescence of the channel system. Sheet conductivity values between 10^{-4} and $5 \cdot 10^{-5}$ $\mathrm{m}^{7/4}\ \mathrm{kg}^{-1/2}$ channel conductivity values between $5 \cdot 10^{-2}$ and 10^{-2} $\mathrm{m}^{3/2}\ \mathrm{kg}^{-1/2}$ produced outputs that best met the outlined criteria, and can be used as baselines for future modelling projects. We cannot conclude on specific values that perfectly emulate the beds of Trinity-Wykeham Glaciers, but this is a valuable test to show a potential range of values and their effects on the GLaDS model.

4.1.4 Future Implications

The seasonal and interannual hydrology trends observed at Trinity-Wykeham Glaciers present many questions regarding the future of both the glaciers and their surrounding

environment. Air temperatures are trending upward across the globe and Arctic regions are subject to the most rapid heating due to Arctic Amplification (Cohen et al., 2014; Mortimer and Sharp, 2018; Short and Gray, 2004). Summers in the QEI have become increasingly warmer since 2005, resulting in increased summer mean ice surface temperatures, longer melt seasons, and surface mass balances nearly five times more negative than the mean between 1963 and 2004 due to increased melting (see Figure 1.2) (Millan et al., 2017; Sharp et al., 2011). Figure 4.3 features a time series of surface mass balance components in the northern CAA which shows a clear upward trend in melt since the mid-nineties. Trinity-Wykeham Glaciers are the only glaciers on either Ellesmere Island or Axel Heiberg Island to have accelerated consistently since the turn of the century, and Trinity Glacier sped up by over 100% between 1999 and 2015 (Van Wychen et al., 2016), contemporaneously with the observed rise in surface melt. The results of this project suggest that subglacial water pressure and the formation of channelised subglacial drainage, two determining factors in glacial flow speeds, are highly dependent on meltwater input to the bed (Bartholomew et al., 2010; Iken and Bindschadler, 1986; Schoof, 2010).

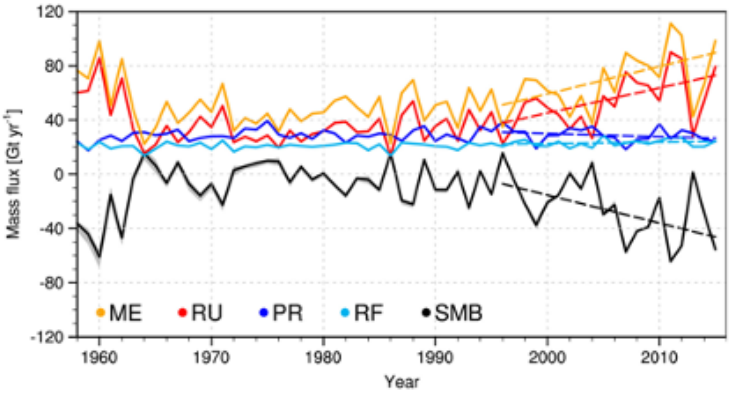

Figure 4.3: Time series of northern CAA and surface mass balance (SMB) components: melt (ME), runoff (RU), total precipitation (PR), and refreezing (RF). The grey envelopes correspond to the SMB uncertainty resulting from changing glaciers hypsometry in time, that is, due to glacier retreat and volume loss. Adapted from Noël et al. (2018).

Increased melt will undoubtedly influence dynamics at Trinity-Wykeham Glaciers, though the precise outcomes are difficult to predict. In the short term, the trend of elevated winter and early-melt season velocities is likely to continue with increased meltwater input. Extended and intensified melt seasons may hasten the formation of an efficient network of channels and cause the summer slowdown observed at the glaciers to occur earlier in the year (Harcourt et al., 2019). If melting rates continue to climb well into the future,

there are two possibilities. First, channelised drainage may persist further into the winter at Trinity-Wykeham Glaciers, resulting in lower velocities year-round. However, increased water input to the bed has the potential to overwhelm the channel network and induce faster basal sliding year-round, a phenomenon suggested to have already begun by Dalton et al. (2022) in light of reduced seasonal velocity variability in recent years and observations of accelerated motion affecting a larger portion of the glaciers' trunks. The persistence of channels through the winter and into the following spring as a result of particularly high (2016) or particularly low (2018) summer melting rates suggests that glacier velocities may become more uniform on a seasonal scale in coming years.

Mass balance and glacier retreat have exhibited a strong correlation in the CAA, with variations in retreat patterns closely following atmospheric warming trends (Cook et al., 2019). Elevated melting rates also impede the formation of sea ice at the glaciers' termini. Sea ice resists flow, reduces the frequency of iceberg calving events, and reflects solar radiation more effectively than ocean water (Cohen et al., 2014; Cook et al., 2019; Dalton et al., 2019). Between 2011 and 2014, Trinity-Wykeham Glaciers contributed $\sim$ 60% of the dynamic discharge from Ellesmere and Axel Heiberg Islands (Van Wychen et al., 2016). High velocities, rapid retreat, and the reduced presence of sea ice are all products of elevated air temperatures in the CAA, and they serve to explain the significant increase in dynamic discharge from the two glaciers (Dalton et al., 2019; Van Wychen et al., 2016, 2020b).

The CAA deviates from other polar regions in the fact that the rapid retreat and melting that have been observed are evidently driven by substantial atmospheric temperature rise, seemingly unaffected by the regional variations in ocean temperature that have caused extensive melt on neighbouring Greenland's coastlines (Cook et al., 2019; Rignot et al., 2010). This is particularly concerning given the rapid atmospheric warming seen in the Arctic in the quarter century. There are approximately 300 tidewater glaciers in the CAA, each subject to this rapid warming, and many are grounded below sea level for tens of kilometres upglacier (Cohen et al., 2014; Mortimer and Sharp, 2018; Van Wychen et al., 2020b). The dynamics of Trinity-Wykeham Glaciers are extraordinary in the greater context of the CAA, but the circumstances driving this behaviour—namely, high melt rates and overdeepened basal topography conducive to flotation—are not. Research suggests that the fronts of Trinity-Wykeham Glaciers have detached from their bases and begun partially floating (Harcourt et al., 2019; Van Wychen et al., 2020b). Other tidewater glaciers in the CAA may be susceptible to the same acceleration, thinning, and retreat seen at Trinity-Wykeham Glaciers, and will become more vulnerable as meltwater input continues to trend upward (Van Wychen et al., 2020b). The CAA holds enough ice to contribute 199$\pm$30 mm to sea level, and surface mass balance already accounts for 90% of mass

loss in the QEI (Cook et al., 2019; Millan et al., 2017). If the fronts of other QEI glaciers begin to float, as is suggested of Trinity-Wykeham Glaciers, a similar trend of dynamic thinning, extensive retreat, and ice discharge could spread and result in a region-wide increase in sea level contribution (Dalton et al., 2022; Harcourt et al., 2019; Van Wychen et al., 2020b). Were the striking rates of dynamic discharge seen at Trinity-Wykeham to become widespread in the CAA, an alarming number of icebergs could be released into Arctic waters. Important shipping routes such as the Northwest Passage pass through the CAA in the summer when icebergs are most common (Cook et al., 2019). Icebergs pose a serious threat to the occupants of sea vessels in the North, and an increased presence of icebergs could reduce the viability of routes used to provide vulnerable populations in the Canadian High Arctic, such as the Inuit, with food, supplies, and services. Overall, the exceptional behaviour of the QEI's Trinity-Wykeham Glaciers could prove to be an indication of the response that northern Canadian glaciers will have to climate change in years to come.

4.2 Limitations and Future Work

4.2.1 Model Limitations

One major disagreement between the presented model outputs and in-situ measurements is basal water pressure values. As noted in Subsection 4.1.1, modelled winter water pressures were noticeably low and melt season water pressures were noticeably high when compared to borehole measurements in a similar setting (Wright et al., 2016). This is a commonly cited issue with the GlaDS subglacial hydrology model (Flowers, 2015; Werder et al., 2013). Downs et al. (2018) investigated possible causes for the underpredicted winter water pressures in GlaDS and determined that a reduction in hydraulic conductivity in the distributed system is likely the root of the problem. Their suggested remedy to the low winter pressures is a seasonally variable sheet conductivity that changes in correspondence with the input of meltwater. However, this would be challenging to implement without masking interannual differences in drainage system evolution.

Sections of the glacier margins, particularly at Wykeham Glacier, exhibited erratic and extreme water pressures at times as low as $\sim -450\%$ overburden or as high as $\sim 450\%$ overburden, with no apparent pattern in timing. These areas were small and isolated, with steeply sloped bedrock typical of valley walls and ice typically less than 250 m thick. The GlaDS model struggles with these areas of steep topography, resulting in extreme pressures that in turn create steep pressure gradients that have the capacity to either

expel or draw large quantities of water depending on the direction of the gradient. The extreme pressure gradients exhibited here could have a domino effect on the hydrology of the glaciers, causing artificially high pressures across the domain. One such region was along the southern margin of Wykeham Glacier between $-7.26 \cdot 10^5$ m and $-7.35 \cdot 10^5$ m East. This area is of note because it was often the fastest-flowing area of Wykeham Glacier in 2017, 2018, and 2019. Even once Trinity Glacier and areas of Wykeham Glacier had undergone substantial post-melt season slowdown, velocities well above those prior to the melt season persisted in this highly-pressurised area on the southern margin (see Figures 3.20 (a), (b), and (c)), which could suggest that high water pressures like those produced by the model did occur in that region.

Excessive water pressures were not limited to fringe areas of the bed. While mean basal water pressures during the melt season ranged from 69.1% overburden in 2017 to 91.6% overburden in 2016, spikes as high as 120–140% overburden occurred every year, and in the mid-elevation regions of the glacier, mean pressures regularly approached 150% overburden. Pressures this high are unrealistic, as discussed in Subsection 4.1.1. There are a number of factors that may have caused these excessively high values. One such factor is the uniformity of channel and sheet conductivities. The GlaDS subglacial hydrology model assumes a hard bed composed of bedrock with conductivities unchanging across the domain, but subglacial till composed of a mixture of different-sized particles, including clay, silt, sand, gravel, and even larger rocks, is common. As such, water conductivity can vary substantially in different areas of the bed on a metre scale or smaller, and the uniform conductivities prescribed in the GlaDS model may not reflect the realities of Trinity-Wykeham Glaciers' beds (Dow, 2023). Low conductivities resist the flow of water and may result in artificially elevated water pressures. In GlaDS, water flow in the subglacial hydrological system is always assumed turbulent (Werder et al., 2013). However, it has been suggested that laminar flow may occur through the narrow orifices between the subglacial cavities of the distributed system, and some models aim to capture this (Hill et al., 2023; Sommers and Rajaram, 2020; Werder et al., 2013). Laminar flow is characterised by smooth, ordered motion with consistent velocities and streamlines. In the subglacial distributed system, laminar flow generally exhibits fewer velocity fluctuations compared to turbulent flow. As a result, water pressure variations associated with laminar flow in the distributed system may be less pronounced.

Model runs were initialised with a static velocity that stayed constant throughout the simulation period. This does not reflect the reality of Trinity-Wykeham Glaciers, which are known to flow at velocities that fluctuate by hundreds of metres per year within a single year (Harcourt et al., 2019). Additionally, the basal velocity used to initialise the model was capped at a maximum of 800 m/yr to ensure stability. This practice is commonplace

when using the GlaDS subglacial hydrology model (McArthur et al., 2023; Poinar et al., 2019). There is an area of $\sim$ 22 km^2 adjacent to the grounding line of Trinity Glacier that had its basal velocity reduced by up to 350 m/yr. In GlaDS ISSM, velocity only serves to affect cavity opening, when in reality velocities affect drainage, dynamics, glacier geometry, and the creation of surface features through which meltwater is conducted (Benn and Evans, 2010). The GlaDS model is largely designed for slow-moving valley glaciers, not fast tidewater glaciers. However, sensitivity testing by Poinar et al. (2019) showed that a cap on high-velocity areas had a negligible effect on subglacial hydrological outputs in Southeast Greenland when compared to runs in which velocity was not limited. Because dynamics are not coupled to the model, a time-invariant velocity was sufficient for the purposes of this project.

Another factor regarding velocities is the fact that the image pair velocity fields used in the pressure-velocity comparisons in Subsection 3.1.3 each used the WGS 84/UTM zone 15 N (EPSG:32615) coordinate system (Friedl et al., 2021). The mosaics were then converted to the WGS 84/NSIDC Sea Ice Polar Stereographic North (ESPG:3413) coordinate system, the system used in the April monthly velocity mosaics to which the image pair velocity fields are compared. Each mosaic had a spatial resolution of 200 m in its respective coordinate system, but converting to a different map projection changed the orientation of the mosaics' cells, stretching and compressing them to fit the new projection. The cells of the converted mosaics took on a new resolution of $\sim$ 13 m by $\sim$ 277 m. This could cause distortion in the mosaics, and introduce errors in the fractional change calculations. This limitation was unavoidable due to the limited availability of quality velocity mosaics for Trinity-Wykeham Glaciers.

4.2.2 Future Work

Many of the limitations faced in this project can be improved upon in future works. Errors and discrepancies in calculations involving CAA glacier velocities could be reduced if there were more velocity datasets readily available. Spatial coverage is often sparse, with many regions of missing data across the domain. The velocity-pressure comparisons in Subsection 3.1.3 had to be cropped to the lowest elevations of Trinity-Wykeham Glaciers due to the sparsity of data points upglacier. Temporal coverage is also limited; dates were chosen out of necessity for the velocity-pressure comparisons, and 2016 was eliminated entirely because the available velocity data was not sufficient to make these comparisons. A lack of quality velocity data limits the opportunity for analysis of seasonal velocity trends. In turn, predicting future behaviour is made more difficult, while rising rates of dynamic

discharge make such predictions increasingly important (Dalton et al., 2019; Millan et al., 2017; Van Wychen et al., 2016, 2020a).

Moulin maps are available for many glaciated regions of the world, including the Greenland Ice Sheet and Svalbard, Norway (e.g., Colgan and Steffen (2009); Pälli et al. (2003); Yang and Smith (2016)). Moulin maps help identify the locations and connectivity of moulins, allowing for more realistic and accurate simulations of water flow and drainage processes. Accurate representation of moulins is crucial for capturing the pathways and dynamics of subglacial water drainage, yet no moulin maps exist for much of the CAA. In-situ measurements of model input parameters and remote sensing of surface features and velocities at Trinity-Wykeham Glaciers and the CAA as a whole are critical in better understanding the future behaviour of tidewater glaciers in the region.

Some of the input parameters in the GlaDS subglacial hydrology model are not necessarily meant as realistic inputs that reproduce the real-life conditions of alpine glaciers, but more so as drivers that act together to pressurise or depressurise the subglacial system (Dow, 2023). Such parameters, such as sheet and channel conductivities or bedrock bump heights, are either impossible to accurately determine and emulate or serve as simplified representations of complex processes/phenomena beyond the scope of the models. In the latter case, such simplifications are often sufficient to extract meaningful results from a model. Sensitivity testing is key for parameters like these in order to better understand the effects they have on subglacial hydrological processes, and constrain their accepted values. Other model parameters, such as basal melting rates and the ice hardness constant, can be better understood and estimated through in-situ data collection and laboratory-based research.

Data acquisition via autonomous underwater vehicles (AUVs) can both be useful in characterising subglacial discharge. AUVs can be deployed near the glacier terminus and map the locations and characteristics of channel outflows where subglacial water is discharged into the ocean (Fried et al., 2015; Howe et al., 2019; Jackson et al., 2017). By capturing detailed bathymetric data and imagery, AUVs contribute to understanding the spatial patterns and evolution of subglacial channels and their interaction with the marine environment, along with other aspects of glacier dynamics. These data can also be used as inputs to glacier and plume models, which can be used to conduct sensitivity analyses, exploring how various factors, such as subglacial discharge rate, oceanic conditions, and channel geometry, influence dynamics (Cook et al., 2022; Jackson et al., 2017). Trinity-Wykeham Glaciers discharge water into Talbot Inlet, a wide, relatively accessible fjord. Both of these endeavours should be possible in this setting and could yield vital results for understanding subglacial hydrology in the region.

Finally, glacier hydrology and dynamics are not coupled in this project. This is the next logical step in predicting the future behaviour of tidewater glaciers in the CAA, as the two systems are so closely linked. Coupling between the subglacial hydrology of GlaDs and the dynamics of ISSM is currently in the works (Ehrenfeucht et al., 2023). Computationally, this coupling is extremely expensive. Nonetheless, steps are being taken toward refining our collective approach to the relationship between hydrology and dynamics, and what implications they may hold for the future.

Chapter 5

Conclusion

The GlaDS subglacial hydrology model was used to simulate subglacial processes at Trinity-Wykeham Glaciers. These two tidewater glaciers continue to exhibit dynamic activity of a magnitude unlike any other glaciers in the Canadian Arctic Archipelago (Cook et al., 2019; Van Wychen et al., 2016, 2020b). Radar-derived, satellite-derived, and model-derived datasets were used as inputs to the model, including basal and surface topography, surface velocities, and daily ice surface runoff products for 2016–2019. The model produced outputs of subglacial water sheet thickness, water pressure, and channel discharge in high resolution both temporally and spatially on a uniform, unstructured, triangular mesh representation of the glaciers. This study was designed with the following goals in mind:

- implement coupled two-dimensional distributed and channelized subglacial hydrology in the context of the Candian High Arctic;
- compare temporal and spatial patterns in distributed and channelized subglacial hydrology outputs to satellite-derived velocity data to explore how subglacial hydrological processes may be influencing the dynamics of Trinity-Wykeham Glaciers;
- determine a practical range of values for sheet and channel conductivities appropriate for future applications of the GlaDS model.

Nine model runs were completed with a duration of four years, from January 1, 2016, to December 31, 2019, each with a different combination of sheet conductivity, k_s, and channel conductivity, k_c. These model parameters dictate the ease with which water moves at the glacial bed. These nine runs were completed to test the sensitivity of the GlaDS model to

variations in k_s and k_c and how these changes manifest themselves in the hydrology outputs. See Table 2.3 for a complete list of model runs and corresponding conductivity parameters. Sheet conductivity was shown to have a significant negative relationship with basal water pressures, whereas decreased channel conductivity consistently resulted in elevated water sheet thicknesses and lower rates of discharge through channels at the grounding line, with years of higher meltwater production seeing a wider gap in discharge rates between runs. Lower channel conductivities also increased arborescence in the channel networks, whereas higher channel conductivities resulted in fewer channels of greater length and discharge. Sheet conductivity values of 10^{-4} and $5 \cdot 10^{-5}$ $m^{7/4}$ $kg^{-1/2}$ and channel conductivity values of $5 \cdot 10^{-2}$ and 10^{-2} $m^{3/2}$ $kg^{-1/2}$ were identified as the most reasonable based on the realism of the outputs of the associated model runs. These conductivities can serve as benchmarks for future subglacial hydrology models.

Run 5 with $k_s = 5 \cdot 10^{-5}$ $m^{7/4}$ $kg^{-1/2}$ and $k_c = 5 \cdot 10^{-2}$ $m^{3/2}$ $kg^{-1/2}$ was chosen for the main analysis. The years 2016, 2017, and 2019 each displayed a transition from inefficient distributed drainage to efficient channelised drainage in the lower 25–30 km of Trinity Glacier and 10–20 km of Wykeham Glacier in response to increased surface melting rates. These results generally agreed with satellite-derived surface velocity data at Trinity-Wykeham Glaciers, which showed accelerated flow in the early melt season followed by a dramatic drop in flow rate in the late melt season, coincident with decreased rates of melt and widespread channelized drainage. Across all four years, channels consistently formed along the same paths and at the same points along the grounding lines of both glaciers, indicating that the development of the channel network was strongly influenced by the geometry of the glaciers' beds and their surface slopes. These channels reduced water pressures locally; this was most evident near the glaciers' termini where channels were most abundant and water pressures were lowest throughout the melt season. Channels were found to persist into the following spring when the melt season was either particularly intense (2016) or particularly mild (2018). These channels persisted due to an overwhelmed channel network in the former case, and an underdeveloped channel network in the latter case. Melting rates were exceptionally high and exceptionally low in 2016 and 2018 respectively. Many channels formed during the 2016 melt season, but the meltwater was added to the bed faster than it could be discharged from the terminus and therefore spread into the distributed system. Channelisation was limited in the 2018 melt season due to low rates of surface melt. Both scenarios resulted in an excess of water stored at the bed in the mid-elevation area of the glaciers which fed the channels in the absence of surface melt. Subglacial water pressures also remained high after the 2018 melt season. Satellite data indicate comparatively high surface velocities after the peak of the 2018 melt season, in agreement with the theory that channelized drainage was underdeveloped that

year. These results indicate that outlet glaciers could see increased velocities and rates of outflow during the winter after exceptionally warm or exceptionally cold melt seasons. These findings provide valuable information about the possible mechanisms behind the formation and maintenance of perrenial subglacial channels; relatively little is known on this subject, so the results presented here are not just revealing for temperate glaciers in the CAA, but potentially for any temperate glacier exhibiting seasonally variable rates of flow.

Seasonal patterns in the water pressure outputs generally agreed with borehole measurements at multiple other Arctic tidewater glaciers, although the model tended to underestimate winter pressures and overestimate melt season pressures compared to observations. This demonstrates the importance of realistically representing the transport of meltwater from the supraglacial hydrology system to the bed within a glacier hydrology model. In response to surface melting, subglacial water pressures rapidly increased and underwent fluctuations throughout the melt season. Mean subglacial water sheet thickness monotonically increased at a more gradual rate and decreased exponentially when surface melt ceased. Overall, the agreement between hydrology outputs and surface velocity observations suggests the dynamics of Trinity-Wykeham Glaciers are in part the result of variable rates of surface melt and the configuration of the subglacial hydrology network.

Rising air temperatures observed in the Arctic will result in elevated rates of surface melt in the years to come (Cohen et al., 2014; Mortimer and Sharp, 2018; Short and Gray, 2004). Increased surface melt has the potential to cause the observed late-summer deceleration event to occur earlier in the year and bring about year-round channelised drainage (Harcourt et al., 2019). A perennial channelised system could reduce the seasonal variability and overall magnitude of glacier velocities by reducing water pressures at the bed at all times of year. Conversely, sufficiently high melting rates could surpass the capacity of the subglacial system and drive faster basal sliding, also reducing seasonal variability (Dalton et al., 2022). Belcher and Sydkap Glaciers, outlet glaciers on Devon and Ellesmere Islands repectively, have undergone consistent interannual acceleration near their termini since the mid 2010s that mirrors the dynamics of Trinity-Wykeham Glaciers (Van Wychen et al., 2020a). These changes in dynamics originated near the grounding lines and propogated upglacier over subsequent years. The acceleration has been attributed to changing oceanic and/or atmospheric conditions and, in the case of Belcher Glacier, dynamic thinning stemming from these environmental changes (Van Wychen et al., 2020a); dynamic thinning is also cited as a primary cause of Trinity-Wykeham Glaciers' changes in dynamics (Harcourt et al., 2019; Van Wychen et al., 2016, 2020a). Van Wychen et al. (2020a) suggest that the Belcher Glacier may be subject to further instability and speedup, largely due to the fact that it is grounded below sea level up to $\sim$ 20 km upglacier—yet another commonality

with Trinity-Wykeham Glaciers. Overdeepenings leave glaciers susceptible to rapid retreat, dynamic thinning, increased iceberg calving events, and acceleration (Cook et al., 2019; Van Wychen et al., 2016, 2020b). While Belcher and Sydkap Glaciers are considerably smaller than Trinity-Wykeham Glaciers and currently flow at slower rates (Van Wychen et al., 2020a), they have the potential to continue in their acceleration and contribute substantially to global sea level rise; Trinity-Wykeham Glaciers may serve as a forewarning of the future facing other glaciers of the Canadian Arctic.

Some notable limitations were identified in this project. The instantaneous delivery of meltwater from the surface to the bed likely caused artificially high subglacial melt season water pressures. A lack of time-variable velocities also reduced the realism of the simulation, especially in the context of Trinity-Wykeham Glaciers which exhibit high seasonal velocity variability. Moulin mapping, increased temporal and spatial coverage of velocity mapping in the Arctic, and two-way coupled hydrology and dynamics were all highlighted as ventures that could improve the accuracy and quality of forthcoming modelling projects. This project marks the first use of coupled two-dimensional distributed and channelized subglacial hydrology in the Candian High Arctic. The GlaDS model successfully captured a viable representation of subglacial drainage at Trinity-Wykeham Glaciers. The findings presented here provide insight into the subglacial processes of tidewater glaciers and will help future researchers to more reliably predict the response of tidewater glaciers to the rapidly warming Arctic climate.

References

Adams, P. and Dunbar, M. J. Arctic Archipelago, Mar 2006.

Alley, R. B. Water-pressure coupling of sliding and bed deformation: I. Water system. *Journal of Glaciology*, 35(119):108–118, 1989. doi: 10.3189/002214389793701527.

Alley, R. B. Towards a hydrological model for computerized ice-sheet simulations. *Hydrological Processes*, 10(4):649–660, 1996. doi: 10.1002/(SICI)1099-1085(199604)10:4⟨649::AID-HYP397⟩3.0.CO;2-1.

Alley, R. B., Lawson, D. E., Larson, G. J., Evenson, E. B., and Baker, G. S. Stabilizing feedbacks in glacier-bed erosion. *Nature*, 424(6950):758–760, Aug 2003. doi: 10.1038/nature01839.

Andersen, M. L., Larsen, T. B., Nettles, M., Elosegui, P., van As, D., Hamilton, G. S., Stearns, L. A., Davis, J. L., Ahlstrøm, A. P., de Juan, J., Ekström, G., Stenseng, L., Khan, S. A., Forsberg, R., and Dahl-Jensen, D. Spatial and temporal melt variability at Helheim Glacier, East Greenland, and its effect on ice dynamics. *Journal of Geophysical Research: Earth Surface*, 115(F4), 2010. doi: 10.1029/2010JF001760.

Andersen, M., Nettles, M., Elosegui, P., Larsen, T., Hamilton, G., and Stearns, L. Quantitative estimates of velocity sensitivity to surface melt variations at a large Greenland outlet glacier. *Journal of Glaciology*, 57(204):609–620, 2011. doi: 10.3189/002214311797409785.

Anderson, R. S. Strong feedbacks between hydrology and sliding of a small alpine glacier. *Journal of Geophysical Research*, 109(F3), 2004. doi: 10.1029/2004jf000120.

Arnold, N. and Sharp, M. Influence of glacier hydrology on the dynamics of a large Quaternary ice sheet. *Journal of Quaternary Science*, 7(2):109–124, 1992. doi: 10.1002/jqs.3390070204.

Arnold, N., Richards, K., Willis, I., and Sharp, M. Initial results from a distributed, physically based model of glacier hydrology. *Hydrological Processes*, 12(2):191–219. doi: 10.1002/(SICI)1099-1085(199802)12:2⟨191::AIDHYP571⟩3.0.CO;2-C.

Banwell, A. F., Caballero, M., Arnold, N. S., Glasser, N. F., Mac Cathles, L., and MacAyeal, D. R. Supraglacial lakes on the Larsen B ice shelf, Antarctica, and at Paakitsoq, West Greenland: a comparative study. *Annals of Glaciology*, 55(66):1–8, 2014. doi: 10.3189/2014AoG66A049.

Banwell, A. F., Wever, N., Dunmire, D., and Picard, G. Quantifying Antarctic-wide ice-shelf surface melt volume using microwave and firn model data: 1980 to 2021. *Geophysical Research Letters*, 50(12):e2023GL102744, 2023. doi: 10.1029/2023GL102744.

Bartholomaus, T. C., Anderson, R. S., and Anderson, S. P. Response of glacier basal motion to transient water storage. *Nature Geoscience*, 1(1):33–37, jan 2008. doi: 10.1038/ngeo.2007.52.

Bartholomew, I., Nienow, P., Mair, D., Hubbard, A., King, M. A., and Sole, A. Seasonal evolution of subglacial drainage and acceleration in a Greenland outlet glacier. *Nature Geoscience*, 3(6):408–411, May 2010. doi: 10.1038/ngeo863.

Benn, D. I. and Evans, D. J. A. *Glaciers & Glaciation*. Routledge, 2nd edition, 2010. ISBN 978 0 340 905791.

Bingham, R. G., Nienow, P. W., Sharp, M. J., and Boon, S. Subglacial drainage processes at a High Arctic polythermal valley glacier. *Journal of Glaciology*, 51(172):15–24, 2005. doi: 10.3189/172756505781829520.

Bingham, R. G., Nienow, P. W., Sharp, M. J., and Copland, L. Hydrology and dynamics of a polythermal (mostly cold) High Arctic glacier. *Earth Surface Processes and Landforms*, 31(12):1463–1479, 2006. doi: 10.1002/esp.1374.

Carr, J. R., Stokes, C. R., and Vieli, A. Recent progress in understanding marine-terminating Arctic outlet glacier response to climatic and oceanic forcing. *Progress in Physical Geography: Earth and Environment*, 37(4):436–467, Apr 2013a. doi: 10.1177/0309133313483163.

Carr, J. R., Vieli, A., and Stokes, C. Influence of sea ice decline, atmospheric warming, and glacier width on marine-terminating outlet glacier behavior in northwest Greenland at seasonal to interannual timescales. *Journal of Geophysical Research: Earth Surface*, 118(3):1210–1226, 2013b. doi: 10.1002/jgrf.20088.

Carroll, D., Sutherland, D. A., Shroyer, E. L., Nash, J. D., Catania, G. A., and Stearns, L. A. Modeling turbulent subglacial meltwater plumes: Implications for fjord-scale buoyancy-driven circulation. *Journal of Physical Oceanography*, 45(8):2169–2185, 2015. doi: 10.1175/JPO-D-15-0033.1.

Chu, W., Schroeder, D. M., and Siegfried, M. R. Retrieval of englacial firn aquifer thickness from ice-penetrating radar sounding in southeastern Greenland. *Geophysical Research Letters*, 45(21):11,770–11,778, 2018. doi: 10.1029/2018GL079751.

Clason, C. C., Mair, D. W. F., Nienow, P. W., Bartholomew, I. D., Sole, A., Palmer, S., and Schwanghart, W. Modelling the transfer of supraglacial meltwater to the bed of Leverett Glacier, Southwest Greenland. *The Cryosphere*, 9(1):123–138, 2015. doi: 10.5194/tc-9-123-2015.

Clason, C., Mair, D. W., Burgess, D. O., and Nienow, P. W. Modelling the delivery of supraglacial meltwater to the ice/bed interface: application to Southwest Devon Ice Cap, Nunavut, Canada. *Journal of Glaciology*, 58(208):361–374, 2012. doi: 10.3189/2012JoG11J129.

Cohen, J., Screen, J. A., Furtado, J. C., Barlow, M., Whittleston, D., Coumou, D., Francis, J., Dethloff, K., Entekhabi, D., Overland, J., and Jones, J. Recent Arctic amplification and extreme mid-latitude weather. *Nature Geoscience*, 7(9):627–637, Aug 2014. doi: 10.1038/ngeo2234.

Colgan, W. and Steffen, K. Modelling the spatial distribution of moulins near Jakobshavn, Greenland. *IOP Conference Series: Earth and Environmental Science*, 6(1):012022, Jan 2009. doi: 10.1088/1755-1307/6/1/012022.

Collins, D. Water storage in an alpine glacier. *International Association of Hydrological Sciences Publication*, 138:113–122, Jan 1982.

Cook, A. J., Copland, L., Noël, B. P. Y., Stokes, C. R., Bentley, M. J., Sharp, M. J., Bingham, R. G., and van den Broeke, M. R. Atmospheric forcing of rapid marine-terminating glacier retreat in the Canadian Arctic Archipelago. *Science Advances*, 5(3), Mar 2019. doi: 10.1126/sciadv.aau8507.

Cook, S. J., Christoffersen, P., Todd, J., Slater, D., and Chauché, N. Coupled modelling of subglacial hydrology and calving-front melting at Store Glacier, West Greenland. *The Cryosphere*, 14(3):905–924, 2020. doi: 10.5194/tc-14-905-2020.

Cook, S. J., Christoffersen, P., and Todd, J. A fully-coupled 3d model of a large Greenlandic outlet glacier with evolving subglacial hydrology, frontal plume melting and calving. *Journal of Glaciology*, 68(269):486–502, 2022. doi: 10.1017/jog.2021.109.

Copland, L., Sharp, M. J., and Nienow, P. W. Links between short-term velocity variations and the subglacial hydrology of a predominantly cold polythermal glacier. *Journal of Glaciology*, 49(166):337–348, 2003. doi: 10.3189/172756503781830656.

Courant, R., Friedrichs, K., and Lewy, H. Über die partiellen differenzengleichungen der mathematischen physik. *Mathematische Annalen*, 100(1):32–74, Dec 1928. doi: 10.1007/bf01448839.

Dalton, A., Copland, L., Tivy, A., Van Wychen, W., and Cook, A. Iceberg production and characteristics around the Prince of Wales Icefield, Ellesmere Island, 1997-2015. *Arctic, Antarctic, and Alpine Research*, 51(1):412–427, Jan 2019. doi: 10.1080/15230430.2019.1634442.

Dalton, A., Van Wychen, W., Copland, L., Gray, L., and Burgess, D. Seasonal and multi-year flow variability on the Prince of Wales Icefield, Ellesmere Island: 2009–2019. *Journal of Geophysical Research: Earth Surface*, 127(4), Apr 2022. doi: 10.1029/2021jf006501.

Davison, B. J., Sole, A. J., Cowton, T. R., Lea, J. M., Slater, D. A., Fahrner, D., and Nienow, P. W. Subglacial drainage evolution modulates seasonal ice flow variability of three tidewater glaciers in Southwest Greenland. *Journal of Geophysical Research: Earth Surface*, 125(9):e2019JF005492, 2020. doi: 10.1029/2019JF005492.

Dow, C. F., Werder, M. A., Babonis, G., Nowicki, S., Walker, R. T., Csatho, B., and Morlighem, M. Dynamics of active subglacial lakes in Recovery Ice Stream. *Journal of Geophysical Research: Earth Surface*, 123(4):837–850, 2018. doi: 10.1002/2017JF004409.

Dow, C., McCormack, F., Young, D., Greenbaum, J., Roberts, J., and Blankenship, D. Totten Glacier subglacial hydrology determined from geophysics and modeling. *Earth and Planetary Science Letters*, 531:115961, 2020. doi: 10.1016/j.epsl.2019.115961.

Dow, C. F. The role of subglacial hydrology in Antarctic Ice Sheet dynamics and stability: a modelling perspective. *Annals of Glaciology*, page 1–6, Mar 2023. doi: 10.1017/aog.2023.9.

Downs, J. Z., Johnson, J. V., Harper, J. T., Meierbachtol, T., and Werder, M. A. Dynamic hydraulic conductivity reconciles mismatch between modeled and observed winter subglacial water pressure. *Journal of Geophysical Research: Earth Surface*, 123(4):818–836, Apr 2018. doi: 10.1002/2017jf004522.

Echelmeyer, K. A., Clarke, T. S., and Harrison, W. D. Surficial glaciology of Jakobshavn Isbræ, West Greenland: Part I. surface morphology. *Journal of Glaciology*, 37:368 – 382, 1991. doi: 10.3189/S0022143000005803.

Ehrenfeucht, S., Morlighem, M., Rignot, E., Dow, C. F., and Mouginot, J. Seasonal acceleration of Petermann Glacier, Greenland, from changes in subglacial hydrology. *Geophysical Research Letters*, 50(1):e2022GL098009, 2023. doi: 10.1029/2022GL098009.

Flowers, G. E. Modelling water flow under glaciers and ice sheets. *Proceedings of the Royal Society A: Mathematical, Physical and Engineering Sciences*, 471(2176):20140907, 2015. doi: 10.1098/rspa.2014.0907.

Flowers, G. E. and Clarke, G. K. C. A multicomponent coupled model of glacier hydrology 1. theory and synthetic examples. *Journal of Geophysical Research: Solid Earth*, 107 (B11):ECV 9–1–ECV 9–17, 2002. doi: 10.1029/2001JB001122.

Forster, R. R., Box, J. E., van den Broeke, M. R., Miège, C., Burgess, E. W., van Angelen, J. H., Lenaerts, J. T. M., Koenig, L. S., Paden, J., Lewis, C., Gogineni, S. P., Leuschen, C., and McConnell, J. R. Extensive liquid meltwater storage in firn within the Greenland Ice Sheet. *Nature Geoscience*, 7(2):95–98, Dec 2013. doi: 10.1038/ngeo2043.

Fountain, A. G. and Tangborn, W. V. The effect of glaciers on streamflow variations. *Water Resources Research*, 21(4):579–586, 1985. doi: 10.1029/WR021i004p00579.

Fountain, A. G. and Walder, J. S. Water flow through temperate glaciers. *Reviews of Geophysics*, 36, Aug 1998. doi: 10.1029/97RG03579.

Fried, M. J., Catania, G. A., Bartholomaus, T. C., Duncan, D., Davis, M., Stearns, L. A., Nash, J., Shroyer, E., and Sutherland, D. Distributed subglacial discharge drives significant submarine melt at a Greenland tidewater glacier. *Geophysical Research Letters*, 42 (21):9328–9336, 2015. doi: 10.1002/2015GL065806.

Friedl, P., Seehaus, T., and Braun, M. Global time series and temporal mosaics of glacier surface velocities derived from Sentinel-1 data. *Earth System Science Data*, 13(10): 4653–4675, Oct 2021. doi: 10.5194/essd-13-4653-2021.

Gagliardini, O., Zwinger, T., Gillet-Chaulet, F., Durand, G., Favier, L., de Fleurian, B., Greve, R., Malinen, M., Martín, C., Råback, P., Ruokolainen, J., Sacchettini, M., Schäfer, M., Seddik, H., and Thies, J. Capabilities and performance of Elmer/Ice, a new-generation ice sheet model. *Geoscientific Model Development*, 6(4):1299–1318, 2013. doi: 10.5194/gmd-6-1299-2013.

Gardner, A. S., Fahnestock, M., and Scambos, T. MEaSUREs ITS_LIVE Regional Glacier and Ice Sheet Surface Velocities, Version 1, 2022.

Gardner, A. S., Moholdt, G., Scambos, T., Fahnstock, M., Ligtenberg, S., van den Broeke, M., and Nilsson, J. Increased West Antarctic and unchanged East Antarctic ice discharge over the last 7 years. *The Cryosphere*, 12(2):521–547, Feb 2018. doi: 10.5194/tc-12-521-2018.

Glen, J. W. The creep of polycrystalline ice. *Proceedings of the Royal Society of London. Series A, Mathematical and Physical Sciences*, 228(1175):519–538, 1955. doi: 10.1098/rspa.1955.0066.

Gottlieb, L. Development and Applications of a Runoff Model for Snowcovered and Glacierized Basins. *Hydrology Research*, 11(5):255–272, 10 1980. doi: 10.2166/nh.1980.0013.

Gropp, W. and Lusk, E. Users guide for mpich, a portable implementation of MPI. Jul 1996. doi: 10.2172/378910.

Gropp, W., Lusk, E., Doss, N., and Skjellum, A. A high-performance, portable implementation of the MPI message passing interface standard. *Parallel Computing*, 22(6):789–828, Sep 1996. doi: 10.1016/0167-8191(96)00024-5.

Gulley, J., Benn, D., Müller, D., and Luckman, A. A cut-and-closure origin for englacial conduits in uncrevassed regions of polythermal glaciers. *Journal of Glaciology*, 55(189):66–80, 2009a. doi: 10.3189/002214309788608930.

Gulley, J., Benn, D., Screaton, E., and Martin, J. Mechanisms of englacial conduit formation and their implications for subglacial recharge. *Quaternary Science Reviews*, 28(19):1984–1999, 2009b. doi: 10.1016/j.quascirev.2009.04.002.

Hager, A. O., Hoffman, M. J., Price, S. F., and Schroeder, D. M. Persistent, extensive channelized drainage modeled beneath Thwaites Glacier, West Antarctica. *The Cryosphere*, 16(9):3575–3599, 2022. doi: 10.5194/tc-16-3575-2022.

Harcourt, W. D., Palmer, S. J., Mansell, D. T., Le Brocq, A., Bartlett, O., Gourmelen, N., Tepes, P., Dowdeswell, J. A., Blankenship, D. D., and Young, D. A. Subglacial controls on dynamic thinning at Trinity-Wykeham Glacier, Prince of Wales Ice Field, Canadian Arctic. *International Journal of Remote Sensing*, 41(3):1191–1213, Aug 2019. doi: 10.1080/01431161.2019.1658238.

Harig, C. and Simons, F. J. Ice mass loss in Greenland, the Gulf of Alaska, and the Canadian Archipelago: Seasonal cycles and decadal trends. *Geophysical Research Letters*, 43 (7):3150–3159, 2016. doi: 10.1002/2016GL067759.

Hart, J. K., Young, D. S., Baurley, N. R., Robson, B. A., and Martinez, K. The seasonal evolution of subglacial drainage pathways beneath a soft-bedded glacier. *Communications Earth & Environment*, 3(1), Jun 2022. doi: 10.1038/s43247-022-00484-9.

Hecht, F. bamg: Bidimensional anisotropic mesh generator. Jan 1998.

Hewitt, I. J. Modelling distributed and channelized subglacial drainage: the spacing of channels. *Journal of Glaciology*, 57(202):302–314, 2011. doi: 10.3189/002214311796405951.

Hill, E. A., Gudmundsson, G. H., Carr, J. R., and Stokes, C. R. Velocity response of Petermann Glacier, Northwest Greenland, to past and future calving events. *The Cryosphere*, 12(12):3907–3921, 2018. doi: 10.5194/tc-12-3907-2018.

Hill, T., Flowers, G., Hoffman, M., Bingham, D., and Werder, M. Improved representation of laminar and turbulent sheet flow in subglacial drainage models. Jul 2023.

Hooke, R., Laumann, T., and Kohler, J. Subglacial water pressures and the shape of subglacial conduits. *Journal of Glaciology*, 36:67–71, Jan 1990. doi: 10.1017/S0022143000005566.

Howe, J. A., Husum, K., Inall, M. E., Coogan, J., Luckman, A., Arosio, R., Abernethy, C., and Verchili, D. Autonomous underwater vehicle (AUV) observations of recent tidewater glacier retreat, western Svalbard. *Marine Geology*, 417:106009, 2019. doi: 10.1016/j.margeo.2019.106009.

Hugonnet, R., McNabb, R., Berthier, E., Menounos, B., Nuth, C., Girod, L., Farinotti, D., Huss, M., Dussaillant, I., Brun, F., and Kääb, A. Accelerated global glacier mass loss in the early twenty-first century. *Nature*, 592(7856):726–731, Apr 2021. doi: 10.1038/s41586-021-03436-z.

Iken, A. The effect of the subglacial water pressure on the sliding velocity of a glacier in an idealized numerical model. *Journal of Glaciology*, 27(97):407–421, 1981. doi: 10.3189/S0022143000011448.

Iken, A. and Bindschadler, R. A. Combined measurements of subglacial water pressure and surface velocity of Findelengletscher, Switzerland: Conclusions about drainage system

and sliding mechanism. *Journal of Glaciology*, 32(110):101–119, 1986. doi: 10.3189/s0022143000006936.

Jackson, R. H., Shroyer, E. L., Nash, J. D., Sutherland, D. A., Carroll, D., Fried, M. J., Catania, G. A., Bartholomaus, T. C., and Stearns, L. A. Near-glacier surveying of a subglacial discharge plume: Implications for plume parameterizations. *Geophysical Research Letters*, 44(13):6886–6894, 2017. doi: 10.1002/2017GL073602.

Jansson, P., Kohler, J., and Pohjola, V. Characteristics of basal ice at Engabreen, northern Norway. *Annals of Glaciology*, 22, Jan 1996. doi: 10.1017/S0260305500015299.

Johnson, J. and Fastook, J. L. Northern Hemisphere glaciation and its sensitivity to basal melt water. *Quaternary International*, 95-96:65–74, 2002. doi: 10.1016/S1040-6182(02)00028-9.

Joughin, I., Das, S. B., King, M. A., Smith, B. E., Howat, I. M., and Moon, T. Seasonal speedup along the western flank of the Greenland Ice Sheet. *Science*, 320(5877):781–783, 2008. doi: 10.1126/science.1153288.

Kamb, B., Engelhardt, H., Fahnestock, M. A., Humphrey, N., Meier, M., and Stone, D. Mechanical and hydrologic basis for the rapid motion of a large tidewater glacier: 2. Interpretation. *Journal of Geophysical Research*, 99(B8):15231, 1994. doi: 10.1029/94jb00467.

Larour, E., Seroussi, H., Morlighem, M., and Rignot, E. Continental scale, high order, high spatial resolution, ice sheet modeling using the Ice Sheet System Model (ISSM). *Journal of Geophysical Research: Earth Surface*, 117(F1), Mar 2012. doi: 10.1029/2011jf002140.

Lingle, C. S. and Fatland, D. R. Does englacial water storage drive temperate glacier surges? *Annals of Glaciology*, 36:14–20, 2003. doi: 10.3189/172756403781816464.

McArthur, K., McCormack, F. S., and Dow, C. F. Basal conditions of Denman Glacier from glacier hydrology and ice dynamics modeling. 2023.

Meier, M., Lundstrom, S., Stone, D., Kamb, B., Engelhardt, H., Humphrey, N., Dunlap, W., Fahnestock, M., Krimmel, R., and Walters, R. Mechanical and hydrologic basis for the rapid motion of a large tidewater glacier. 1. Observations. *Journal of Geophysical Research*, 99:15,219–15,229, 09 1994. doi: 10.1029/94JB00237.

Millan, R., Mouginot, J., and Rignot, E. Mass budget of the glaciers and ice caps of the Queen Elizabeth Islands, Canada, from 1991 to 2015. *Environmental Research Letters*, 12(2):024016, Feb 2017. doi: 10.1088/1748-9326/aa5b04.

Miège, C., Forster, R. R., Brucker, L., Koenig, L. S., Solomon, D. K., Paden, J. D., Box, J. E., Burgess, E. W., Miller, J. Z., McNerney, L., Brautigam, N., Fausto, R. S., and Gogineni, S. Spatial extent and temporal variability of Greenland firn aquifers detected by ground and airborne radars. *Journal of Geophysical Research: Earth Surface*, 121 (12):2381–2398, 2016. doi: 10.1002/2016JF003869.

Moon, T., Joughin, I., Smith, B., van den Broeke, M. R., van de Berg, W. J., Noël, B., and Usher, M. Distinct patterns of seasonal Greenland glacier velocity. *Geophysical Research Letters*, 41(20):7209–7216, 2014. doi: 10.1002/2014GL061836.

Mortimer, C. A. and Sharp, M. Spatiotemporal variability of Canadian High Arctic glacier surface albedo from MODIS data, 2001–2016. *The Cryosphere*, 12(2):701–720, Feb 2018. doi: 10.5194/tc-12-701-2018.

Munneke, P. K., M. Ligtenberg, S. R., van den Broeke, M. R., van Angelen, J. H., and Forster, R. R. Explaining the presence of perennial liquid water bodies in the firn of the Greenland Ice Sheet. *Geophysical Research Letters*, 41(2):476–483, 2014. doi: 10.1002/2013GL058389.

Murray, T., Stuart, G. W., Fry, M., Gamble, N. H., and Crabtree, M. D. Englacial water distribution in a temperate glacier from surface and borehole radar velocity analysis. *Journal of Glaciology*, 46(154):389–398, 2000. doi: 10.3189/172756500781833188.

Müller, F. and Iken, A. Velocity fluctuations and water regime at Arctic valley glaciers. In *Symposium on the hydrology of glaciers, Cambridge, 7-13 September 1969*, pages 7–13. International Association of Scientific Hydrology, 1973.

Nienow, P., Sharp, M., and Willis, I. Seasonal changes in the morphology of the subglacial drainage system, Haut Glacier d'Arolla, Switzerland. *Earth Surface Processes and Landforms*, 23(9):825–843, 1998. doi: 10.1002/(SICI)1096-9837(199809)23:9⟨825::AID-ESP893⟩3.0.CO;2-2.

Noël, B., van de Berg, W. J., Lhermitte, S., Wouters, B., Schaffer, N., and van den Broeke, M. R. Six decades of glacial mass loss in the Canadian Arctic Archipelago. *Journal of Geophysical Research: Earth Surface*, 123(6):1430–1449, Jun 2018. doi: 10.1029/2017jf004304.

Nye, J. Water at the bed of a glacier. In *International Glaciological Society: Symposium on the hydrology of glaciers*, pages 189–194. International Association of Scientific Hydrology, 1973.

O'Callaghan, J. F. and Mark, D. M. The extraction of drainage networks from digital elevation data. *Computer Vision, Graphics, and Image Processing*, 28(3):323–344, 1984. doi: 10.1016/S0734-189X(84)80011-0.

Paden, J. L. C. L. F. R.-M., J. and Hale., R. IceBridge MCoRDS L3 Gridded Ice Thickness, Surface, and Bottom, Version 2, 2013.

Paterson, W. S. B. *The physics of glaciers*. Pergamon, Oxford, OX, England ;, 3rd edition, 1994. ISBN 0080379451. doi: 10.1016/C2009-0-14802-X.

Pitcher, L. H. and Smith, L. C. Supraglacial streams and rivers. *Annual Review of Earth and Planetary Sciences*, 47(1):421–452, 2019. doi: 10.1146/annurev-earth-053018-060212.

Poinar, K., Dow, C. F., and Andrews, L. C. Long-term support of an active subglacial hydrologic system in Southeast Greenland by firn aquifers. *Geophysical Research Letters*, 46(9):4772–4781, May 2019. doi: 10.1029/2019gl082786.

Porter, C., Morin, P., Howat, I., Noh, M.-J., Bates, B., Peterman, K., Keesey, S., Schlenk, M., Gardiner, J., Tomko, K., Willis, M., Kelleher, C., Cloutier, M., Husby, E., Foga, S., Nakamura, H., Platson, M., Wethington, J., Michael, Williamson, C., Bauer, G., Enos, J., Arnold, G., Kramer, W., Becker, P., Doshi, A., D'Souza, C., Cummens, P., Laurier, F., and Bojesen, M. ArcticDEM, Version 3, 2018.

Pälli, A., Moore, J. C., Jania, J., Kolondra, L., and Glowacki, P. The drainage pattern of Hansbreen and Werenskioldbreen, two polythermal glaciers in Svalbard. *Polar Research*, 22(2):355–371, Jan. 2003. doi: 10.3402/polar.v22i2.6465.

Rada Giacaman, C. A. and Schoof, C. Channelized, distributed, and disconnected: spatial structure and temporal evolution of the subglacial drainage under a valley glacier in the Yukon. *The Cryosphere*, 17(2):761–787, 2023. doi: 10.5194/tc-17-761-2023.

Raup, B., Racoviteanu, A., Khalsa, S. J. S., Helm, C., Armstrong, R., and Arnaud, Y. The GLIMS geospatial glacier database: A new tool for studying glacier change. *Global and Planetary Change*, 56(1–2):101–110, Mar 2007. doi: 10.1016/j.gloplacha.2006.07.018.

Rignot, E., Koppes, M., and Velicogna, I. Rapid submarine melting of the calving faces of West Greenland glaciers. *Nature Geoscience*, 3(3):187–191, Feb 2010. doi: 10.1038/ngeo765.

Robin, G. Q. Is the basal ice of a temperate glacier at the pressure melting point? *Journal of Glaciology*, 16(74):183–196, 1976. doi: 10.3189/S002214300003152X.

Ryser, C., Lüthi, M. P., Andrews, L. C., Catania, G. A., Funk, M., Hawley, R., Hoffman, M., and Neumann, T. A. Caterpillar-like ice motion in the ablation zone of the Greenland Ice Sheet. *Journal of Geophysical Research: Earth Surface*, 119(10):2258–2271, 2014. doi: 10.1002/2013JF003067.

Röthlisberger, H. Water pressure in intra- and subglacial channels. *Journal of Glaciology*, 11(62):177–203, 1972. doi: 10.3189/s0022143000022188.

Scholzen, C., Schuler, T. V., and Gilbert, A. Sensitivity of subglacial drainage to water supply distribution at the Kongsfjord basin, Svalbard. *The Cryosphere*, 15(6):2719–2738, Jun 2021. doi: 10.5194/tc-15-2719-2021.

Schoof, C. The effect of cavitation on glacier sliding. *Proceedings: Mathematical, Physical and Engineering Sciences*, 461(2055):609–627, 2005. doi: 10.1098/rspa.2004.1350.

Schoof, C. Ice sheet grounding line dynamics: Steady states, stability, and hysteresis. *Journal of Geophysical Research: Earth Surface*, 112(F3), 2007. doi: 10.1029/2006JF000664.

Schoof, C. Ice-sheet acceleration driven by melt supply variability. *Nature*, 468(7325): 803–806, Dec 2010. doi: 10.1038/nature09618.

Schwanghart, W. and Scherler, D. Short Communication: TopoToolbox 2 – MATLAB-based software for topographic analysis and modeling in Earth surface sciences. *Earth Surface Dynamics*, 2(1):1–7, 2014. doi: 10.5194/esurf-2-1-2014.

Schwanghart, W. and Kuhn, N. J. TopoToolbox: A set of Matlab functions for topographic analysis. *Environmental Modelling Software*, 25(6):770–781, 2010. doi: 10.1016/j.envsoft.2009.12.002.

Seale, A., Christoffersen, P., Mugford, R. I., and O'Leary, M. Ocean forcing of the Greenland Ice Sheet: Calving fronts and patterns of retreat identified by automatic satellite monitoring of eastern outlet glaciers. *Journal of Geophysical Research*, 116(F3), Aug 2011. doi: 10.1029/2010jf001847.

Sharp, M., Burgess, D. O., Cogley, J. G., Ecclestone, M., Labine, C., and Wolken, G. J. Extreme melt on Canada's Arctic ice caps in the 21st century. *Geophysical Research Letters*, 38(11), Jun 2011. doi: 10.1029/2011gl047381.

Shiklomanov, I. A. *World fresh water resources*, page 13–24. Oxford University Press, New York, USA, 1993.

Short, N. H. and Gray, A. L. Potential for RADARSAT-2 interferometry: glacier monitoring using speckle tracking. *Canadian Journal of Remote Sensing*, 30(3):504–509, Jan 2004. doi: 10.5589/m03-071.

Short, N. H. and Gray, A. L. Glacier dynamics in the Canadian High Arctic from RADARSAT-1 speckle tracking. *Canadian Journal of Remote Sensing*, 31(3):225–239, Jan 2005. doi: 10.5589/m05-010.

Shreve, R. L. Movement of water in glaciers. *Journal of Glaciology*, 11(62):205–214, 1972. doi: 10.3189/s002214300002219x.

Slater, D. A., Straneo, F., Das, S. B., Richards, C. G., Wagner, T. J. W., and Nienow, P. W. Localized plumes drive front-wide ocean melting of a Greenlandic tidewater glacier. *Geophysical Research Letters*, 45(22):12,350–12,358, 2018. doi: 10.1029/2018GL080763.

Smith, L. C., Andrews, L. C., Pitcher, L. H., Overstreet, B. T., Rennermalm, K., Cooper, M. G., Cooley, S. W., Ryan, J. C., Miège, C., Kershner, C., and Simpson, C. E. Supraglacial river forcing of subglacial water storage and diurnal ice sheet motion. *Geophysical Research Letters*, 48(7):e2020GL091418, 2021. doi: 10.1029/2020GL091418.

Smith, L. C., Yang, K., Pitcher, L. H., Overstreet, B. T., Chu, V. W., Åsa K. Rennermalm, Ryan, J. C., Cooper, M. G., Gleason, C. J., Tedesco, M., Jeyaratnam, J., van As, D., van den Broeke, M. R., van de Berg, W. J., Noël, B., Langen, P. L., Cullather, R. I., Zhao, B., Willis, M. J., Hubbard, A., Box, J. E., Jenner, B. A., and Behar, A. E. Direct measurements of meltwater runoff on the Greenland Ice Sheet surface. *Proceedings of the National Academy of Sciences of the United States of America*, 114(50):E10622–E10631, 2017. doi: 10.1073/pnas.1707743114.

Sole, A., Nienow, P., Bartholomew, I., Mair, D., Cowton, T., Tedstone, A., and King, M. A. Winter motion mediates dynamic response of the Greenland Ice Sheet to warmer summers. *Geophysical Research Letters*, 40(15):3940–3944, 2013. doi: 10.1002/grl.50764.

Sommers, A. N. and Rajaram, H. Energy transfer by turbulent dissipation in glacial conduits. *Journal of Geophysical Research: Earth Surface*, 125(10):e2019JF005502, 2020. doi: 10.1029/2019JF005502.

Stevens, L. A., Nettles, M., Davis, J. L., Creyts, T. T., Kingslake, J., Ahlstrøm, A. P., and Larsen, T. B. Helheim Glacier diurnal velocity fluctuations driven by surface melt forcing. *Journal of Glaciology*, 68(267):77–89, 2022. doi: 10.1017/jog.2021.74.

Straneo, F. and Heimbach, P. North Atlantic warming and the retreat of Greenland's outlet glaciers. *Nature*, 504(7478):36–43, Dec 2013. doi: 10.1038/nature12854.

Sundal, A. V., Shepherd, A., Nienow, P., Hanna, E., Palmer, S., and Huybrechts, P. Melt-induced speed-up of Greenland Ice Sheet offset by efficient subglacial drainage. *Nature*, 469(7331):521–524, January 2011. doi: 10.1038/nature09740.

Tarboton, D. and Ames, D. Advances in the mapping of flow networks from digital elevation data. 111, 03 2001. doi: 10.1061/40569(2001)166.

Tarboton, D. G. A new method for the determination of flow directions and upslope areas in grid digital elevation models. *Water Resources Research*, 33(2):309–319, 1997. doi: 10.1029/96WR03137.

Truffer, M. and Motyka, R. J. Where glaciers meet water: Subaqueous melt and its relevance to glaciers in various settings. *Reviews of Geophysics*, 54(1):220–239, Mar 2016. doi: 10.1002/2015rg000494.

Trunz, C., Covington, M. D., Poinar, K., Andrews, L. C., Mejia, J., and Gulley, J. Modeling the influence of moulin shape on subglacial hydrology. *Journal of Geophysical Research: Earth Surface*, 127(8), Aug 2022. doi: 10.1029/2022jf006674.

Vallot, D., Pettersson, R., Luckman, A., Benn, D. I., Zwinger, T., Van Pelt, W. J. J., Kohler, J., Schäfer, M., Claremar, B., Hulton, N. R. J., and et al. Basal dynamics of Kronebreen, a fast-flowing tidewater glacier in Svalbard: non-local spatio-temporal response to water input. *Journal of Glaciology*, 63(242):1012–1024, 2017. doi: 10.1017/jog.2017.69.

van de Wal, R. S. W., Boot, W., van den Broeke, M. R., Smeet, C. J. P. P., Reijmer, C. H., Donker, J. J. A., and Oerlemans, J. Large and rapid melt-induced velocity changes in the ablation zone of the Greenland Ice Sheet. *Science*, 321(5885):111–113, 2008. doi: 10.1126/science.1158540.

van de Wal, R. S. W., Smeets, C. J. P. P., Boot, W., Stoffelen, M., van Kampen, R., Doyle, S. H., Wilhelms, F., van den Broeke, M. R., Reijmer, C. H., Oerlemans, J., and Hubbard, A. Self-regulation of ice flow varies across the ablation area in South-West Greenland. *The Cryosphere*, 9(2):603–611, 2015. doi: 10.5194/tc-9-603-2015.

van der Veen, C. J. Fracture propagation as means of rapidly transferring surface meltwater to the base of glaciers. *Geophysical Research Letters*, 34(1), 2007. doi: 10.1029/2006GL028385.

Van Wychen, W., Burgess, D. O., Gray, L., Copland, L., Sharp, M., Dowdeswell, J. A., and Benham, T. J. Glacier velocities and dynamic ice discharge from the Queen Elizabeth Islands, Nunavut, Canada. *Geophysical Research Letters*, 41(2):484–490, Jan 2014. doi: 10.1002/2013gl058558.

Van Wychen, W., Davis, J., Burgess, D. O., Copland, L., Gray, L., Sharp, M., and Mortimer, C. Characterizing interannual variability of glacier dynamics and dynamic discharge (1999-2015) for the ice masses of Ellesmere and Axel Heiberg Islands, Nunavut, Canada. *Journal of Geophysical Research: Earth Surface*, 121(1):39–63, Jan 2016. doi: 10.1002/2015jf003708.

Van Wychen, W., Burgess, D., Kochtitzky, W., Nikolic, N., Copland, L., and Gray, L. RADARSAT-2 derived glacier velocities and dynamic discharge estimates for the Canadian High Arctic: 2015–2020. *Canadian Journal of Remote Sensing*, 46(6):695–714, Nov 2020a. doi: 10.1080/07038992.2020.1859359.

Van Wychen, W., Copland, L., and Burgess, D. Ice masses of the eastern Canadian Arctic Archipelago. In Slaymaker, O. and Catto, N., editors, *Landscapes and Landforms of Eastern Canada*, page 297–314. Springer International Publishing, Cham, Switzerland, 2020b. doi: 10.1007/978-3-030-35137-3_13.

Vaughan, D. G. Relating the occurrence of crevasses to surface strain rates. *Journal of Glaciology*, 39(132):255–266, 1993. doi: 10.3189/S0022143000015926.

Walder, J. and Hallet, B. Geometry of former subglacial water channels and cavities. *Journal of Glaciology*, 23(89):335–346, 1979. doi: 10.3189/S0022143000029944.

Walder, J. S. Hydraulics of subglacial cavities. *Journal of Glaciology*, 32(112):439–445, 1986. doi: 10.3189/S0022143000012156.

Weertman, J. Stability of the junction of an ice sheet and an ice shelf. *Journal of Glaciology*, 13(67):3–11, 1974. doi: 10.3189/S0022143000023327.

Weertman, J. and Birchfield, G. E. Basal water film, basal water pressure, and velocity of traveling waves on glaciers. *Journal of Glaciology*, 29(101):20–27, 1983. doi: 10.3189/S0022143000005116.

Weertman, J. Can a water-filled crevasse reach the bottom surface of a glacier? In *Symposium on the Hydrology of Glaciers, Cambridge, 7-13 September 1969*, page 139–145. International Association of Scientific Hydrology, 1973.

Weertman, J. Creep deformation of ice. *Annual Review of Earth and Planetary Sciences*, 11(1):215–240, 1983. doi: 10.1146/annurev.ea.11.050183.001243.

Werder, M. A., Hewitt, I. J., Schoof, C. G., and Flowers, G. E. Modeling channelized and distributed subglacial drainage in two dimensions. *Journal of Geophysical Research: Earth Surface*, 118(4):2140–2158, Oct 2013. doi: 10.1002/jgrf.20146.

Willis, I. C., Pope, E. L., Leysinger Vieli, G. J.-M., Arnold, N. S., and Long, S. Drainage networks, lakes and water fluxes beneath the Antarctic ice sheet. *Annals of Glaciology*, 57(72):96–108, 2016. doi: 10.1017/aog.2016.15.

Wright, P. J., Harper, J. T., Humphrey, N. F., and Meierbachtol, T. W. Measured basal water pressure variability of the western Greenland Ice Sheet: Implications for hydraulic potential. *Journal of Geophysical Research: Earth Surface*, 121(6):1134–1147, Jun 2016. doi: 10.1002/2016jf003819.

Wójcik, K. A. and Sobota, I. Spatial and temporal changes in ablation, distribution and evolution of glacial zones on Irenebreen, a small glacier of the High Arctic, Svalbard. *Polar Science*, 23:100503, 2020. doi: 10.1016/j.polar.2020.100503.

Yang, K. and Smith, L. C. Internally drained catchments dominate supraglacial hydrology of the Southwest Greenland Ice Sheet. *Journal of Geophysical Research: Earth Surface*, 121(10):1891–1910, 2016. doi: 10.1002/2016JF003927.

Zemp, M., Huss, M., Thibert, E., Eckert, N., McNabb, R., Huber, J., Barandun, M., Machguth, H., Nussbaumer, S. U., Gärtner-Roer, I., Thomson, L., Paul, F., Maussion, F., Kutuzov, S., and Cogley, J. G. Global glacier mass changes and their contributions to sea-level rise from 1961 to 2016. *Nature*, 568(7752):382–386, Apr 2019. doi: 10.1038/s41586-019-1071-0.

Zweng, M. M. and Münchow, A. Warming and freshening of Baffin Bay, 1916–2003. *Journal of Geophysical Research*, 111(C7), 2006. doi: 10.1029/2005jc003093.